HOKKAIDO
UNIVERSITY

DOCTORAL THESIS

Synthesis and function exploration of new composite materials from designable precursors containing carbon using ultrahigh pressure

（炭素を含む設計可能な前駆体への超高圧処理を用いた複合材料の合成と機能探索）

Ichiro YAMANE

Materials Chemistry and Engineering Course

Graduate School of Chemical Sciences and Engineering

Hokkaido University

(Doctoral Supervisor : Toshihiro SHIMADA, Professor)

（ 指導教員：島田 敏宏　教授 ）

Contents

Chapter 1 General Introduction

1.1 Carbon materials

1.1.1 Carbon and its allotropes

Carbon is an element with atomic number 6, and its electron configuration as one atom is $1s^2 2s^2 2p^2$. Four electrons in the 2s and 2p orbitals act as valence electrons, and these valence electrons can form sp, sp^2, and sp^3 hybridization states. This feature enables carbon atoms to make a variety of structures with covalent bonds. Therefore, there are numerous kinds of molecules that contain skeletons of carbon atoms, i.e., organic compounds. More than millions of those compounds have been discovered so far.

This structural diversity is not limited to organic molecules. As the phase diagram [1,2] shows (Figure 1-1), the thermodynamically stable solid phases of carbon allotropes are only graphite and diamond, but many metastable allotropes exist because of the diverse topology of carbon described above. Examples including carbyne [3], Lonsdaleite [4], glassy carbon [5], and amorphous carbon. These are bulk allotropes with huge long-range order due to covalent bonding, but metastable allotropes with

nano-sized structures have also been discovered. These allotropes are called nanocarbons. Examples of nanocarbons are fullerenes [6,7], carbon nanotubes [8], graphene [9], and their structural derivatives, such as carbon nanohorns [10], graphene nanoribbons [11], and carbon nanobelts [12]. In addition, many hypothetic carbon allotropes have been predicted by first-principles calculations [13], such as M-carbon and Z-carbon.

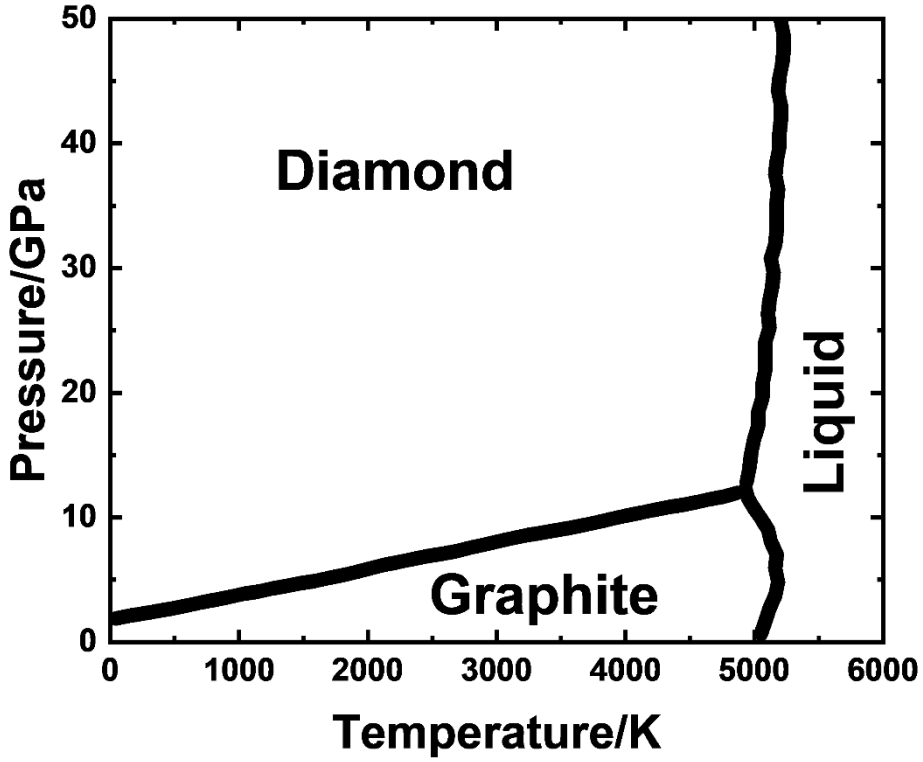

Figure 1-1 *P-T* phase diagram for carbon, based on Ref. [1] and [2].

Each of these allotropes has different carbon hybridization states and bonding patterns, leading to different properties. Furthermore, even the same allotrope can

exhibit different properties by changing its morphology, such as nanoparticles, thin films, and fibers. This flexibility in the material design is the important and unique feature of carbon. Further discovery of novel materials and further understanding of the relationship between structure and function are expected in the future.

1.1.2 Preparation of Carbon materials

This section describes the preparation methods of various carbon containing materials. Organic compounds are mainly used as precursors, which are carbonized by pyrolysis or other processes to produce carbon materials. Some carbon material can also be used as a precursor for other carbon materials, as in synthesizing artificial graphite from coke, or synthesizing diamond from graphite. The preparation methods of carbon materials can be classified into three types by the phases of the precursors during carbonization: vapor phase synthesis, liquid phase synthesis, and solid phase synthesis.

In vapor-phase synthesis, carbon materials are produced by introducing source gas into a chamber or tube furnace and converting them. An example of this method is chemical vapor deposition (CVD). The source gas introduced into the reaction vessel is activated by microwave [14] or thermal treatment [15]. The activated precursors react on the surface of the substrate to form carbon materials. Graphene and diamond thin films are synthesized by CVD [14,15]. In addition, CVD with certain metal particles supported on the substrate enables carbon materials to grow one-dimensionally from the

particles.

It provides carbon nanotubes [16,17]. The metal particles act as a catalyst this time. Examples of the vapor phase method, except for CVD, include the synthesis of fullerenes by laser ablation [6] and arc discharge [18].

Liquid-phase synthesis is conducted by decomposing and carbonizing precursors via a liquid phase. An example of liquid-phase synthesis is the synthesis of raw cokes. Liquid organic compounds such as pitch and coal tar are used as starting materials [19]. Carbonization proceeds in the liquid phase when they pyrolyze, and coke are finally generated. Another example that has been attracting attention in recent years includes the solution synthesis of nanocarbons. This method is to obtain graphene-related nanocarbons by coupling aromatic compounds in solution using techniques of synthetic organic chemistry. carbon nanorings [20], carbon nanobelts [21], and Möbius carbon nanobelts [21] have been reported so far.

Examples of solid-phase synthesis include synthesizing activated carbon (a kind of amorphous carbon) and glassy carbon by thermal treatment of organic compounds such as coal tar and thermosetting resins. Another important example of solid-state synthesis is the high-pressure and high-temperature synthesis of diamonds from graphite. This method converts raw materials into diamonds under conditions where the diamond is thermodynamically stable. There are two techniques for the method: one is to use a

metal catalyst, and the other is to convert the raw material directly without metal. In the former method, diamond is synthesized from graphite at >5-6 GPa and 1300-1600 °C in the presence of iron, nickel, cobalt, etc [22–24]. Metals works as catalysts and solvents in this technique, and diamond crystals are grown in molten metals. This method allows synthesis under milder conditions than the direct conversion technique described below, whereas it has the disadvantage that the diamond sometimes includes metal atoms [22]. On the other hand, in the metal-free technique, graphite can be directly converted to diamond by the treatment under more severe conditions of >10 GPa, >2000 °C [25,26].

1.1.3 Doping to carbon materials

The doping of heteroatoms is also a factor in determining the properties of carbon materials, whereas it was mentioned at the beginning of this chapter that carbon materials exhibit a wide variety of physical properties by controlling the electronic states and the bondings. For example, boron-doped diamonds can act as p-type semiconductors and exhibit significantly enhanced electrical conductivity [27]. Nitrogen-vacancy centers obtained by replacing carbon atoms in diamonds with an N atom in diamonds can capture electrons. They are promising materials as high-performance sensing devices [28]. The elements, such as Si and Ge also form vacancy center like N when doped to diamond [29]. Another useful example is N doping of graphite structure. Such N-doped carbon exhibits various catalytic activities, such as

electrochemical oxygen reduction reactions [30–32].

Doping methods include ion-beam bombardment [30], post-treatment of synthesized carbon materials [30,33], and synthesis of carbon materials from precursors that contain heteroatoms [29].

1.1.4. Composite of carbon materials and metal or metal compounds

Carbon materials are often used as composites with other materials. One of those applications is a support for catalysts [34–36]. Support in catalysts is a material in which catalyst particles are dispersed and fixed on its surface. Such catalyst-supported solid materials are called heterogeneous catalysts and are used as catalysts in liquid- and gas-phase reactions. They are essential in industrial applications due to ease of recovery.

The following properties are required for catalyst supports [34]: (1) Large surface area to support a large amount of catalyst and increase the active sites of reactions. (2) Chemical stability. The support must resist acids and bases condition and high temperatures and must not cause reactions other than the intended one. Some support materials themselves exhibit activity, or they enhance the activity of the catalyst by synergetic interaction with the catalyst. (3) Adsorption ability on the catalyst. If it is weak, particles will drop out and coagulate during use, leading to decrease performance. (4) electrical conductivity (in the case of electrocatalysts). Carbon materials satisfy

these conditions and are suitable as supports. In particular, in terms of their conductivity and cost, it is superior to other support materials, such as porous alumina and silica.

A method to prepare carbon-supported catalysts is to disperse the particles on prepared carbon materials afterward. A typical sequence is as follows: the carbon support is treated with a solution of the compounds of the metal, and the salt is adsorbed on the surface; subsequently, the salt adsorbed on the surface is converted into catalyst particles by heat treatment [37].

Another method is directly synthesizing composite materials by pyrolyzing an organic material containing metal atoms. This method uses organometallic compounds or metal-organic frameworks as precursors [38,39]. This method has the advantage that the synthesis proceeds in one step, but the disadvantage is that the particles grow and agglomerate during heat treatment. Sintering particles decreases the specific surface area of the particles, leading to decrease in reaction efficiency. Techniques to solve this problem have been reported, but this requires additional processes and highly designed precursors [40].

1.2 High-pressure treatment to search for new materials

1.2.1 High pressure on materials science

Pressure is a thermodynamically crucial physical quantity as well as temperature to

manipulate the states of matter [41]. Applying high pressure decreases the interatomic distances, leading to the following effects: the change of bonding patterns and the valence of atoms, the phase transition, and the electronic structure modification, such as electron transfer and reducing the band gap [41–44]. Those effects enable synthesizing the materials with novel composition, structure, and properties that could not be obtained under ambient conditions [41–44]. To manipulate not only pressure but also temperature can broaden a wider variety of substances to synthesize. Thus high-pressure (HP) or high-pressure and high-temperature (HPHT) treatments have been a powerful tool in the search for new materials [41,42].

High-pressure generation requires relatively large or special equipment. I briefly describe the kinds of methods to generate high-pressure and their features below. The methods can be generally classified into static compression and dynamic compression. The former generates pressure by hydraulic press via anvils or pistons. It is possible to control applied pressure, pressure holding time, and heating temperature independently because the pressure is slowly applied. The latter generates pressure by shock waves derived from a laser [45,46] or a gas gun [47,48]. This process is adiabatic compression, and the temperature of the sample also rises along with the pressure. This technique can generate higher pressure than the static compression, whereas pressure cannot be held for long.

The equipment for static compression will be described in more detail below because this study employs the static method. Apparatuses for the static compression are roughly categorized into piston-cylinder type, Bridgeman anvil press type, and multianvil press type (Figure 1-2).

The piston-cylinder is the simplest apparatus [49,50]. It generates high uniaxial pressure when the piston presses the sample cell assembly inside the cylinder. Achievable pressure is lower than other apparatuses, whereas a relatively large sample volume is available.

Bridgman anvil apparatus, or opposed-type anvil apparatus, was developed by the P.W. Bridgman [51]. He used opposed two anvils instead of the piston and succeeded in the improvement of the generated pressure. Although anvils are generally made of superhard materials such as cemented carbide, the device in which diamonds are used as anvils is specially called a diamond anvil cell (DAC) [52] because of its unique features. One of the features of DAC is achievable pressure. DAC can generate the highest pressure among static compression apparatuses because anvils are made of single-crystal diamonds, the hardest substance. The flat tip surface of anvils, called culet, has a the diameter with μm order, resulting in the microvolume sample space. Another feature is that *in situ* measurements are available. Taking advantage of the optical transparency of single-crystal diamonds, the observation by optical microscope and the

measurements such as X-ray diffraction (XRD), Raman spectroscopy, and Fourier transform infrared (FT-IR) spectroscopy can perform during experiments.

Multianvil press apparatus uses regular polyhedron-shaped sample cell assembly, such as tetrahedral [53,54], cubic [55,56], and octahedral [57]. Pressing each face of the cell with anvils generates high pressure. This way of applying pressure brings about good hydrostatic pressure. The apparatuses are suitable for the characterization and measurements of samples after experiments because they have relatively large sample spaces.

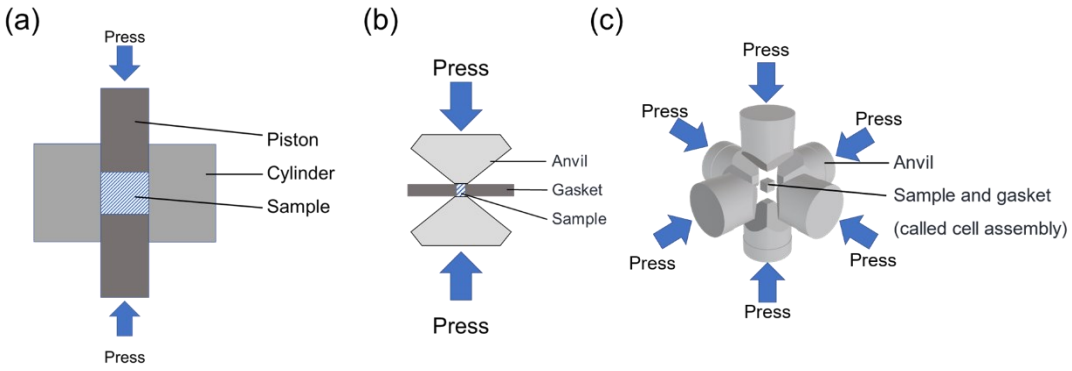

Figure 1-2 The schematic images of (a) piston cylinder, (b) Bridgman anvil apparatus, and (c) cubic anvil press apparatus (a type of multianvil press apparatuses).

1.2.2 Pressure-induced reaction of the organic compounds

HP processing of organic molecules has been the subject of investigation similar to that of HP synthesis in inorganic materials. The research on HP processing of organic

molecules can be classified into two types in terms of the pressure region. One is the investigation carried out in relatively lower pressure, 0.1-2 GPa. The other is that performed in >2 GPa pressure region, which is called ultrahigh pressure. Each type deals with solution reactions and solid-state reactions, respectively.

The studies conducted in 0.1-2 GPa mainly deal with solution reaction because the solvents do not solidify under these pressure regions. These studies are conducted in terms of synthetic organic chemistry, and their objective is to analyze the kinetics and reaction mechanisms at high pressure and to develop new reactions and molecules. The pressure effect on chemical reactions can be described by activation volume $\Delta V^{\ddagger}$ [58,59]. $\Delta V^{\ddagger}$ is defined as the difference between partial molar volumes of transition stats and reactants. $\Delta V^{\ddagger}$ is related to reaction rate constant k and pressure P by the following equation [58,59].

$$\Delta V^{\ddagger} = -RT\left(\frac{\partial \ln k}{\partial P}\right)_T \qquad (1)$$

It means reactions can be promoted under high pressure in $\Delta V^{\ddagger}<0$. Previous studies have revealed the types of reactions accelerated at high pressure [58]: (1) reactions in which the number of molecules decrease before and after the reaction [60,61]; (2) reactions via ionic intermediates [62,63]; (3) reactions via cyclic transition state [64]; (4) reactions inhibited kinetically by steric barriers [65]. Typical examples of each type are shown in Table 1-1.

Table 1-1 The examples of chemical reaction under high pressure

Reaction types	Reaction examples	Ref.
(1)	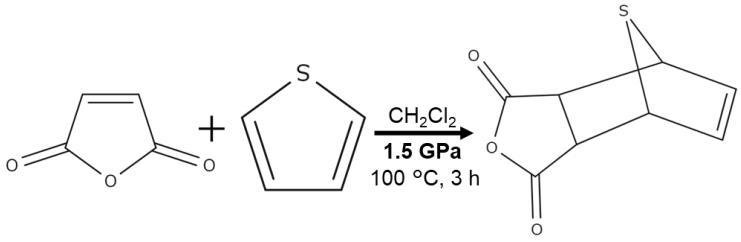 Diels-Alder reaction	[60]
(2)	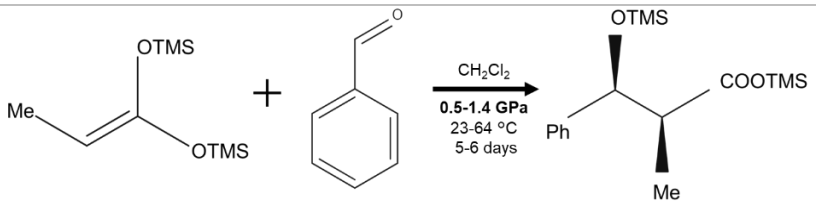 Mukaiyama aldol reaction	[62]
(3)	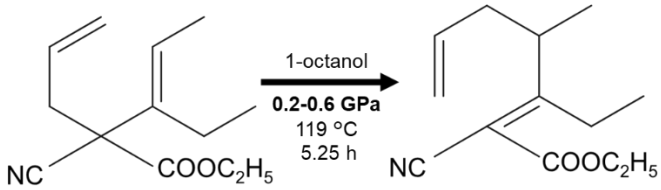 Cope rearrangement	[64]
(4)	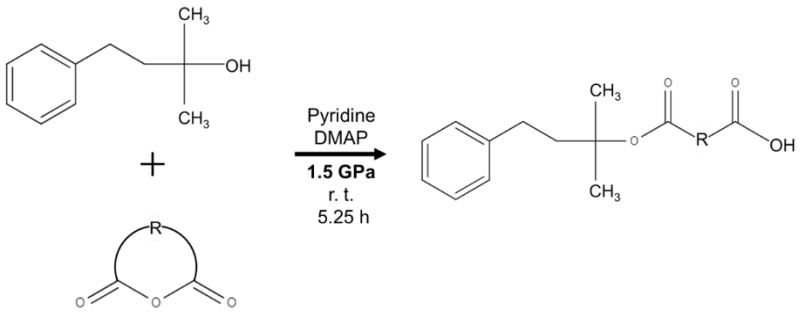 Esterification of tertiary alcohols	[65]

At more than 2 GPa, solid-state reactions have been an object of research because solvents solidified. Pressure-induced polymerization (PIP) is one of the main research topics of solid-state reactions of organic molecules. [66,67]. This polymerization occurs with unsaturated molecules because the bonding patterns transform triple bonds into

double ones or double ones into single ones by applying ultrahigh pressure [68,69]. This sequence satisfies the abovementioned criterion: (1) reactions in which the number of molecules decreased before and after the reaction. The difference between the PIP and typical polymerizations in solution is that PIP does not need solvents and catalysts. In addition, another feature of PIP is that the reaction can become a topotactic or topochemical process, i.e., the reaction can be affected significantly by the crystal structure of the reactants [70,71].

Examples of unsaturated molecules causing PIP include acetylene [71,72], ethylene [73], styrene [74], acetonitrile [75], and butadiene [76]. PIP also can transform π bonds and polymerize aromatic compounds, and the PIP of benzene [77,78], pyridine [79,80], triptycene [81], and so on have been reported.

It has also been reported that the products can form crystalline carbon materials, i.e., carbon framework with long-range when topotactic/topochemical PIP proceeds (Figure 1-3 and Table 1-2). For example, topochemical PIP of acetylene can produces graphane [71]. Acetylene initially transformed to polyacetylene, and then further PIP of the polyacetylene chain progressed, leading to crystalline graphane. Other examples include the carbon nanothreads from the π-stacked C_6H_6-C_6F_6 cocrystal [82,83] and the graphitic nanoribbon from 1,4-diphenylbutadiyne [70]. Besides hydrocarbons, fullerenes and their cocrystals with other compounds form ordered carbon frameworks

by PIP. Hence, the PIP was helpful for synthesizing carbon materials from molecules without pyrolysis though some obtained carbon solids synthesized could not be recovered at ambient pressure.

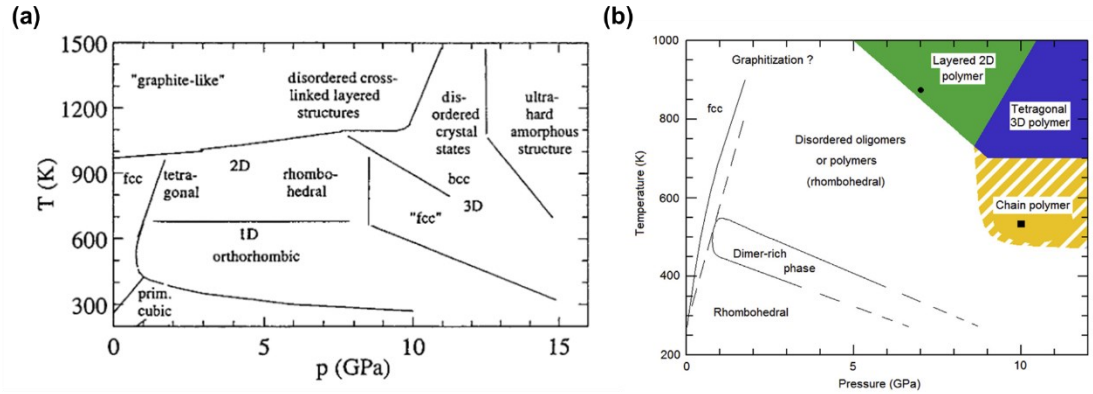

Figure 1-3 The phase diagrams of (a) C_{60} and (b) C_{70}. Adapted with permission from Ref [84] and [85], respectively. Copyright 2001 and 2017, Wiley-VCH and Elsevier, respectively.

Table 1-2 The carbon materials synthesized from molecules by PIP.

Precursors	Pressure /GPa	Temperature /°C	Products	Ref.
C_6H_6-C_6F_6 cocrystal	>20	r. t.	Carbon nanothread	[82]
C_6H_6-C_6F_6 cocrystal	>20	r. t.	Substituted graphane	[83]
1,4-diphenylbutadiyne	>10	r. t.	Graphitic nanoribbon	[70]
C_{60}	see Figure 1-3		1-3 D polymer	[84]
C_{70}	see Figure 1-3		1-3 D polymer	[85]
C_{60}-ferrocene cocrystal	1.5	300	1D polymer	[86]
C_{60}-ferrocene cocrystal	2	427	2D polymer	[86]
C_{60}-Ni(OEP) cocrystal	2	427	1D polymer	[86]
C_{60}-$AgNO_3$ cocrystal	1.5, 2	300, 427	1D polymer	[86]
C_{70}-ferrocene cocrystal	8	r. t.	1D polymer	[87]

One of the greatest challenges in searching for materials by PIP is that aromatic compounds often require much higher pressure for PIP. As a result, some polycyclic aromatic hydrocarbons (PAHs) do not polymerize, and only oligomers may be obtained (Table 1-3). Recent studies suggested that heteroatoms in an aromatic ring (e.g., N) or a number of aromatic rings influence the degree of oligomerization, whereas more results are required to investigate the effect.

Table 1-3 Previous studies on HPHT-induced oligomerization of aromatic compounds. * The oligomer with the largest degree of oligomerization. ** Dec. means decomposition to amorphous carbon.

Molecules	Number of rings	Pressure /GPa	Temperature /°C	Oligomers*	Ref.
Diphenyldiacetylene	2	0.13	250	9	[88]
Benzene	1	>13	r. t.	2	[89]
Naphthalene	2	7	500	4	[90]
		7	600	5	[90]
		20	r. t.	3	[91]
Anthracene	3	3.5	500	4	[92]
		3.5	600	2	[92]
		7	500	4	[90]
		7	600	Dec.**	[90]
Phenanthrene	3	7	500	5	[90]
Pyrene	4	3.5	500	5	[92]
		3.5	600	5	[92]
		7	500	7	[90]
		7	600	5	[90]
		7	700	Dec.**	[90]
Fluoranthene	4	7	500	5	[90]
		7	600	Dec.**	[90]
Benzo[a]pyrene	6	7	500	n. a.	[90]
		7	600	Dec.**	[90]
Coronene	7	3.5	500	4	[92]
		3.5	600	2	[92]
		7	500	6	[90]
		7	600	Dec.**	[90]
2,3-naphthyridine	2	0.5-1.5	200-300	7	[93]
1,5-naphthyridine	2	0.5-1.5	250-275	3	[94]

1.2.3 High-pressure and high-temperature treatments of the organic compounds

So far this section has focused on the pressure-induced chemical reactions of organic compounds undertaken at mild temperature conditions. The following section will describe studies on the HPHT treatments by which the compounds are pyrolyzed and carbonized. Those studies can be classified into ones on fundamental science and ones on materials science.

An example of the former is the HPHT treatment of aromatic compounds. Aromatic compounds are observed in mantle-derived minerals, meteorites, and space. It is consequently important for basic chemistry and geochemistry to investigate their behavior under deep earth, i.e., HPHT conditions. The PAHs behaviors under high pressure have been studied since 1940s [95], providing the pressure-temperature phase diagrams of many PAHs (Figure 1-4). However, the impact of molecular structures on the behavior on molecular structures is not fully understood, particularly impacts of heteroatoms [90,94,96–98].

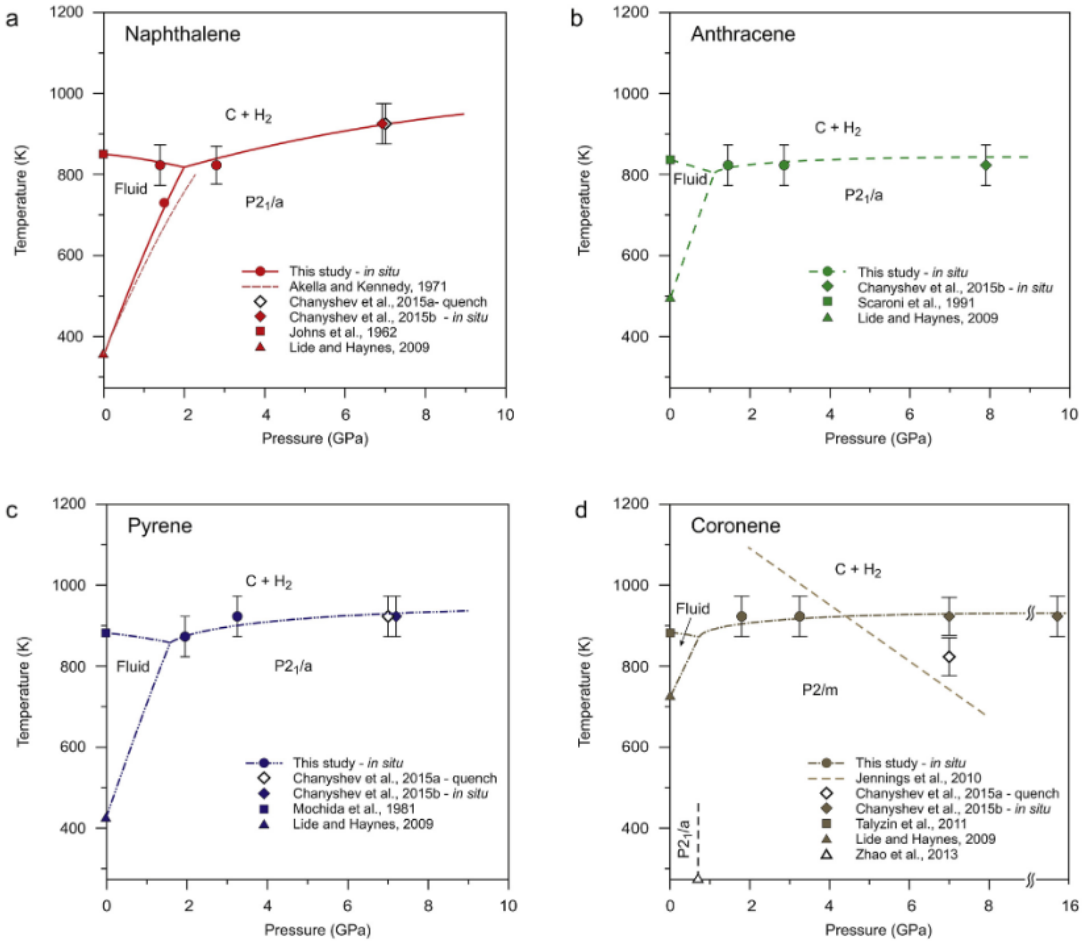

Figure 1-4 phase diagrams of PAHs: (a) naphthalene, (b) anthracene, (c) pyrene, and (d) coronene. Adapted with permission [98]. Copyright 2017, Elsevier.

The most popular example of the studies on materials science is the synthesis of diamonds. Diamonds have been one of the main research topics of what the synthesis technique, controlling morphology, characterization, and exploring similar materials with diamonds have been investigated. Under static HPHT synthesis, Diamonds are often synthesized with metal catalysts from graphite, whereas the synthesis from the organic compounds were reported by Wentorf in the 1960s [99]. The diamonds obtained

in Ref. [99] were not of high quality due to impurity and other problems, but recent studies provided the diamond with high crystallinity. The advantage of the synthetic route from organic compounds are as follows: 1) diamonds can be obtained under mild pressure and temperature conditions compared with the route from graphite; 2) controlling grain size is relatively easy.; 3) doped diamonds can be obtained by mixing molecules containing heteroatoms into the precursor hydrocarbons [29]. PAHs, adamantane, and their derivatives (a group of compounds with a diamond skeleton, such as adamantane, is called diamondoid.) were usually used as precursors [29,96,99–101]. In addition, a recent study reported that the nano-polycrystalline diamond was synthesized without binders from stearic acid [102].

Other types of material synthesis by HPHT treatments of organic compounds include carbon nitrides or C-N compounds. C-N compounds show a variety of compositions and crystal structures besides the graphitic C_3N_4 [103–105]. In particular, β-C_3N_4 has paid attention as superhard materials exceeding diamond [106,107]. So far, the HPHT treatments of triazole, triazine, and melamine have been reported to investigate novel C-N compounds [108–112].

1.3 Motivation of this study and organization of the thesis

One of motivation of this study was to investigate the effect of molecular structure on the pressure-induced oligomerization of aromatics. Although previous studies suggested that heteroatoms or a number of aromatic rings affect the degree of oligomerization, more findings are required to investigate the effect in detail. This study seeks to obtain data which will help to address these research gaps.

The other of motivation of this study was to investigate the usefulness of the HPHT treatments as a synthesis method for MOF-derived materials. In conventional preparation method, particles on MOF-derived materials tend to agglomerate during preparation. This can become disadvantage when the materials are used as catalysts. This study seeks focused on the possibility of suppressing diffusion under high pressure to solve the problem, consequently I will explore miniaturization of particles by HPHT treatments.

The overall structure if the thesis takes the form of five chapters. Chapter 1 was concerned with the general introduction of this study. Chapter 2 will consider the high pressure treatments of nitrogen-containing polycyclic aromatic hydrocarbons were carried out at room temperature in order to investigate the effect of molecular structure on the pressure-induced oligomerization of aromatics. In chapter 3, I have proposed pyrolysis of MOF under ultrahigh pressure and applied it to Cu-BTC, a kind of Cu-

containing MOF. The products were evaluated as the heterogeneous catalysts for organic reaction. Chapter 4 investigate the impact of applying pressure on the characteristics of the product in HPHT treatments of Cu-BTC. The obtained products were tested as catalysts in electrochemical reactions for function exploration. Chapter 5 is concerned with general conclusion.

References

[1] F. P. Bundy, *Pressure-Temperature Phase Diagram of Elemental Carbon*, Phys. A: Stat. Mech. Appl. **156**, 169 (1989).

[2] F. P. Bundy, W. A. Bassett, M. S. Weathers, R. J. Hemley, H. U. Mao, and A. F. Goncharov, *The Pressure-Temperature Phase and Transformation Diagram for Carbon; Updated through 1994*, Carbon **34**, 141 (1996).

[3] R. B. Heimann, J. Kleiman, and N. M. Salansky, *Structural Aspects and Conformation of Linear Carbon Polytypes (Carbynes)*, Carbon **22**, 147 (1984).

[4] C. Frondel and U. B. Marvin, *Lonsdaleite, a Hexagonal Polymorph of Diamond*, Nature **214**, 5088 (1967).

[5] S. Yamada and H. Sato, *Some Physical Properties of Glassy Carbon*, Nature **193**, 4812 (1962).

[6] H. W. Kroto, J. R. Heath, S. C. O'Brien, R. F. Curl, and R. E. Smalley, *C_{60}: Buckminsterfullerene*, Nature **318**, 6042 (1985).

[7] F. Diederich and R. L. Whetten, *Beyond C_{60}: The Higher Fullerenes*, Acc. Chem. Res. **25**, 119 (1992).

[8] S. Iijima, *Helical Microtubules of Graphitic Carbon*, Nature **354**, 6348 (1991).

[9] K. S. Novoselov, A. K. Geim, S. V. Morozov, D. Jiang, Y. Zhang, S. V. Dubonos, I. V. Grigorieva, and A. A. Firsov, *Electric Field Effect in Atomically Thin Carbon Films*, Science **306**, 666 (2004).

[10] S. Iijima, M. Yudasaka, R. Yamada, S. Bandow, K. Suenaga, F. Kokai, and K. Takahashi, *Nano-Aggregates of Single-Walled Graphitic Carbon Nano-Horns*, Chem. Phys. Lett. **309**, 165 (1999).

[11] D. V. Kosynkin, A. L. Higginbotham, A. Sinitskii, J. R. Lomeda, A. Dimiev, B. K. Price, and J. M. Tour, *Longitudinal Unzipping of Carbon Nanotubes to Form Graphene Nanoribbons*, Nature **458**, 872 (2009).

[12] G. Povie, Y. Segawa, T. Nishihara, Y. Miyauchi, and K. Itami, *Synthesis of a Carbon Nanobelt*, Science **356**, 172 (2017).

[13] L. Yang, H. Y. He, and B. C. Pan, *Theoretical Prediction of New Carbon Allotropes*, J. Chem. Phys. **138**, 024502 (2013).

[14] T. Tamura, T. Takami, S. Kobayashi, T. Nagahama, T. Yanase, and T. Shimada, *Formation of Bismuth-Core-Carbon-Shell Nanoparticles by Bismuth Immersion during Plasma CVD Synthesis of Thin Diamond Films*, Diam. Relat. Mater. **69**, 127 (2016).

[15] S. Suzuki, T. Nagamori, Y. Matsuoka, and M. Yoshimura, *Threefold Atmospheric-Pressure Annealing for Suppressing Graphene Nucleation on Copper in Chemical Vapor Deposition*, Jpn. J. Appl. Phys. **53**, 095101 (2014).

[16] J.-F. Colomer, C. Stephan, S. Lefrant, G. Van Tendeloo, I. Willems, Z. Kónya, A. Fonseca, C.

Laurent, and J. B. Nagy, *Large-Scale Synthesis of Single-Wall Carbon Nanotubes by Catalytic Chemical Vapor Deposition (CCVD) Method*, Chem. Phys. Lett. **317**, 83 (2000).

[17] T. Hayashi, Y. A. Kim, T. Matoba, M. Esaka, K. Nishimura, T. Tsukada, M. Endo, and M. S. Dresselhaus, *Smallest Freestanding Single-Walled Carbon Nanotube*, Nano Lett. **3**, 887 (2003).

[18] R. E. Haufler, J. Conceicao, L. P. F. Chibante, Y. Chai, N. E. Byrne, S. Flanagan, M. M. Haley, S. C. O'Brien, C. Pan, and . et al., *Efficient Production of C_{60} (Buckminsterfullerene), $C_{60}H_{36}$, and the Solvated Buckide Ion*, J. Phys. Chem. **94**, 8634 (1990).

[19] K. J. Hüttinger, *Coke Yield in Liquid-Phase Pyrolysis of Hydrocarbons from the Standpoint of Chemical Reaction Engineering Science*, Carbon **26**, 477 (1988).

[20] H. Takaba, H. Omachi, Y. Yamamoto, J. Bouffard, and K. Itami, *Selective Synthesis of [12]Cycloparaphenylene*, Angew. Chem. Int. Ed. **48**, 6112 (2009).

[21] Y. Segawa, T. Watanabe, K. Yamanoue, M. Kuwayama, K. Watanabe, J. Pirillo, Y. Hijikata, and K. Itami, *Synthesis of a Möbius Carbon Nanobelt*, Nat. Synth. **1**, 7 (2022).

[22] H. Kanda and K. Watanabe, *Distribution of the Cobalt-Related Luminescence Center in HPHT Diamond*, Diam. Relat. Mater. **6**, 708 (1997).

[23] H. M. Strong and R. E. Hanneman, *Crystallization of Diamond and Graphite*, J. Chem. Phys. **46**, 3668 (1967).

[24] F. P. Bundy, H. T. Hall, H. M. Strong, and R. H. Wentorfjun., *Man-Made Diamonds*, Nature **176**, 4471 (1955).

[25] T. Irifune, A. Kurio, S. Sakamoto, T. Inoue, and H. Sumiya, *Ultrahard Polycrystalline Diamond from Graphite*, Nature **421**, 6923 (2003).

[26] F. P. Bundy, *Direct Conversion of Graphite to Diamond in Static Pressure Apparatus*, J. Chem. Phys. **38**, 631 (1963).

[27] K. Muzyka, J. Sun, T. H. Fereja, Y. Lan, W. Zhang, and G. Xu, *Boron-Doped Diamond: Current Progress and Challenges in View of Electroanalytical Applications*, Anal. Methods **11**, 397 (2019).

[28] V. Acosta and P. Hemmer, *Nitrogen-Vacancy Centers: Physics and Applications*, MRS Bull. **38**, 127 (2013).

[29] E. A. Ekimov, M. V. Kondrin, V. S. Krivobok, A. A. Khomich, I. I. Vlasov, R. A. Khmelnitskiy, T. Iwasaki, and M. Hatano, *Effect of Si, Ge and Sn Dopant Elements on Structure and Photoluminescence of Nano- and Microdiamonds Synthesized from Organic Compounds*, Diam. Relat. Mater. **93**, 75 (2019).

[30] D. Guo, R. Shibuya, C. Akiba, S. Saji, T. Kondo, and J. Nakamura, *Active Sites of Nitrogen-Doped Carbon Materials for Oxygen Reduction Reaction Clarified Using Model Catalysts*, Science **351**, 361 (2016).

[31] Q. Wang, H. Wang, Y. Zhang, G. Wen, H. Liu, and D. Su, *Syntheses and Catalytic Applications of the High-N-Content, the Cup-Stacking and the Macroscopic Nitrogen Doped*

Carbon Nanotubes, J. Mater. Sci. Technol. **33**, 843 (2017).

[32] Y. Tang, B. L. Allen, D. R. Kauffman, and A. Star, *Electrocatalytic Activity of Nitrogen-Doped Carbon Nanotube Cups*, J. Am. Chem. Soc. **131**, 13200 (2009).

[33] B. Stöhr, H. P. Boehm, and R. Schlögl, *Enhancement of the Catalytic Activity of Activated Carbons in Oxidation Reactions by Thermal Treatment with Ammonia or Hydrogen Cyanide and Observation of a Superoxide Species as a Possible Intermediate*, Carbon **29**, 707 (1991).

[34] E. Lam and J. H. T. Luong, *Carbon Materials as Catalyst Supports and Catalysts in the Transformation of Biomass to Fuels and Chemicals*, ACS Catal. **4**, 3393 (2014).

[35] I. C. Gerber and P. Serp, *A Theory/Experience Description of Support Effects in Carbon-Supported Catalysts*, Chem. Rev. **120**, 1250 (2020).

[36] F. Rodríguez-reinoso, *The Role of Carbon Materials in Heterogeneous Catalysis*, Carbon **36**, 159 (1998).

[37] E. Auer, A. Freund, J. Pietsch, and T. Tacke, *Carbons as Supports for Industrial Precious Metal Catalysts*, Appl. Catal. A **173**, 259 (1998).

[38] S.-I. Hirano, T. Yogo, N. Nogami, and S. Naka, *Synthesis and Properties of Cobalt-Dispersed Carbons by Pressure Pyrolysis of Organocobalt Polymers*, J. Mater. Sci. **21**, 225 (1986).

[39] S. Dang, Q.-L. Zhu, and Q. Xu, *Nanomaterials Derived from Metal–Organic Frameworks*, Nat. Rev. Mater. **3**, 1 (2017).

[40] J. Su, R. Ge, Y. Dong, F. Hao, and L. Chen, *Recent Progress in Single-Atom Electrocatalysts: Concept, Synthesis, and Applications in Clean Energy Conversion*, J. Mater. Chem. A **6**, 14025 (2018).

[41] L. Zhang, Y. Wang, J. Lv, and Y. Ma, *Materials Discovery at High Pressures*, Nat. Rev. Mater. **2**, 17005 (2017).

[42] M. Miao, Y. Sun, E. Zurek, and H. Lin, *Chemistry under High Pressure*, Nat. Rev. Chem. 1 (2020).

[43] X. Wang and X. Liu, *High Pressure: A Feasible Tool for the Synthesis of Unprecedented Inorganic Compounds*, Inorg. Chem. Front. **7**, 2890 (2020).

[44] P. F. McMillan, *High Pressure Synthesis of Solids*, Curr. Opin. Solid State Mater. Sci. **4**, 171 (1999).

[45] D. K. Bradley, J. H. Eggert, R. F. Smith, S. T. Prisbrey, D. G. Hicks, D. G. Braun, J. Biener, A. V. Hamza, R. E. Rudd, and G. W. Collins, *Diamond at 800 GPa*, Phys. Rev. Lett. **102**, 075503 (2009).

[46] R. Cauble, D. W. Phillion, T. J. Hoover, N. C. Holmes, J. D. Kilkenny, and R. W. Lee, *Demonstration of 0.75 Gbar Planar Shocks in x-Ray Driven Colliding Foils*, Phys. Rev. Lett. **70**, 2102 (1993).

[47] G. A. Lyzenga, T. J. Ahrens, and A. C. Mitchell, *Shock Temperatures of SiO_2 and Their Geophysical Implications*, J. Geophys. Res. **88**, 2431 (1983).

[48] O. V. Fat'yanov and P. D. Asimow, *MgO Melting Curve Constraints from Shock Temperature*

and Rarefaction Overtake Measurements in Samples Preheated to 2300 K, J. Phys.: Conf. Ser. **500**, 062003 (2014).

[49] A. Lavergne and E. Whalley, *Steel Pressure Vessels for Hydrostatic Pressures to 50 Kilobars*, Rev. Sci. Instrum. **49**, 923 (1978).

[50] I. R. Walker, *Nonmagnetic Piston–Cylinder Pressure Cell for Use at 35 Kbar and Above*, Rev. Sci. Instrum. **70**, 3402 (1999).

[51] P. F. McMillan, *Pressing on: The Legacy of Percy W. Bridgman*, Nat. Mater. **4**, 10 (2005).

[52] A. Dewaele, P. Loubeyre, F. Occelli, O. Marie, and M. Mezouar, *Toroidal Diamond Anvil Cell for Detailed Measurements under Extreme Static Pressures*, Nat. Commun. **9**, 1 (2018).

[53] M. D. Banus and S. D. Nye, *Efficiency in a Tetrahedral-Anvil Press as Related to Anvil and Pyrophyllite Size*, Rev. Sci. Instrum. **35**, 1319 (1964).

[54] H. T. Hall, *Some High-Pressure, High-Temperature Apparatus Design Considerations: Equipment for Use at 100 000 Atmospheres and 3000°C*, Rev. Sci. Instrum. **29**, 267 (1958).

[55] K. Inoue and T. Asada, *Cubic Anvil X-Ray Diffraction Press Up to 100 Kbar and 1000°C*, Jpn. J. Appl. Phys. **12**, 1786 (1973).

[56] A. Sano-Furukawa, T. Hattori, H. Arima, A. Yamada, S. Tabata, M. Kondo, A. Nakamura, H. Kagi, and T. Yagi, *Six-Axis Multi-Anvil Press for High-Pressure, High-Temperature Neutron Diffraction Experiments*, Rev. Sci. Instrum. **85**, 113905 (2014).

[57] N. Kawai and S. Endo, *The Generation of Ultrahigh Hydrostatic Pressures by a Split Sphere Apparatus*, Rev. Sci. Instrum. **41**, 1178 (1970).

[58] F.-G. Klärner and F. Wurche, *The Effect of Pressure on Organic Reactions*, J. Prackt. Chem. **342**, 609 (2000).

[59] B. Chen, R. Hoffmann, and R. Cammi, *The Effect of Pressure on Organic Reactions in Fluids—a New Theoretical Perspective*, Angew. Chem. Int. Ed. **56**, 11126 (2017).

[60] H. Kotsuki, H. Nishizawa, S. Kitagawa, M. Ochi, N. Yamasaki, K. Matsuoka, and T. Tokoroyama, *High Pressure Organic Chemistry. III. Diels-Alder Reaction of Thiophene with Maleic Anhydride*, Bull. Chem. Soc. Jpn. **52**, 544 (1979).

[61] T. Thiemann, D. Ohira, Y. Li, T. Sawada, S. Mataka, K. Rauch, M. Noltemeyer, and A. de Meijere, *[4+2] Cycloaddition of Thiophene S-Monoxides to Activated Methylenecyclopropanes*, J. Chem. Soc., Perkin Trans. 1 2968 (2000).

[62] M. Bellassoued, E. Reboul, and F. Dumas, *High Pressure Induced Mukaiyama Type Aldol Reaction of Bis Trimethylsilyl Ketene Acetals*, Tetrahedron Lett. **38**, 5631 (1997).

[63] G. Jenner, *Phosphine-Catalyzed Dimerization of Activated Alkenes under Ambient and High Pressure Conditions*, Tetrahedron Lett. **41**, 3091 (2000).

[64] Cheves. Walling and Michael. Naiman, *Organic Reactions under High Pressure. VI. Some Claisen and Cope Rearrangements*, J. Am. Chem. Soc. **84**, 2628 (1962).

[65] T. Shimizu, R. Kobayashi, H. Ohmori, and T. Nakata, *Synthesis of Dicarboxylic Monoesters with Cyclic Anhydrides under High Pressure*, Synlett **1995**, 650 (1995).

[66] X. Yang, X. Wang, Y. Wang, K. Li, and H. Zheng, *From Molecules to Carbon Materials-High Pressure Induced Polymerization and Bonding Mechanisms of Unsaturated Compounds*, Crystals **9**, 490 (2019).

[67] F. Li, J. Xu, Y. Wang, H. Zheng, and K. Li, *Pressure-Induced Polymerization: Addition and Condensation Reactions*, Molecules **26**, 24 (2021).

[68] V. Schettino and R. Bini, *Constraining Molecules at the Closest Approach: Chemistry at High Pressure*, Chem. Soc. Rev. **36**, 869 (2007).

[69] V. Schettino and R. Bini, *Molecules under Extreme Conditions: Chemical Reactions at High Pressure*, Phys. Chem. Chem. Phys. **5**, 1951 (2003).

[70] P. Zhang et al., *Distance-Selected Topochemical Dehydro-Diels–Alder Reaction of 1,4-Diphenylbutadiyne toward Crystalline Graphitic Nanoribbons*, J. Am. Chem. Soc. **142**, 17662 (2020).

[71] J. Sun et al., *Pressure-Induced Polymerization of Acetylene: Structure-Directed Stereoselectivity and a Possible Route to Graphane*, Angew. Chem. Int. Ed. **56**, 6553 (2017).

[72] K. Aoki, S. Usuba, M. Yoshida, Y. Kakudate, K. Tanaka, and S. Fujiwara, *Raman Study of the Solid-state Polymerization of Acetylene at High Pressure*, J. Chem. Phys. **89**, 529 (1988).

[73] D. Chelazzi, M. Ceppatelli, M. Santoro, R. Bini, and V. Schettino, *Pressure-Induced Polymerization in Solid Ethylene*, J. Phys. Chem. B **109**, 21658 (2005).

[74] D. Gourdain, J. C. Chervin, and Ph. Pruzan, *Transformations of Styrene at High Pressure*, J. Chem. Phys. **105**, 9040 (1996).

[75] H. Zheng et al., *Polymerization of Acetonitrile via a Hydrogen Transfer Reaction from CH3 to CN under Extreme Conditions*, Angew. Chem. Int. Ed. **55**, 12040 (2016).

[76] M. Citroni, M. Ceppatelli, R. Bini, and V. Schettino, *The High-Pressure Chemistry of Butadiene Crystal*, J. Chem. Phys. **118**, 1815 (2003).

[77] Ph. Pruzan, J. C. Chervin, M. M. Thiéry, J. P. Itié, J. M. Besson, J. P. Forgerit, and M. Revault, *Transformation of Benzene to a Polymer after Static Pressurization to 30 GPa*, J. Chem. Phys. **92**, 6910 (1990).

[78] L. Ciabini, M. Santoro, F. A. Gorelli, R. Bini, V. Schettino, and S. Raugei, *Triggering Dynamics of the High-Pressure Benzene Amorphization*, Nat. Mater. **6**, 1 (2007).

[79] X. Li et al., *Carbon Nitride Nanothread Crystals Derived from Pyridine*, J. Am. Chem. Soc. **140**, 4969 (2018).

[80] T. Yasuzuka, K. Komatsu, and H. Kagi, *A Revisit to High-Pressure Transitions of Pyridine: A New Phase Transition at 5 GPa and Formation of a Crystalline Phase over 20 GPa*, Chem. Lett. **40**, 733 (2011).

[81] P. Ray, J. L. Gray, J. V. Badding, and A. D. Lueking, *High-Pressure Reactivity of Triptycene Probed by Raman Spectroscopy*, J. Phys. Chem. B **120**, 11035 (2016).

[82] Y. Wang et al., *Phase Transitions and Polymerization of C_6H_6–C_6F_6 Cocrystal under Extreme Conditions*, J. Phys. Chem. C **120**, 29510 (2016).

[83] Y. Wang et al., *Pressure-Induced Diels–Alder Reactions in C_6H_6-C_6F_6 Cocrystal towards Graphane Structure*, Angew. Chem. Int. Ed. **58**, 1468 (2019).

[84] B. Sundqvist, *Buckyballs under Pressure*, Phys. Stat. Sol. (b) **223**, 469 (2001).

[85] B. Sundqvist, *Intermolecular Bonding in C_{70} at High Pressure and Temperature*, Carbon **125**, 258 (2017).

[86] W. Cui, B. Sundqvist, S. Sun, M. Yao, and B. Liu, *High Pressure and High Temperature Induced Polymerization of Doped C_{60} Materials*, Carbon **109**, 269 (2016).

[87] W. Cui et al., *Reversible Pressure-Induced Polymerization of $Fe(C_5H_5)_2$ Doped C_{70}*, Carbon **62**, 447 (2013).

[88] Y. Kojima, M. Tsuji, T. Matsuoka, and H. Takahashi, *High-Pressure Synthesis of Polyacene-Based Oligomer*, Macromolecules **27**, 3735 (1994).

[89] A. Shinozaki, K. Mimura, H. Kagi, K. Komatu, N. Noguchi, and H. Gotou, *Pressure-Induced Oligomerization of Benzene at Room Temperature as a Precursory Reaction of Amorphization*, J. Chem. Phys. **141**, 084306 (2014).

[90] A. D. Chanyshev, K. D. Litasov, A. F. Shatskiy, Y. Furukawa, T. Yoshino, and E. Ohtani, *Oligomerization and Carbonization of Polycyclic Aromatic Hydrocarbons at High Pressure and Temperature*, Carbon **84**, 225 (2015).

[91] A. Shinozaki, K. Mimura, T. Nishida, T. Inoue, S. Nakano, and H. Kagi, *Stability and Partial Oligomerization of Naphthalene under High Pressure at Room Temperature*, Chem. Phys. Lett. **662**, 263 (2016).

[92] A. D. Chanyshev, K. D. Litasov, Y. Furukawa, K. A. Kokh, and A. F. Shatskiy, *Temperature-Induced Oligomerization of Polycyclic Aromatic Hydrocarbons at Ambient and High Pressures*, Sci. Rep. **7**, 7889 (2017).

[93] A. Shinozaki, K. Mimura, and T. Nishida, *Decomposition and Oligomerization of 2,3-Naphthyridine under High-Pressure and High-Temperature Conditions*, Sci. Rep. **9**, 7335 (2019).

[94] A. Shinozaki, K. Mimura, T. Nishida, and G. D. Cody, *Polymerization Mechanism of Nitrogen-Containing Heteroaromatic Compound Under High-Pressure and High-Temperature Conditions*, J. Phys. Chem. A **125**, 376 (2021).

[95] S. C. Abrahams, J. M. Robertson, and J. G. White, *The Crystal and Molecular Structure of Naphthalene. I. X-Ray Measurements*, Acta. Cryst. **2**, 4 (1949).

[96] V. A. Davydov, A. V. Rakhmanina, V. Agafonov, B. Narymbetov, J.-P. Boudou, and H. Szwarc, *Conversion of Polycyclic Aromatic Hydrocarbons to Graphite and Diamond at High Pressures*, Carbon **42**, 261 (2004).

[97] R. B. Aust, W. H. Bentley, and H. G. Drickamer, *Behavior of Fused-Ring Aromatic Hydrocarbons at Very High Pressure*, J. Chem. Phys. **41**, 1856 (1964).

[98] A. D. Chanyshev, K. D. Litasov, A. F. Shatskiy, I. S. Sharygin, Y. Higo, and E. Ohtani, *Transition from Melting to Carbonization of Naphthalene, Anthracene, Pyrene and Coronene*

at High Pressure, Phys. Earth Planet. Inter. **270**, 29 (2017).

[99] R. H. Jr. Wentorf, *The Behavior of Some Carbonaceous Materials at Very High Pressures and High Temperatures*, J. Phys. Chem. **69**, 3063 (1965).

[100] E. A. Ekimov, S. G. Lyapin, Yu. V. Grigoriev, I. P. Zibrov, and K. M. Kondrina, *Size-Controllable Synthesis of Ultrasmall Diamonds from Halogenated Adamantanes at High Static Pressure*, Carbon **150**, 436 (2019).

[101] E. A. Ekimov, O. S. Kudryavtsev, N. E. Mordvinova, O. I. Lebedev, and I. I. Vlasov, *High-Pressure Synthesis of Nanodiamonds from Adamantane: Myth or Reality?*, ChemNanoMat **4**, 269 (2018).

[102] J. Guignard, M. Prakasam, and A. Largeteau, *A Review of Binderless Polycrystalline Diamonds: Focus on the High-Pressure–High-Temperature Sintering Process*, Materials **15**, 6 (2022).

[103] S. Kumar, V. R. Battula, and K. Kailasam, *Single Molecular Precursors for C_xN_y Materials-Blending of Carbon and Nitrogen beyond g-C_3N_4*, Carbon **183**, 332 (2021).

[104] E. Horvath-Bordon, R. Riedel, A. Zerr, P. F. McMillan, G. Auffermann, Y. Prots, W. Bronger, R. Kniep, and P. Kroll, *High-Pressure Chemistry of Nitride-Based Materials*, Chem. Soc. Rev. **35**, 987 (2006).

[105] E. Kroke and M. Schwarz, *Novel Group 14 Nitrides*, Coord. Chem. Rev. **248**, 493 (2004).

[106] M. L. Cohen, *Calculation of Bulk Moduli of Diamond and Zinc-Blende Solids*, Phys. Rev. B **32**, 7988 (1985).

[107] A. Y. Liu and M. L. Cohen, *Prediction of New Low Compressibility Solids*, Science **245**, 841 (1989).

[108] E. Horvath-Bordon et al., *High-Pressure Synthesis of Crystalline Carbon Nitride Imide, $C_2N_2(NH)$*, Angew. Chem. Int. Ed. **46**, 1476 (2007).

[109] Z. Zhang, K. Leinenweber, M. Bauer, L. A. J. Garvie, P. F. McMillan, and G. H. Wolf, *High-Pressure Bulk Synthesis of Crystalline $C_6N_9H_3{\cdot}HCl$: A Novel C_3N_4 Graphitic Derivative*, J. Am. Chem. Soc. **123**, 7788 (2001).

[110] T. Horibe, K. Kusaba, K. Niwa, M. Hasegawa, K. Yasuda, and R. Ishigami, *Molecular Routes Syntheses of Graphite-like C–N Compounds with Various N/C Ratios in High Pressure and Temperature*, J. Ceram. Soc. JAPAN **124**, 1013 (2016).

[111] H. A. Ma et al., *High-Pressure Pyrolysis Study of $C_3N_6H_6$: A Route to Preparing Bulk C_3N_4*, J. Phys.: Condens. Matter **14**, 11269 (2002).

[112] X. Yuan, K. Luo, Y. Wu, J. He, Z. Zhao, and D. Yu, *Investigation on the Stability of Derivative Melam from Melamine Pyrolysis under High Pressure*, Nanomaterials **8**, 3 (2018).

Chapter 2 Search for new nitrogen-doped carbon materials by compressing molecular crystals

2.1 Introduction

Nitrogen (N)-doped carbon materials exhibit various useful properties, such as catalytic activity [1,2], magnetism [3,4] hydrogen storage [5]. These properties are determined by factors including the hybridization of atoms, the structure of carbon skeleton, and the position of nitrogen species. New materials will be obtained by controlling these factors.

High-pressure synthesis is a versatile tool for creating new materials. Under high pressure, interatomic distances are reduced, and electronic structure is modified [6]. Metastable materials can be synthesized using those effects. There are some reports on the high-pressure processing of organic molecules to make carbon solids. Three-dimensional topotactic polymerization of C60 fullerene is an example [7]. Very hard materials are obtained by the polymerization of co-crystal between fullerene and other molecules [8–11]. Photocatalytic graphitic-carbon nitride changed bandgap by compression due to the holes vanishing in the carbon-nitrogen networks [12]. When aromatic molecular solids are placed under high pressure, it is expected that a Diels–

Alder-like reaction occurs and the molecules polymerize or oligomerize. This type of reaction on simple aromatic molecules has been reported [13–19]. However, to the authors' knowledge, those of heteroatom-containing polycyclic aromatic molecules have rarely been reported.

In order to investigate the reactions of heterocyclic aromatic compounds compressed under high pressure and explore the possibility of synthesizing new N-doped carbon materials, I carried out experiments compressing N-containing aromatic molecules under ultrahigh pressure. [20] In this paper, I examine the experimental data in detail with the aid of density functional theory (DFT) calculations.

2.2 Experimental and computational section

2.2.1 Sample preparation

I carried out high-pressure experiments using a cubic anvil press and used organic molecules as precursors. The precursors were quinoxalino[2′,3′:9,10] phenanthro[4,5-abc] phenazine (TQPP) and dibenzo[a,c]dibenzo[5,6:7,8]quinoalino[2,3-i] phenazine (DDQP). The molecular structures of TQPP and DDQP are shown in Figure 2-1. I made single crystals of these molecules and analyzed their crystal structure by X-ray diffraction (XRD). The results agreed with the previous reports [21,22]. They have a herringbone structure. Crystalline powders of precursors were used in the high-pressure

experiments.

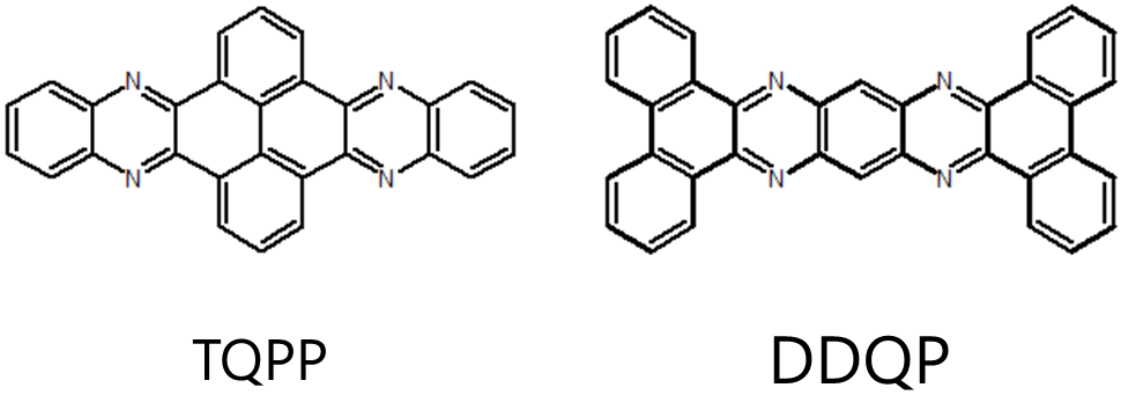

Figure 2-1 Molecular structure of TQPP (left) and DDQP (right)

The precursor molecules were encapsulated in cylindrical copper vessels, which were then placed in a pyrophyllite cube. The cell assembly was compressed to 5 GPa at room temperature using cubic anvil apparatus. The pressure was ramped from ambient to 5 GPa in 60 min, and subsequently, it was retained for 24 h. Finally, it was decreased to ambient pressure in 90 min, and the sample was recovered from the cell assembly.

2.2.2 Characterization

The recovered samples were characterized by matrix-assisted laser deposited ionization time-of-flight mass spectroscopy (MALDI-TOF-MS), Fourier transform infrared spectroscopy (FT-IR) and powder XRD.

2.2.3 DFT calculation

In addition to the high-pressure experiments, I attempted DFT calculations in order to

investigate the structures of products. The simulation of high-pressure treatment to molecular crystals was carried out in the following way. First, I used crystal structures determined by the single crystal XRD as starting structures. Next, the cell size was reduced step by step by 5% in length. At each step, the lattice parameters and atom positions were optimized by DFT calculations by fixing the cell volume. Symmetry constraint was not used. The pressure was obtained as a result of the calculation. This method was used to investigate the difference between two molecules using a minimum amount of computation. All the calculations in this work were carried out using Vienna Ab initio Simulation Package [23] (VASP) which is based on DFT, plane waves, and pseudopotentials. Our calculation was performed with the projector augmented wave method and the exchange–correlation energy treated using the Perdew–Burke–Ernzerhof (PBE) functional [24] based on the generalized gradient approximation (GGA). The cutoff energy was 400 eV.

2.3 Results and discussion

MALDI-TOF-MS measurements were performed to investigate the contents of the samples after high-pressure compression. Mass spectra of the samples after 5 GPa compression are shown in Figure 2-2. In the spectrum of the compressed TQPP, peaks were observed at m/z = 405.552 and 811.286. These peaks correspond to the TQPP

monomer and TQPP dimer, respectively, because the molecular weight of TQPP is 406.438. In the spectrum of the compressed DDQP, two main peaks and some small peaks were observed. The molecular weight of DDQP is 482.553, and two main peaks at *m*/*z* = 481.540 and 963.546 are assigned to the DDQP monomer and dimer, respectively. In addition, a peak was found at m/z = 1444.392. This corresponds to the DDQP trimer. It is considered that other intermediate peaks correspond to fragments. The results indicate that the samples after high-pressure processing contain oligomers of precursor molecules. However, the yield of oligomerization was not very high, and unreacted precursors were observed in the product.

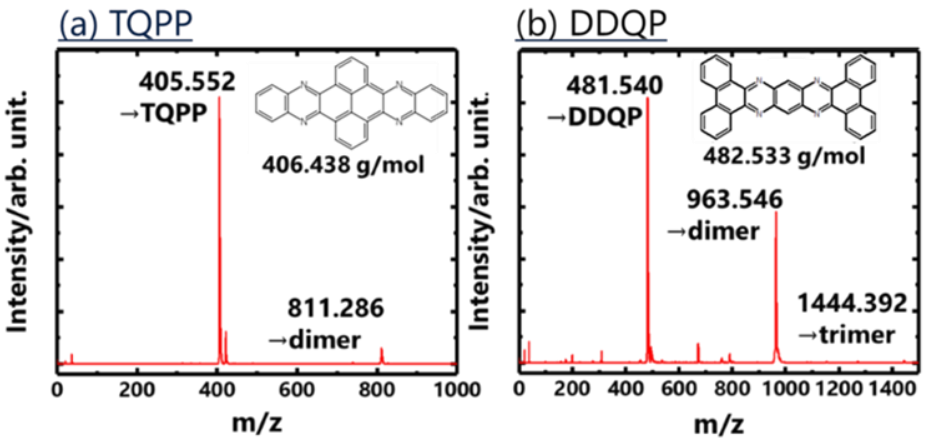

Figure 2-2 Mass spectra of (a) TQPP and (b) DDQP samples after high pressure treatments.

The results of FT-IR measurements of the precursors and the samples after applying 5 GPa (measured at ambient pressure) are shown in Figure 2-3. In the TQPP [Figure 2-3 (a)], the IR spectrum changed, and new absorption bands were observed. However, it is difficult to identify these new absorption bands. Changes were also observed in the spectra of the DDQP samples [Figure 2-3(b)]. In the spectrum of the sample after compression, absorption around 900–675 cm^{-1} was significantly decreased compared with that of the precursor. Additionally, a new absorption band was observed in 3000–2840 cm^{-1} in the DDQP after compression. Absorptions around 900–675 cm^{-1} and 3000–2840 cm^{-1} correspond to C–H out-of-plane deformation of the aromatic ring and C–H stretching of alkane, respectively. These changes indicate that carbon atoms of DDQP molecules transformed from sp^2 -hybridization to sp^3, which is consistent with the oligomerization. On the other hand, the features mentioned above were not clearly observed in the spectra of the TQPP. It probably corresponds to the low yield of the pressure-induced oligomerization of the TQPP.

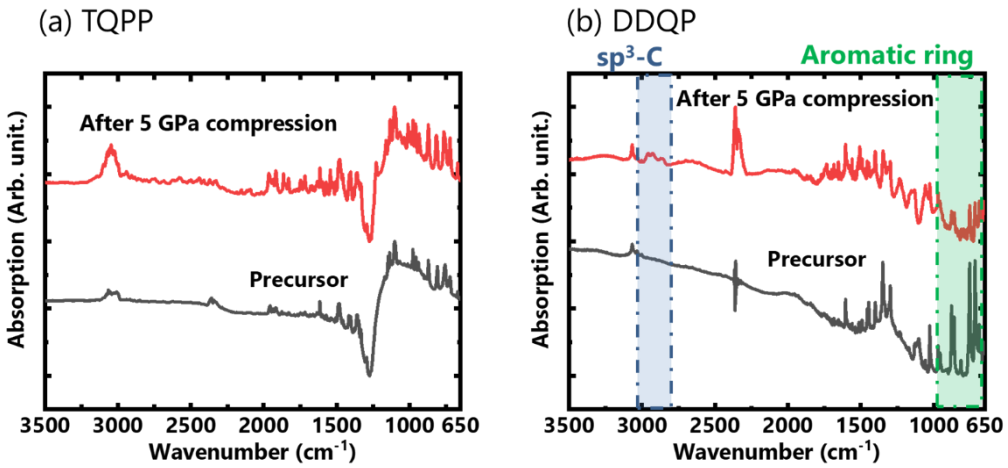

Figure 2-3 IR spectra of precursors (black line) and the samples after 5 GPa application (red line; measured at ambient pressure). (a) TQPP, (b) DDQP. Green and blue areas in the spectra of DDQP are assigned to absorption of CH out-of-plane deformation of the aromatic ring and CH stretching of alkane, respectively.

Figure 2-4 shows powder XRD patterns before and after high-pressure processing, both measured under ambient pressure. In both cases of TQPP and DDQP, XRD patterns changed after compression. It is remarkable that sharp peaks were observed in the patterns of the samples after the compression. It indicates that the samples did not become amorphous by high-pressure treatment. Thus, the application of 5 GPa changed the crystal structures, but the long-range order was retained.

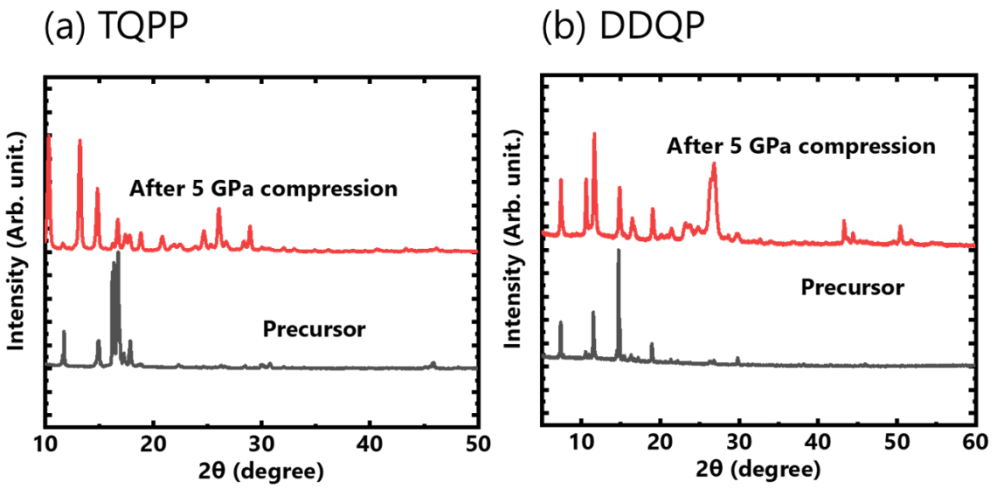

Figure 2-4 Powder XRD patterns of precursors (black line) and the samples after 5 GPa application (red line; measured at ambient pressure). (a) TQPP, (b) DDQP.

From the experimental results, I concluded that the oligomerization occurred associated with the change in hybridization from sp^2 to sp^3. In order to obtain information on the detail of the reaction, I performed simulations using DFT calculations. In order to analyze the oligomerization and structure of the product, a structural optimization calculation was performed starting from the structure of precursor crystal obtained by single crystal XRD. However, a structure in which the A axis of the unit cell was doubled was used as the supercell for the calculation to increase the number of molecules contained in the cell .When structural optimization was finished at each step of reducing cell volume, the vertical pressure applied to each surface was calculated (Table 2-1). Since the values are almost uniform, these calculations successfully simulated quasi-hydrostatic compression. In the simulation of

compressing TQPP crystal, TQPP molecules were not polymerized when the cell volume was 72.9% (=(90%)^3 , 13.4 GPa) of the original one but polymerized when it was 51.2% (=(80%)^3, 42.5 GPa). The discrepancy between the experiment (partial dimerization observed at 5 GPa) and calculation (total polymerization occurred between 13.4 and 35.5 GPa) remains unclarified. Our tentative speculation about the discrepancy is the limitation in the computational accuracy without precise treatment of van der Waals forces. I consider that the high pressure needed for polymerization reflects the difficulty of intermolecular-bond formation compared with DDQP, as described later. The calculated structure of TQPP after polymerization is shown in Figure 2-5. This simulation was performed using a unit cell of TQPP with three-dimensional periodicity. The polymers had a column-like one-dimensional structure, although the force was applied to each surface uniformly. Carbon and nitrogen atoms of the polymer were in sp^3 hybridization. The crystal system of the structure remained monoclinic. The substructure composed of two molecules extracted from the TQPP polymer are shown in Figure 2-6 (a)-(c). The structure of the TQPP dimer is likely to be based on the substructure. However, The bond cleavage and hydrogen atom transfer could occur during the polymer decomposition to dimer because this substructure as it is would result in inconsistencies in bond valences. Figure 2-6 (d) shows one of the several possible dimer structures that can be estimated in this way.

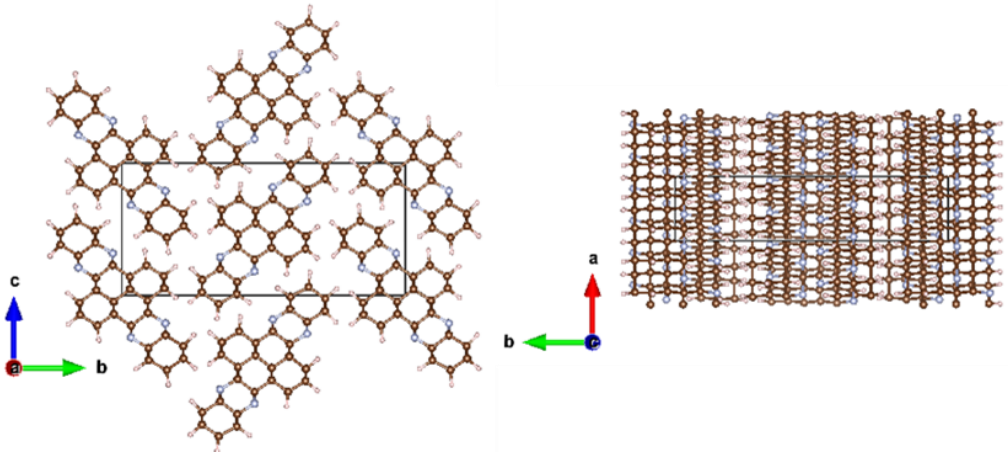

Figure 2-5 Calculated structure of compressed TQPP

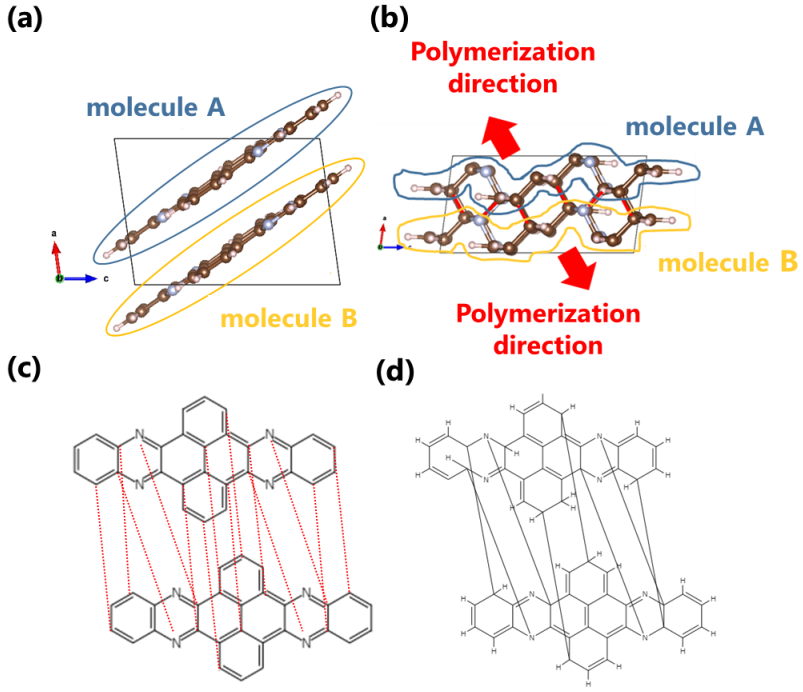

Figure 2-6 (a) the TQPP crystal structure at ambient pressure. (b) the structure of TQPP polymer obtained from the calculation. The red bonds represent newly formed intermolecular bonds due to polymerization. (c) Indication of intermolecular bonds in TQPP polymer by structural formula. Red dotted lines represent the intermolecular bonds. (d) An example of the predicted structure of the TQPP dimer, based on (c).

Table 2-1 The variation of the lattice parameters and pressures during compression

	Lattice constants						Pressures/GPa		
	a/Å	*b*/Å	*c*/Å	*α*/deg.	*β*/deg.	*γ*/deg.	*a*	*b*	*C*
TQPP (starting structure)	7.70	21.6	10.7	90.0	98.0	90.0	–	–	–
TQPP (72.9% cell volume) not polymerized	6.58	20.1	9.74	90.0	92.1	90.0	13.3	13.3	13.3
TQPP (51.2% cell volume) polymerized	4.77	20.2	9.46	90.0	82.4	90.0	42.4	42.6	42.5
DDQP (starting structure)	7.56	16.6	17.1	90.0	95.3	90.0	–	–	–
DDQP (72.9% cell volume) not polymerized	6.49	15.5	15.7	90.0	99.7	90.0	12.6	12.7	12.6
DDQP (61.4% cell volume) polymerized	5.46	14.9	16.2	90.0	92.6	90.0	15.2	15.0	15.0

DDQP was also polymerized in the calculation. Figure 2-7 shows the structure of the polymer. It is dissimilar to that of TQPP. DDQP polymers have cross-linking bonds between columns and result in the formation of a 3D network structure. This polymerization was not observed when the cell volume was 72.9% ((=90%)3) of the original and completed when 61.4% (=(85%)3). The calculated pressures before and after the polymerizations were 13.1 GPa at 72.9% and 11.7 GPa was 61.4%, respectively (Table 2-1). The inter-molecular distance was decreased by compression and Diels– Alder-like bonds generated between aromatic rings (Figure 2-8). Examples of the structures DDQP dimer and trimer inferred from that of DDQP polymer obtained

are shown in Figure 2-9. According to the DFT calculation, TQPP polymerizes under compression. However, the TQPP dimer was only obtained as a minor product in the experiment, and the unreacted precursor remained as the main component. There are two possible explanations. One is that the applied pressure (5 GPa) was not enough, which is suggested by the calculation. Another is that the polymerization is reversible, and the polymer decomposes into a monomer and dimer while releasing the pressure. A phenomenon similar to the latter was reported in benzene under the high-pressure process. Higher pressure and high temperature are probably necessary to achieve irreversible polymerization to make nitrogen-doped new carbon solids. DDQP shows much lower pressure for the polymerization compared to TQPP in the DFT calculation, and it agrees with the experiment.

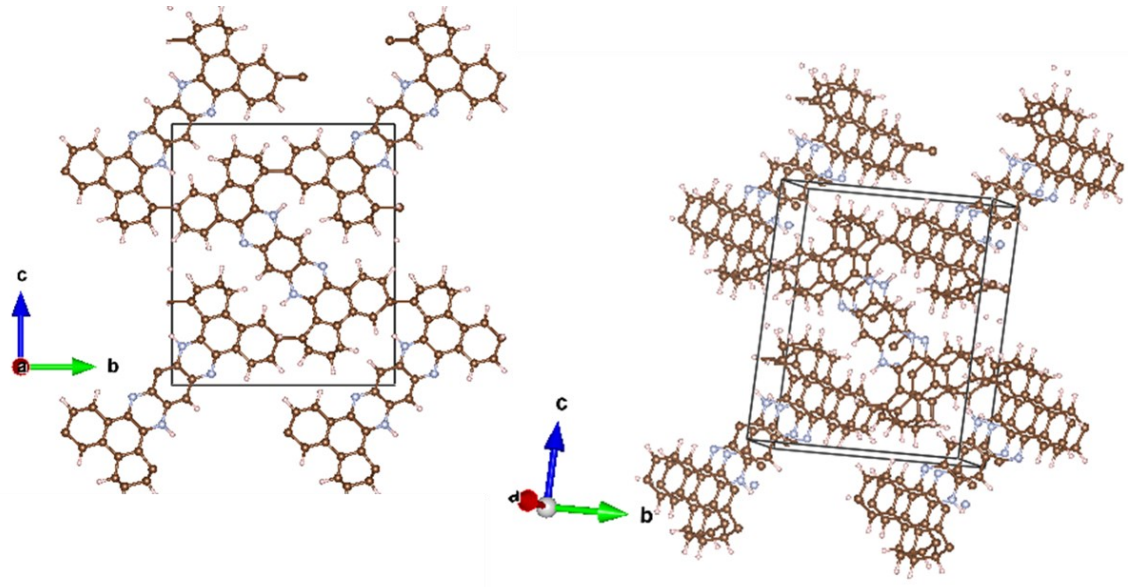

Figure 2-7 Calculated structure of compressed DDQP.

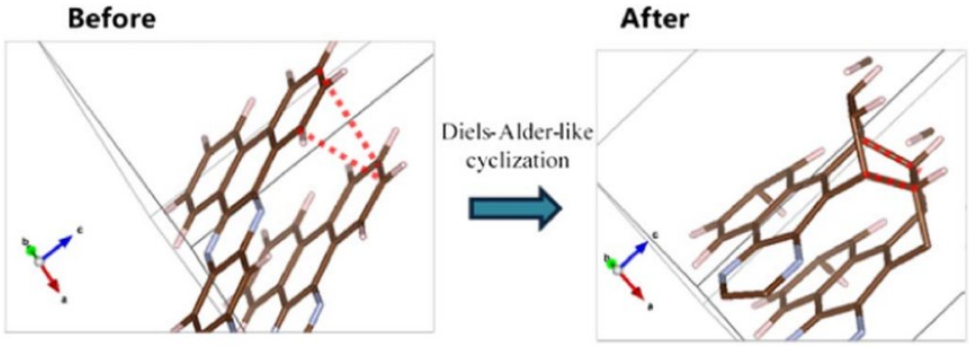

Figure 2-8 The comparison of the structure of DDQP at ambient pressure (left) and the structure obtained before simulating compression (right).

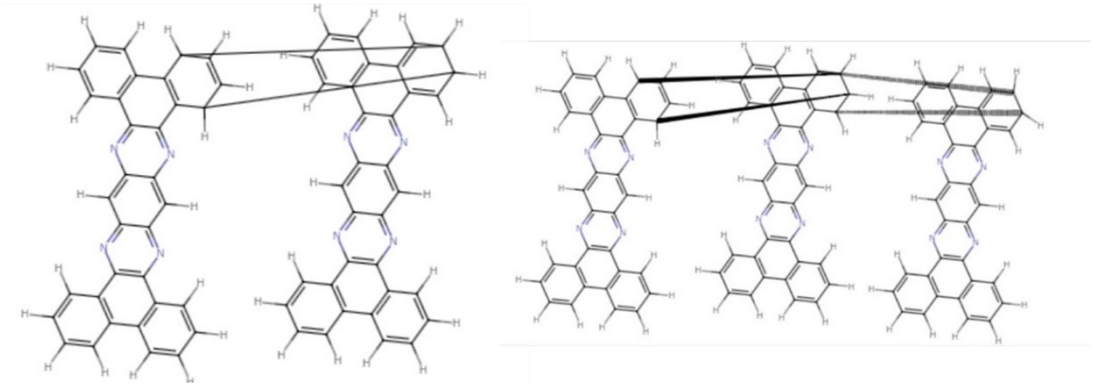

Figure 2-9 an example of the predicted structure of DDQP dimer (left) and trimer (right).

2.4 Conclusions

Crystals of N-doped polyacene TQPP and DDQP were compressed to 5 GPa at room temperature for 24 h using a cubic anvil press. After releasing the samples at room temperature, both molecules underwent pressure-induced oligomerization. In the oligomerization of DDQP, FT-IR showed that carbon atoms of DDQP transformed from sp^2- to sp^3- hybridization.

The present results demonstrate that molecules with complex structures can oligomerize by just applying pressure. It will be a promising approach to create new

carbon-based materials with useful functions because the high-pressure treatment is versatile.

References

[1] D. Guo, R. Shibuya, C. Akiba, S. Saji, T. Kondo, and J. Nakamura, *Active Sites of Nitrogen-Doped Carbon Materials for Oxygen Reduction Reaction Clarified Using Model Catalysts*, Science **351**, 361 (2016).

[2] M. Z. Rahman, J. Ran, Y. Tang, M. Jaroniec, and S. Z. Qiao, *Surface Activated Carbon Nitride Nanosheets with Optimized Electro-Optical Properties for Highly Efficient Photocatalytic Hydrogen Production*, J. Mater. Chem. A **4**, 2445 (2016).

[3] V. Acosta and P. Hemmer, *Nitrogen-Vacancy Centers: Physics and Applications*, MRS Bull. **38**, 127 (2013).

[4] N. Mohanty, D. Moore, Z. Xu, T. S. Sreeprasad, A. Nagaraja, A. A. Rodriguez, and V. Berry, *Nanotomy-Based Production of Transferable and Dispersible Graphene Nanostructures of Controlled Shape and Size*, Nat. Commun. **3**, 844 (2012).

[5] X. D. Bai, D. Zhong, G. Y. Zhang, X. C. Ma, S. Liu, E. G. Wang, Y. Chen, and D. T. Shaw, *Hydrogen Storage in Carbon Nitride Nanobells*, Appl. Phys. Lett. **79**, 1552 (2001).

[6] L. Zhang, Y. Wang, J. Lv, and Y. Ma, *Materials Discovery at High Pressures*, Nat. Rev. Mater. **2**, 17005 (2017).

[7] S. Yamanaka, N. S. Kini, A. Kubo, S. Jida, and H. Kuramoto, *Topochemical 3D Polymerization of C_{60} under High Pressure at Elevated Temperatures*, J. Am. Chem. Soc. **130**, 4303 (2008).

[8] W. Cui, S. Sun, B. Sundqvist, S. Wang, and B. Liu, *Pressure Induced Metastable Polymerization in Doped C60 Materials*, Carbon **115**, 740 (2017).

[9] W. Cui, B. Sundqvist, S. Sun, M. Yao, and B. Liu, *High Pressure and High Temperature Induced Polymerization of Doped C_{60} Materials*, Carbon **109**, 269 (2016).

[10] W. Cui et al., *Reversible Pressure-Induced Polymerization of $Fe(C_5H_5)_2$ Doped C_{70}*, Carbon **62**, 447 (2013).

[11] M. Yao et al., *Tailoring Building Blocks and Their Boundary Interaction for the Creation of New, Potentially Superhard, Carbon Materials*, Adv. Mater. **27**, 3962 (2015).

[12] Z. Yang et al., *Tuning the Band Gap and the Nitrogen Content in Carbon Nitride Materials by High Temperature Treatment at High Pressure*, Carbon **130**, 170 (2018).

[13] Y. Kojima, M. Tsuji, T. Matsuoka, and H. Takahashi, *High-Pressure Synthesis of Polyacene-Based Oligomer*, Macromolecules **27**, 3735 (1994).

[14] A. D. Chanyshev, K. D. Litasov, A. F. Shatskiy, Y. Furukawa, T. Yoshino, and E. Ohtani, *Oligomerization and Carbonization of Polycyclic Aromatic Hydrocarbons at High Pressure and Temperature*, Carbon **84**, 225 (2015).

[15] A. Shinozaki, K. Mimura, T. Nishida, T. Inoue, S. Nakano, and H. Kagi, *Stability and Partial Oligomerization of Naphthalene under High Pressure at Room Temperature*, Chem. Phys. Lett. **662**, 263 (2016).

[16] B. Chen, R. Hoffmann, N. W. Ashcroft, J. Badding, E. Xu, and V. Crespi, *Linearly Polymerized Benzene Arrays As Intermediates, Tracing Pathways to Carbon Nanothreads*, J. Am. Chem. Soc. **137**, 14373 (2015).

[17] A. Shinozaki, K. Mimura, H. Kagi, K. Komatu, N. Noguchi, and H. Gotou, *Pressure-Induced Oligomerization of Benzene at Room Temperature as a Precursory Reaction of Amorphization*, J. Chem. Phys. **141**, 084306 (2014).

[18] J. Sun et al., *Pressure-Induced Polymerization of Acetylene: Structure-Directed Stereoselectivity and a Possible Route to Graphane*, Angew. Chem. Int. Ed. **56**, 6553 (2017).

[19] Y. Wang et al., *Phase Transitions and Polymerization of C_6H_6–C_6F_6 Cocrystal under Extreme Conditions*, J. Phys. Chem. C **120**, 29510 (2016).

[20] I. Yamane, T. Yanase, T. Nagahama, and T. Shimada, *Search for New Nitrogen-Doped Carbon Materials by Compressing Molecular Crystals*, in (2018), p. K-08-02.

[21] P.-Y. Gu, Z. Wang, G. Liu, H. Yao, Z. Wang, Y. Li, J. Zhu, S. Li, and Q. Zhang, *Synthesis, Full Characterization, and Field Effect Transistor Behavior of a Stable Pyrene-Fused N-Heteroacene with Twelve Linearly Annulated Six-Membered Rings*, Chem. Mater. **29**, 4172 (2017).

[22] B. Wex, A. O. El-Ballouli, A. Vanvooren, U. Zschieschang, H. Klauk, J. A. Krause, J. Cornil, and B. R. Kaafarani, *Crystalline TQPP as P-Type Semiconductor: X-Ray Crystallographic Investigation, OTFT Device, and Computational Analysis of Transport Properties*, J. Mol. Struct. **1093**, 144 (2015).

[23] G. Kresse and J. Furthmüller, *Efficient Iterative Schemes for Ab Initio Total-Energy Calculations Using a Plane-Wave Basis Set*, Phys. Rev. B **54**, 11169 (1996).

[24] J. P. Perdew, K. Burke, and M. Ernzerhof, *Generalized Gradient Approximation Made Simple*, Phys. Rev. Lett. **77**, 3865 (1996).

Chapter 3 Ultrahigh-pressure preparation and catalytic activity of MOF-derived Cu nanoparticles

3.1 Introduction

Solid-state copper shows important catalytic functions in organic synthesis [1–8], graphene synthesis [9,10], electrochemical reduction of carbon dioxide [11,12], and purification of automobile exhaust [13,14]. Although group 11 elements in the periodic table show important catalytic activities [15], copper is unique among them because of its natural abundance. For heterogeneous catalysts, nanoparticles (NPs) of active components are desired because a large number of active sites are provided owing to the high surface-to-volume ratio in NPs [16,17]. Various methods for the preparation of Cu nanoparticles have been proposed [18]. Among them, metal–organic framework (MOF)-derived metal-carbon composites are recently gathering attention because it is conceptually possible to prepare materials with designed nanostructures [19–22]. These materials are synthesized by the pyrolysis of MOFs. This method is attractive for the preparation of supported metal NPs because the active site and carrier can be synthesized simultaneously; namely, the metal cations and the ligands in the MOF are converted to metal (or metal-based) NPs and carbon matrix, respectively. However, since the carbonization process involves thermal decomposition of the organic ligands,

the products are sensitive to the process parameters. Copper atoms can aggregate to make Cu NPs by pyrolysis because copper does not form stable carbides. However, previous reports show that the pyrolysis of a Cu-containing MOF gives Cu NPs tens of nm [19–22]. It is desirable to reduce the size of Cu NPs to achieve efficient catalytic functions.

Here, I propose high-pressure and high-temperature (HPHT) synthesis to make metal nanoparticles supported on MOF-derived carbonaceous materials. In general, diffusion in the solid state is expected to be affected by applied pressure. Indeed, in the case of diffusion by vacancy mechanism, it has been reported that the diffusion coefficient decreases with a rise in pressure theoretically and experimentally [23–26]. Thus, it is expected that pyrolysis under high pressure can prevent nanoparticles from aggregating if their atoms diffused by the vacancy mechanism is dominant.

In this work, I carried out the HPHT treatment of copper benzenetricarboxylate (Cu–BTC; $C_{18}H_6Cu_3O_{12}$) [27,28] to examine the possibility of controlling the carbonization process. The products were characterized by transmission electron microscopy (TEM), X-ray diffraction (XRD), Fourier-transform infrared spectroscopy (FTIR), and X-ray absorption spectroscopy (XAS). I also prepared the samples treated under a vacuum-sealed glass tube for comparison. I found that the precursor Cu-BTC was converted to a copper–carbon composite (Cu@C) at a relatively low temperature and the samples

pyrolyzed sufficiently by the HPHT method contained fine Cu nanoparticles. Finally, I investigated the catalytic activity of the HPHT-treated samples in azide–alkyne Huisgen cycloaddition [5,29–32].

3.2 Experimental section

3.2.1 Sample preparation

Cu-BTC, whose trade name is Basolite® C-300, was purchased from Aldrich. Benzylazide, phenylacetylene, 1,4-dioxane, triethylamine, 1,3,5-triisopropylbenzene, and Cu standard solution (1000 ppm aqueous solution) were purchased from FUJIFILM Wako Pure Chemical and were used without further purification.

High-pressure experiments were carried out using a cubic anvil press (180 ton, CTfactory) calibrated with phase transitions of bismuth [33]. The Cu-BTC powder was encapsulated in a cylindrical copper capsule, which was embedded in a NaCl filler and then a graphite tube heater, which was then placed in a 13 mm pyrophyllite cube with stainless steel electrodes. I confirmed that the copper capsule was stable and did not interfere with the results. The temperature was measured by an alumel–chromel thermocouple placed in the pyrophyllite cube, which was calibrated with another thermocouple at the sample position in a separate measurement. The sample assembly was compressed to 5 GPa. Then the cell assembly was heated by flowing electric

current to the graphite heater in the sample assembly. The temperature increase took approximately 15 min, and the temperature was kept at 200, 300, 400, and 500 ◦C for 15 min. Then the heating was stopped by switching off the current, and the temperature became below 50 ◦C only after 30 s. After the sample was completely cooled down, the pressure was released, and the samples were collected from the cubic anvil press under ambient conditions. After ground by a mortar and pestle, the obtained samples were used for characterization and catalytic reaction.

I also synthesized the samples pyrolyzed under a vacuum. A Cu-BTC pellet was placed in a glass tube with one side closed, and a vacuum pump evacuated the glass tube to 6.0 × 10−1 Pa. Subsequently, the glass tube was sealed under vacuum by burning off a part of the glass tube with a burner. The Cu-BTC samples sealed in the glass tube were heated in a furnace at different temperatures (i.e., 200, 300, and 400 ◦C). The temperature was held for 15 minutes, and then the glass tube was removed from the furnace. After the samples cooled to room temperature, the sample was collected from the glass tube. The obtained samples were ground into powder by a mortar and pestle and were used for further experiments.

3.2.2 Characterization

Scanning electron microscopy (SEM) observations were conducted by a JEM-2010 (JEOL). The carbonized products were analyzed by powder XRD (MiniFlex 600,

Rigaku), FT-IR (FTIR-4600, JASCO), and TEM (JEM-2010, JEOL). Adsorption–desorption isotherms of N_2 at 77 K were acquired on a Belsorp-mini instrument (BEL Japan Inc.). Specific surface areas were estimated by using the Brunauer-Emmett-Teller (BET) equation applied to the adsorption isotherms of N_2. XAS spectra were taken at BL11S2 of Aichi Synchrotron Radiation Center in transmission mode. The sample and hexagonal boron nitride used as a matrix were mixed with a mortar and pestle for 20 min, and the mixture was pelletized into a 10 mm pellet using a tablet press for XAS measurement.

Copper contents in the samples were determined by inductively coupled plasma optical emission spectroscopy (ICP-OES). The samples were completely dissolved in concentrated nitric acid under reflux conditions, and the diluted sample solutions were used for ICP-OES (ICPE-9000, Shimadzu) measurement. The detail described below. Cu standard solution (Cu 1000 ppm, solvent 0.1 mol/L HNO_3) was diluted with 1.3 mol/L HNO_3 to prepare Cu standard samples for making a calibration curve at concentrations of 10 ppm, 5 ppm, 2.5 ppm, 1.25 ppm, and 500 ppb. Sample solutions to measure Cu content were prepared as follows: the sample powder was added to a flask with 13 mol/L (60 wt%) HNO_3 10 mL, then the dispersion was heated until all of the powder was dissolved with refluxing. The solutions were diluted with distilled water to make the HNO_3 concentration 1.3 mol/L. These original solutions were further diluted

with 1.3 mol/L HNO_3 to prepare two sample solutions with different concentrations for one sample.

3.2.3 Catalytic activity test

The catalytic performance of these samples was evaluated for Huisgen cycloaddition illustrated in Scheme 3-1 following the procedure in the literature [30]. A powder catalyst (10 mg) prepared as stated above was added to the mixture of benzylazide (0.20 mmol), phenylacetylene (0.22 mmol), triethylamine (0.22 mmol), and 1,4-dioxane (4 mL) in a test tube. Subsequently, a stir bar was added to the test tube, and the tube was sealed by a cap. The reaction solution was heated with stirring at 60 ◦C for 1 h. Then cycloaddition was quenched by an ice bath. After the catalyst powder was removed from the mixture by filtration, the filtrate was analyzed by gas chromatography (GC) to determine the yield of the cycloaddition product. A gas chromatograph (GC-14B, Shimadzu) was equipped with a flame ionization detector and capillary column (TC-FFAP, 0.25 mm, 50 m). 1,3,5-Triisopropylbenzene was used as an internal standard. To assign the GC peaks, the filtrate was analyzed with a GC–mass spectrometer (GCMS-QP2010SE, Shimadzu) equipped with a capillary column (SH-Rxi-5Sil MS, Shimadzu).

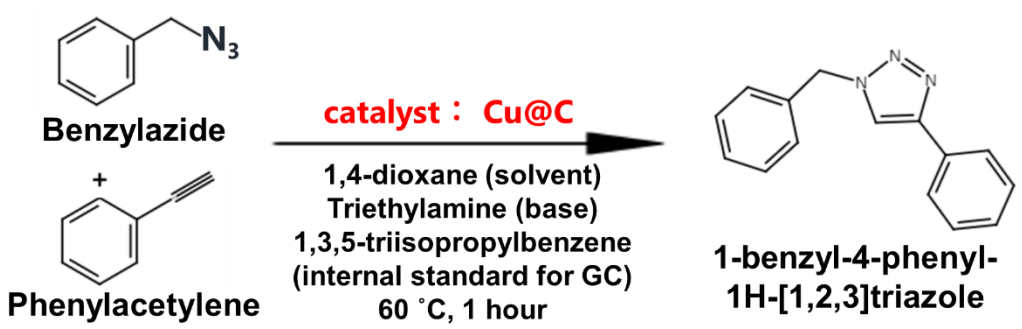

Scheme 3-1 Huisgen cycloaddition for the evaluation of catalytic performance.

3.3 Results and Discussion

The powder XRD patterns and FTIR spectra were acquired to characterize and identify the as-synthesized samples. Figure 3-1(a) and (b) shows the XRD patterns of the MOF-derived samples prepared by the HPHT treatment and pyrolysis in a vacuum-sealed glass tube, respectively. The figure also illustrates that of the precursor Cu-BTC for comparison. As shown in Figure 3-1(a), the three characteristic peaks at 2θ = 43.4°, 50.5°, and 74.1° are observed in all HPHT-treated samples, which are absent in the precursor Cu-BTC. These diffraction peaks correspond to (110), (200), and (220) crystalline planes of metallic copper, respectively. No peaks attributed to CuO and Cu_2O were observed. It is reported that the framework structure of Cu-BTC is robust at room temperature and does not become amorphous below 20 GPa [34]. The appearance of diffraction peaks from Cu indicates that the pyrolysis of Cu-BTC at 5 GPa started at 200 °C or below, resulting in the formation of metallic copper and carbonized BTC framework. Besides, some peaks of the precursor Cu-BTC were maintained in the low-

angle region at 5 GPa/200 °C and 5 GPa/300 °C. This suggests that the partly collapsed Cu-BTC framework may remain in these samples.

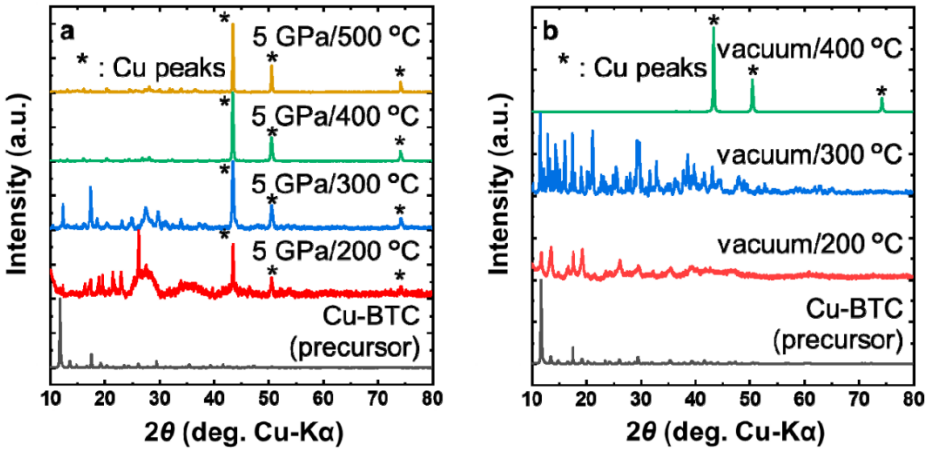

Figure 3-1 X-ray diffraction patterns of (a) the HPHT samples and (b) the samples pyrolyzed in the vacuum-sealed glass tubes. The peaks marked with an asterisk (*) at 2θ = 43.4°, 50.5°, and 74.1° are assigned to (110), (200), and (220) crystalline planes of metallic Cu, respectively.

On the other hand, the XRD patterns of the samples obtained in the vacuum-sealed glass tube show a different trend from those of the HPHT-treated ones (Figure 3-1(b)). For the samples obtained at 200 and 300 °C, the peaks due to not metallic Cu but the partially decomposed precursor Cu-BTC were observed. The peaks became broader, and the intensities significantly changed with temperature increase, indicating that heat treatments decreased the crystallinity with no production of Cu particles. For the sample obtained at 400 °C, three diffraction peaks of metallic Cu were observed as in the case of HPHT-treated samples. Therefore, it is apparent that the Cu-BTC pyrolyzed and

carbonized at 400 °C in the vacuum-sealed glass tube. The XRD measurements indicate that pyrolysis initiation temperature declined in HPHT experiments. The results suggest that the pyrolysis of Cu-BTC was accelerated by compression. This is because this reaction is probably accompanied by a volume reduction.

Figure 3-2 (a) and (b) show the IR spectra of the HPHT-treated samples and those heated in a vacuum-sealed glass tube, respectively. The IR spectrum of the precursor Cu-BTC is given for comparison. Several characteristic bands are observed in the spectrum of the precursor Cu-BTC. The band at 486 cm^{-1} corresponds to the Cu–O stretching vibration. The two bands at 730 and 760 cm^{-1} correspond to the out-of-plane C–H bending vibration of the benzene rings of the Cu-BTC, while the band at 1110 cm^{-1} corresponds to their in-plane C–H bending vibration. The two bands at 1373/1449 cm^{-1} and 1571/1630 cm^{-1} represent the symmetric and asymmetric stretching vibration of the carboxylate groups, respectively [34]. For the spectra of all the HPHT-treated samples, the Cu–O band disappears as shown in Figure 3-2(a), which means that Cu^{2+} no longer coordinated with carboxyl groups COO^{-} and the crystal structure of Cu-BTC was collapsed. The bands corresponding to the benzene rings and carboxylate groups gradually disappeared as the temperature was increased. This indicates that the pyrolysis of the BTC (i.e., $C_6H_3(COO^{-})_3$) proceeded at temperatures higher than that for metallic Cu formation. It is considered that the benzene ring decomposed to carbonaceous

substances, and COO^- was eliminated as CO_2. This decarboxylation was associated with the reduction of Cu^{2+} to metallic Cu. This is consistent with the results of XRD. Besides, the IR spectra indicate that a small amount of benzene ring and carboxy groups remained in the samples treated at 400 and 500 °C under 5 GPa, although their XRD patterns exhibited only metallic Cu peaks. It means that the carbonized matrix was amorphous.

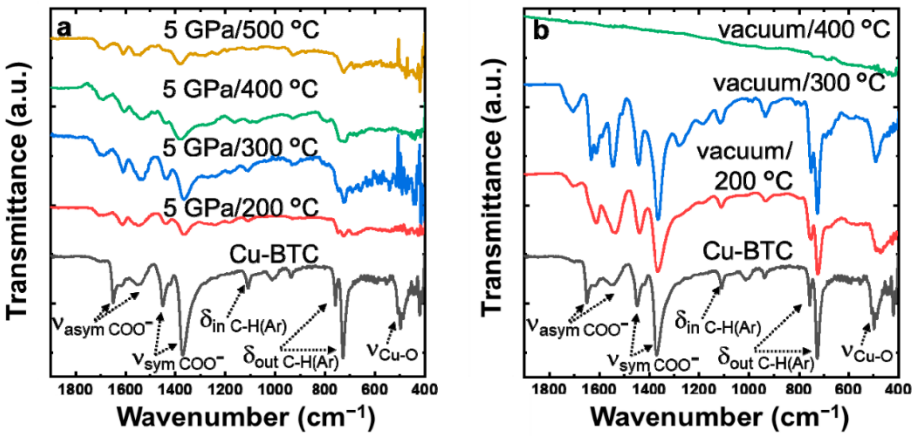

Figure 3-2 FTIR spectra of (a) the HPHT samples and (b) the samples pyrolyzed in the vacuum-sealed glass tubes. Marks of IR peaks ν, δ, and Ar in the figures denote stretching, bending, and the benzene ring, respectively.

The samples heated at 200 and 300 °C in the vacuum-sealed glass tube had IR bands similar to those of the precursor Cu-BTC, while no such bands were observed in the sample obtained at 400 °C. This result indicates that the Cu-BTC was not pyrolyzed at 300 °C or below, while the benzene ring was fully converted to carbon materials by

pyrolysis at 400 °C. This is also consistent with the result of XRD.

The copper content of the synthesized samples was examined by ICP-OES. As shown in Table 3-1, the relative Cu content increased with an increase in the treatment temperature for the HPHT-treated samples. It reflects the progress of pyrolysis associated with the loss of carbon species, which is consistent with the results of XRD and FTIR. The Cu contents of 5 GPa/200 °C and 5 GPa/300 °C samples were lower than that of the precursor Cu-BTC (31.5 wt%), and this may be caused by moisture absorption on the samples. On the other hand, for the samples obtained in the vacuum-sealed glass tube, the Cu content of the unpyrolyzed ones (<300 °C) was almost the same as that of the Cu-BTC. Subsequently, the Cu content was increased drastically by heating at 400 °C, indicating the occurrence of the pyrolysis.

Table 3-1 Cu content determined by ICP-OES of MOF-derived Cu@C materials.

Scheme	Cu content
5 GPa/500 ˚C	63 wt%
5 GPa/400 ˚C	56 wt%
5 GPa/300 ˚C	27 wt%
5 GPa/200 ˚C	25 wt%
Vacuum/400 ˚C	54 wt%
Vacuum/300 ˚C	30 wt%
Vacuum/200 ˚C	30 wt%

Previous studies have reported that Cu-BTC decomposes at >400 °C under ambient pressure [35–38]. Our experiments show that heating of Cu-BTC in vacuum had the same trend. However, under high pressure (5 GPa), Cu-BTC started to decompose and produce metallic copper at a lower temperature than those conditions. This suggests that the high pressure shifts the equilibrium to the side to decompose Cu-BTC to produce Cu.

The morphology of Cu particles in the samples was examined by TEM. While the pristine Cu-BTC formed the microcrystals (Figure 3-3), the samples sufficiently pyrolyzed contained Cu as NPs in the carbon matrix, as shown in Figure 3-4. For the samples synthesized at 5 GPa/500 °C and 5 GPa/400 °C, the sizes of Cu NPs are around 5 and 10 nm, respectively, which are smaller than that pyrolyzed in a vacuum-sealed glass tube. Furthermore, the Cu NPs are also smaller than the values of the reported Cu-BTC-derived materials pyrolyzed at ambient pressure [35–37]. Therefore, high-pressure treatments enable the Cu NPs to prevent from sintering without any special templates or support materials. This pressure effect can be originated from the pressure dependency of the diffusion coefficient.

Although the fine particles were observed in TEM images of the HPHT-treated samples, the XRD patterns had sharp diffraction peaks indicating large grain size. The fact that the particle sizes were not uniform in TEM images can explain this phenomenon. In other words, particle size refinement by high pressure occurs as a

general trend, and particle sizes have a distribution. The large particles among them can give sharp peaks in the XRD. It is assumed that the particle size distribution is related to the grain size of Cu-BTC before treatments.

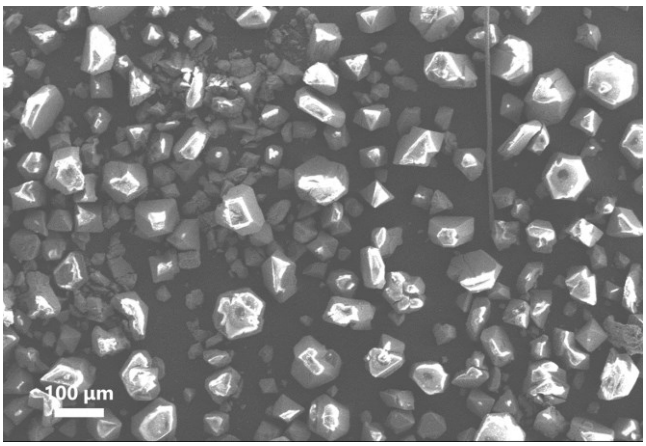

Figure 3-3 SEM image of pristine Cu-BTC crystals.

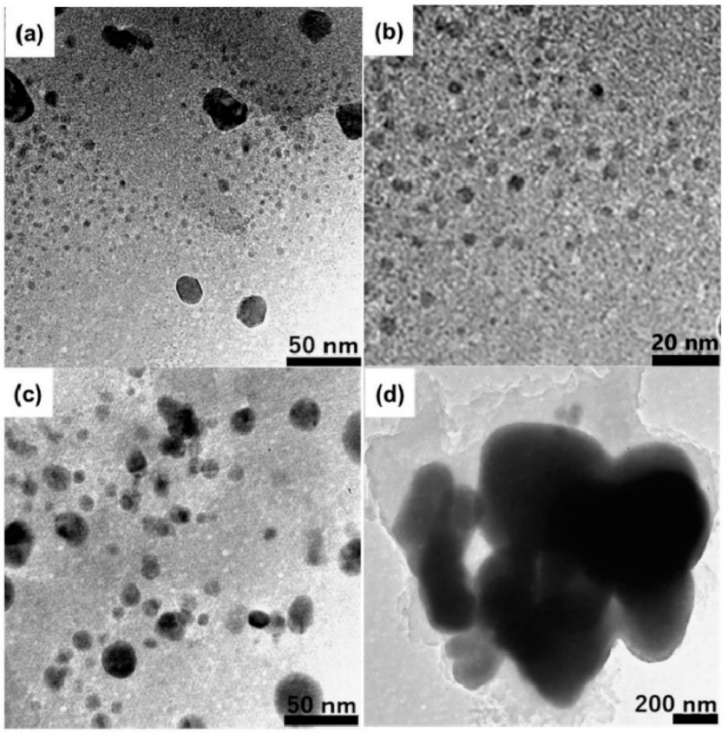

Figure 3-4 TEM images of (a) Cu@C synthesized at 5 GPa/500 °C, (b) magnified view of (a), (c) Cu@C synthesized at 5 GPa/400 °C, and (d) Cu@C synthesized in a vacuum-sealed glass tube (vacuum/400 °C).

The samples pyrolyzed sufficiently were further characterized by X-ray absorption

near edge structure (XANES) in order to evaluate the valence state of Cu in the NPs. The normalized XANES spectra of these samples and references (Cu-foil, Cu_2O, and CuO) are shown in Figure 3-5. The sample synthesized in the vacuum-sealed glass tube at 400 °C showed a similar XANES spectrum to that of the Cu-foil in the spectrum, whereas the samples prepared at 5 GPa/400 °C and 5 GPa/500 °C were quite different from those of the references. The main absorption peak of the sample prepared at 5 GPa slightly shifted toward higher energy, and the slope on the rising of the peak became smaller than that of the Cu-foil. It is in contrast to the fact that only metal Cu peaks were observed in the XRD patterns of all these samples. This indicates that the spectra of the HPHT-treated samples contained the component for those of Cu_2O and CuO. Thus, it is revealed that the surface of Cu NPs in HPHT-treated samples was partially oxidized. The XANES spectra were curve-fitted by linear combination of the spectra of the Cu-foil, Cu_2O, and CuO. The result is shown in Table 3-2 and Figure 3-6.

Table 3-2 XANES analysis for Cu valency of MOF-derived Cu@C materials.

Synthesis Conditions	Cu	Cu_2O	CuO
	Atomic %	Atomic %	Atomic %
5 GPa/500 °C	26.2 ± 1.9	22.6 ± 2.3	51.2 ± 4.5
5 GPa/400 °C	44.9 ± 4.8	31.9 ± 5.7	26.2 ± 8.3
vacuum/500 °C	79.3 ± 1.4	20.7 ± 3.0	0.0 ± 09

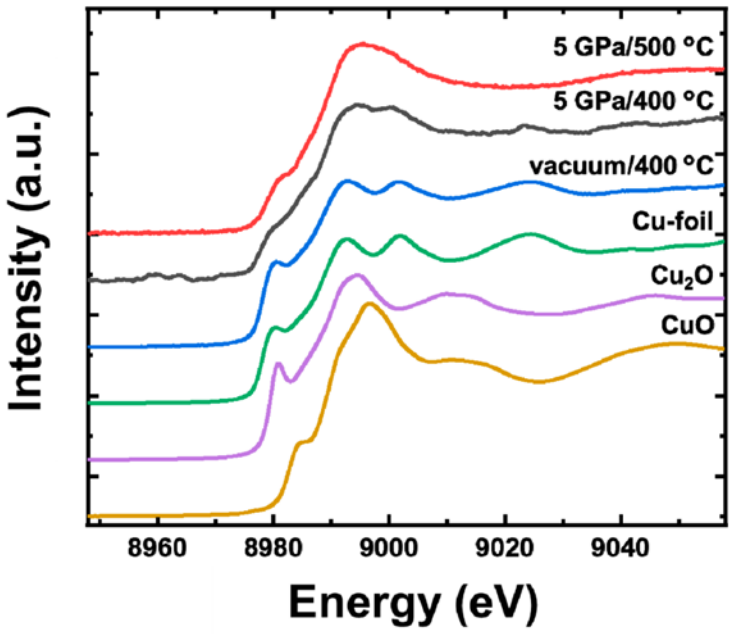

Figure 3-5 XANES spectra of MOF-derived Cu@C and reference samples.

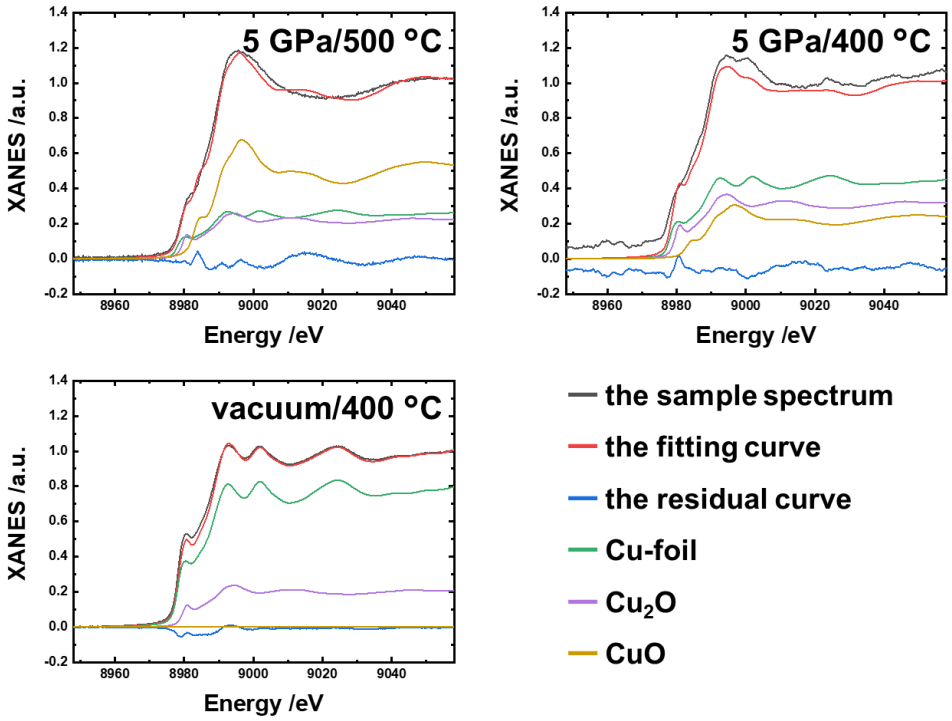

Figure 3-6 Curve fitting of the XANES spectra was least square of the residuals using spectra of Cu foil, Cu_2O and CuO.

The fitting results revealed that the sample prepared at 5 GPa/500 °C was the most oxidized, and the one prepared at 5 GPa/400 °C was the second most done. The sample prepared at vacuum/400 °C was the least oxidized. This indicates that the Cu NPs produced by the HPHT treatment are oxidized. It is considered that the air has oxidized the nanoparticles during or after the treatments. In addition, no diffraction peaks of copper oxide were observed in XRD, suggesting that the oxides are amorphous.

The porous nature of the carbonaceous matrix in these samples was characterized by N_2 adsorption measurements, with the specific surface areas (SSAs) calculated by the BET method. The results are shown in Table 3-3. Only the one synthesized at 200 °C had mesopores as in the precursor Cu-BTC, while the other ones showed macropores. The rather complicated behavior of the SSAs shown in Table 3-3 can be explained as follows. In the vacuum-treated samples, the SSAs decreased significantly by the deterioration in crystallinity at 200 and 300 °C. At 400 °C, the pyrolysis proceeded, and CO_2 and other volatile species were formed, resulting in channels in the products and in an increase in the SSAs. In the HPHT-treated samples, very small SSAs at 200 °C can be explained by the collapse of the pores of a MOF by decomposition under pressure. The increase of SSAs from 300 to 400 °C can be explained by the pores created by trails of Cu NPs during the aggregation. At 500 °C, the Cu aggregation is hindered by the quick carbonization of the MOF ligand, thus preventing the formation of long connected

channels.

Huisgen cycloaddition is one of the most representative click reactions that produce 1,2,3-triazole and is accelerated by Cu catalysts [18,30]. The yields of the product in Huisgen cycloaddition are shown in Table 3-4.

Table 3-3 Surface areas measured by N_2 adsorption and the BET method of MOF-derived Cu@C materials, pristine Cu-BTC.

Synthesis conditions of catalysts	Surface areas/m^2g^{-1}
5 GPa/500 ˚C	6.7
5 GPa/400 ˚C	22.6
5 GPa/300 ˚C	9.1
5 GPa/200 ˚C	0.40
Vacuum/400 ˚C	13.6
Vacuum/300 ˚C	9.7
Vacuum/200 ˚C	124.6
Cu-BTC	937.6

Table 3-4 Yields of the product in Huisgen cycloaddition over by MOF-derived Cu@C catalysts.

Synthesis conditions of catalysts	Yield
5 GPa/500 ˚C	28 %
5 GPa/400 ˚C	18 %
5 GPa/300 ˚C	16 %
5 GPa/200 ˚C	0 %
Blank (no catalyst)	0 %

The HPHT pyrolyzed samples exhibited catalytic activity, which was improved with

a rise in treatment temperature. On the other hand, vacuum-pyrolyzed samples did not show catalytic activity. I can consider three factors governing the catalytic activity in this case. The first is the exposure of the Cu NP surface to the outside. If the carbon species cover the Cu NPs, the Cu NPs do not work as catalysts. Under a confined environment, the decomposed species may cover the surface of the Cu NPs. This explains the result in which the samples obtained in the vacuum-sealed glass tube did not show catalytic activity. In contrast, the HPHT environment was in the air, and carbonaceous matrix species covering the Cu NP can be partially combusted. Actually, I can see some small gaps between the Cu NPs and the surrounding matrix in the TEM images of the HPHT-treated samples (Figure 3-4 (a)–(c)), whereas the samples treated in the vacuum-sealed glass tube were totally covered by carbon matrix (Figure 3-4(d)).

The second factor is the surface-to-volume ratio of the Cu NPs. In general, Cu NPs easily sinter and aggregate at >300 °C, leading to a decrease in catalytic activity. In this work, however, I succeeded in inhibiting the diffusion of Cu atoms by treating them under high pressure, thus preventing the aggregation. This effect makes it possible to increase the relative copper loading ratio contained in the samples without sintering the particles, which I consider to be responsible for the increase in the catalytic activity of the HPHT samples treated at higher temperatures.

The third factor is the oxidation state of the NP surface. It has been reported that not

only CuI salts but also mixed Cu/Cu–oxide NPs or CuO can act as catalysts [1,5,30,39]. The XANES results showed that the surfaces of the Cu NPs in the samples synthesized at 5 GPa/400 °C and 5 GPa/500 °C were partly oxidized, forming mixed Cu/Cu–oxide NPs. The 5 GPa/500 °C sample was more oxidized. These results are in accordance with the catalytic activity. The high oxidation ratio of the HPHT 500 °C sample is explained by the high surface-to-volume ratio of the smallest Cu NPs among the samples.

The second and third factors come from the small size of the Cu NPs, which originated from the inhibited diffusion of Cu atoms at a high-pressure condition during the decomposition of the MOF. The present result offers a strategy for the preparation of highly active catalysts based on metal nanoparticles synthesized from the decomposition of the MOF and metal complex-based materials.

3.4 Conclusion

I examined the HPHT treatment of the Cu-containing MOF (Cu-BTC) to prepare Cu NPs supported on the carbonaceous material. The aggregation of Cu NPs was prevented, and sub-10 nm NPs were obtained. It was found that the decomposition temperature of Cu-BTC was lowered from 400 °C at ambient pressure or vacuum to 200 °C at 5 GPa. The Cu@C samples prepared by the HPHT treatment showed high activity for Huisgen cycloaddition reaction.

References

[1] J. Hassan, M. Sévignon, C. Gozzi, E. Schulz, and M. Lemaire, *Aryl−Aryl Bond Formation One Century after the Discovery of the Ullmann Reaction*, Chem. Rev. **102**, 1359 (2002).

[2] M. B. Thathagar, J. Beckers, and G. Rothenberg, *Copper-Catalyzed Suzuki Cross-Coupling Using Mixed Nanocluster Catalysts*, J. Am. Chem. Soc. **124**, 11858 (2002).

[3] M. B. Thathagar, J. Beckers, and G. Rothenberg, *Palladium-Free and Ligand-Free Sonogashira Cross-Coupling*, Green Chem. **6**, 215 (2004).

[4] M. Lakshmi Kantam, V. Swarna Jaya, M. Jaya Lakshmi, B. R. Reddy, B. M. Choudary, and S. K. Bhargava, *Alumina Supported Copper Nanoparticles for Aziridination and Cyclopropanation Reactions*, Catal. Commun. **8**, 1963 (2007).

[5] F. Alonso, Y. Moglie, G. Radivoy, and M. Yus, *Multicomponent Synthesis of 1,2,3-Triazoles in Water Catalyzed by Copper Nanoparticles on Activated Carbon*, Adv. Synth. Catal. **352**, 3208 (2010).

[6] M. Kidwai, N. K. Mishra, V. Bansal, A. Kumar, and S. Mozumdar, *Cu-Nanoparticle Catalyzed O-Arylation of Phenols with Aryl Halides via Ullmann Coupling*, Tetrahedron Lett. **48**, 8883 (2007).

[7] S. Bhadra, A. Saha, and B. C. Ranu, *One-Pot Copper Nanoparticle -Catalyzed Synthesis of S-Aryl- and S-Vinyl Dithiocarbamates in Water : High Diastereoselectivity Achieved for Vinyl Dithiocarbamates*, Green Chem. **10**, 1224 (2008).

[8] M. Kidwai, V. Bansal, A. Saxena, S. Aerry, and S. Mozumdar, *Cu-Nanoparticles: Efficient Catalysts for the Oxidative Cyclization of Schiffs' Bases*, Tetrahedron Lett. **47**, 8049 (2006).

[9] X. Li et al., *Large-Area Synthesis of High-Quality and Uniform Graphene Films on Copper Foils*, Science **324**, 1312 (2009).

[10] Z. Sun, Z. Yan, J. Yao, E. Beitler, Y. Zhu, and J. M. Tour, *Growth of Graphene from Solid Carbon Sources*, Nature **468**, 7323 (2010).

[11] Q. Lu, J. Rosen, Y. Zhou, G. S. Hutchings, Y. C. Kimmel, J. G. Chen, and F. Jiao, *A Selective and Efficient Electrocatalyst for Carbon Dioxide Reduction*, Nat. Commun. **5**, 1 (2014).

[12] R. Kortlever, J. Shen, K. J. P. Schouten, F. Calle-Vallejo, and M. T. M. Koper, *Catalysts and Reaction Pathways for the Electrochemical Reduction of Carbon Dioxide*, J. Phys. Chem. Lett. **6**, 4073 (2015).

[13] M. Iwamoto and H. Hamada, *Removal of Nitrogen Monoxide from Exhaust Gases through Novel Catalytic Processes*, Catal. Today **10**, 57 (1991).

[14] J. Kašpar, P. Fornasiero, and N. Hickey, *Automotive Catalytic Converters: Current Status and Some Perspectives*, Catal. Today **77**, 419 (2003).

[15] J. McNulty, K. Keskar, and R. Vemula, *The First Well-Defined Silver(I)-Complex-Catalyzed Cycloaddition of Azides onto Terminal Alkynes at Room Temperature*, Chem. Eur. J. **17**, 14727 (2011).

[16] D. Astruc, F. Lu, and J. R. Aranzaes, *Nanoparticles as Recyclable Catalysts: The Frontier between Homogeneous and Heterogeneous Catalysis*, Angew. Chem. Int. Ed. **44**, 7852 (2005).

[17] M. T. Reetz and M. Maase, *Redox-Controlled Size-Selective Fabrication of Nanostructured Transition Metal Colloids*, Adv. Mater. **11**, 773 (1999).

[18] B. C. Ranu, R. Dey, T. Chatterjee, and S. Ahammed, *Copper Nanoparticle-Catalyzed Carbon-Carbon and Carbon-Heteroatom Bond Formation with a Greener Perspective*, ChemSusChem **5**, 22 (2012).

[19] K. Shen, X. Chen, J. Chen, and Y. Li, *Development of MOF-Derived Carbon-Based Nanomaterials for Efficient Catalysis*, ACS Catal. **6**, 5887 (2016).

[20] A. Kim, N. Muthuchamy, C. Yoon, S. Joo, and K. Park, *MOF-Derived Cu@Cu_2O Nanocatalyst for Oxygen Reduction Reaction and Cycloaddition Reaction*, Nanomaterials **8**, 138 (2018).

[21] A. Han et al., *Recent Advances for MOF-Derived Carbon-Supported Single-Atom Catalysts*, Small Methods **3**, 1800471 (2019).

[22] H. Liu, S. Zhang, Y. Liu, Z. Yang, X. Feng, X. Lu, and F. Huo, *Well-Dispersed and Size-Controlled Supported Metal Oxide Nanoparticles Derived from MOF Composites and Further Application in Catalysis*, Small **11**, 3130 (2015).

[23] C. T. Candland, D. L. Decker, and H. B. Vanfleet, *Interstitial Diffusion of Copper in Lead at Pressures up to 56 Kbar*, Phys. Rev. B **5**, 2085 (1972).

[24] N. L. Peterson, *Self-Diffusion in Pure Metals*, J. Nucl. Mater. **69–70**, 3 (1978).

[25] J. Wang, B. Chen, Q. Williams, and M. H. Manghnani, *Short- and Intermediate-Range Structure and Dynamics of Fe-Ni-C Liquid Under Compression*, Front. Earth Sci. **7**, (2019).

[26] G. Rein and H. Mehrer, *Effect of Hydrostatic Pressure and Temperature on the Self-Diffusion Rate in Single Crystals of Silver and Gold*, Philos. Mag. A **45**, 467 (1982).

[27] S. S.-Y. Chui, S. M.-F. Lo, J. P. H. Charmant, A. G. Orpen, and I. D. Williams, *A Chemically Functionalizable Nanoporous Material [$Cu_3(TMA)_2(H_2O)_3]_n$*, Science **283**, 1148 (1999).

[28] H.-Y. Chen, G. Wee, R. Al-Oweini, J. Friedl, K. S. Tan, Y. Wang, C. L. Wong, U. Kortz, U. Stimming, and M. Srinivasan, *A Polyoxovanadate as an Advanced Electrode Material for Supercapacitors*, ChemPhysChem **15**, 2162 (2014).

[29] G. Molteni, C. L. Bianchi, G. Marinoni, N. Santo, and A. Ponti, *Cu/Cu-Oxide Nanoparticles as Catalyst in the "Click" Azide – Alkyne Cycloaddition*, New J. Chem. **30**, 1137 (2006).

[30] B. H. Lipshutz and B. R. Taft, *Heterogeneous Copper-in-Charcoal-Catalyzed Click Chemistry*, Angew. Chem. Int. Ed. **45**, 8235 (2006).

[31] X. Zhang, H. Li, L. You, Y. Tang, and R. P. Hsung, *Copper Salt-Catalyzed Azide-[3 + 2] Cycloadditions of Ynamides and Bis-Ynamides*, Adv. Synth. Catal. **348**, 2437 (2006).

[32] Z.-Y. Yan, Y.-B. Zhao, M.-J. Fan, W.-M. Liu, and Y.-M. Liang, *General Synthesis of (1-Substituted-1H-1,2,3-Triazol-4-Ylmethyl)-Dialkylamines via a Copper(I)-Catalyzed Three-*

Component Reaction in Water, Tetrahedron **61**, 9331 (2005).

[33] J. S. Knibbe, S. M. Luginbühl, R. Stoevelaar, W. van der Plas, D. M. van Harlingen, N. Rai, E. S. Steenstra, R. van de Geer, and W. van Westrenen, *Calibration of a Multi-Anvil High-Pressure Apparatus to Simulate Planetary Interior Conditions*, EPJ Techn. Instrum. **5**, 5 (2018).

[34] Z. Dong, Z. Mi, W. Shi, H. Jiang, Y. Zheng, and K. Yang, *High Pressure Effects on Hydrate Cu-BTC Investigated by Vibrational Spectroscopy and Synchrotron X-Ray Diffraction*, RSC Adv. **7**, 55504 (2017).

[35] J. Zhang, B. An, Y. Hong, Y. Meng, X. Hu, C. Wang, J. Lin, W. Lin, and Y. Wang, *Pyrolysis of Metal–Organic Frameworks to Hierarchical Porous Cu/Zn-Nanoparticle@carbon Materials for Efficient CO_2 Hydrogenation*, Mater. Chem. Front. **1**, 2405 (2017).

[36] J. Cheng, X. Xuan, X. Yang, J. Zhou, and K. Cen, *Selective Reduction of CO_2 to Alcohol Products on Octahedral Catalyst of Carbonized Cu(BTC) Doped with Pd Nanoparticles in a Photoelectrochemical Cell*, Chem. Eng. J. **358**, 860 (2019).

[37] Y. Weng, S. Guan, L. Wang, H. Lu, X. Meng, G. I. N. Waterhouse, and S. Zhou, *Defective Porous Carbon Polyhedra Decorated with Copper Nanoparticles for Enhanced NIR-Driven Photothermal Cancer Therapy*, Small **16**, 1905184 (2020).

[38] X. Zhou, X. Zhai, G. Ge, J. Dan, K. Pan, J. Tian, R. Sun, B. Dai, H. Pfeiffer, and F. Yu, *Enhanced Selective Catalytic Reduction of NO with CO over Cu/C Nanoparticles Synthetized from a Cu-Benzene-1,3,5-Tricarboxylate Metal Organic Framework by a Continuous Spray Drying Process*, Chem. Eng. J. **388**, 124270 (2020).

[39] V. D. Bock, H. Hiemstra, and J. H. van Maarseveen, *CuI-Catalyzed Alkyne–Azide "Click" Cycloadditions from a Mechanistic and Synthetic Perspective*, Eur. J. Org. Chem. **2006**, 51 (2006).

Chapter 4 Ultrahigh pressure-induced modification of morphology and performance of MOFs-derived Cu@C electrocatalysts.

4.1 Introduction

The development of high-performance catalysts has currently been paid attention to deal with environmental issues and promote clean and sustainable energy production [1–3]. Although noble metals, such as Pt, Pd, and Rh, are mainly used as catalysts, their widespread use is prevented by their low earth abundance and high prices [4–6]. In particular, electrocatalysts for the oxygen reduction reactions(ORR) and oxygen evolution reaction (OER) will significantly increase in demand because they play an important role in clean energy technologies, i.e., water splitting [7,8], fuel cells [9,10], and metal-air batteries [11]. Therefore, high-performance materials as alternatives to noble metals are strongly desired and have been studied. [12–14] There are two approaches to develop them. One is the search for novel compounds with previously unknown compositions, such as new transition metals oxynitrides [15–17], Heusler alloys [18,19], and MXenes [20]. The other one is controlling the nanostructures of materials to improve the catalytic efficiency. What is expected from this approach includes making their active sites more dispersed [21], modifying their

electronic structure [22–24], and stabilizing specific atomic arrangements on the nanosurfaces [25–27]. Appropriately predesigned precursors are needed in this approach. An example of the former approach includes high-pressure synthesis. High-pressure synthesis has been used to search for novel materials because this method can provide compounds difficult to synthesize under ambient conditions [28–30]. Previous studies regarding the high-pressure synthesis of the electrocatalysts were limited, which include quadruple perovskites [31,32], transition metal carbides [33], phosphides [34], and borides [35]. However, no studies of the latter approach - controlling the nanostructures of the electrocatalysts - have utilized high-pressure synthesis before the present authors.

I have employed metal-organic frameworks (MOFs) for controlling the nanostructures by high-pressure and high-temperature (HPHT) treatments. [36] The MOFs consists of metal cations and organic ligands, and carbon-supported heterogeneous catalysts can be synthesized in one step by pyrolysis [37–39]. However, this approach often suffers from the aggregation of the catalyst particles during the pyrolysis. Metals that are not alloyed with carbon, ex. Cu, strongly indicate this tendency [38,40]. Although using designed precursors may solve this problem [41–48], this method also has challenges. First, designing and synthesizing precursors require complicated procedures. Second, available metal elements are limited because precursor

MOFs suitable for this method are restricted [21]. I focus on the HPHT treatments of the MOFs as a new method to control the nanostructures.

Generally, the lattice diffusion of atoms is inhibited under high pressure due to increase in the activation energy of the diffusion [49–52]. This feature suppresses the agglomeration of metal atoms in the thermal treatments during the synthesis of the catalysts. Therefore, the HPHT treatment of the MOFs will lead to the miniaturization of nanoparticles in the MOFs-derived heterogeneous catalysts. I have already succeeded in the preparation of single-nm copper particles on carbon supports (Cu@C) without nitrogen anchoring simply by the HPHT treatments of copper(ii)-benzene-1,3,5-tricarboxylate (Cu-BTC) at 5 GPa [36]. However, the behavior under lower pressure conditions remains unknown. The electrocatalytic activity has also not been studied.

I now report the morphology of Cu for the Cu@C products synthesized by annealing Cu-BTC at various pressures and their electrocatalytic performance toward oxygen-related reactions in alkaline media. An anomalous pressure dependence was observed, and their performance was superior to previous reports of the MOFs-derived catalysts. The findings will pave the way for the application of high-pressure techniques for controlling the morphology and activity of the nanostructured catalysis.

4.2 Experimental section

4.2.1 Sample preparation

The Cu@C samples were synthesized from Cu-BTC pellets by HPHT treatments under various pressure conditions using a DIA-type cubic-anvil press (CT-factory) or thermal treatment in a vacuum-sealed glass tube. The precursor Cu-BTC was purchased from Sigma Aldrich (its trade name is Basolite® C-300). The applied pressures used in the HPHT treatment were 5, 2.5, 1, and 0.5 GPa, and the heating temperature and time were 500 °C and 15 min, respectively. The cell assembly for the HPHT experiments consisted of a pyrophyllite block with a hole, pyrophyllite disks, a graphite tube coated inside with h-BN, an h-BN pellet, stainless steel rings, and a chromel-alumel thermocouple in an Al_2O_3 tube (Figure 4-1). The sample and h-BN pellet were encapsulated in the graphite tube, then the tube was placed in the hole of the pyrophyllite block. The h-BN pellet was used as a spacer. The hole in the block was closed by fitting the pyrophyllite disks and stainless steel rings. Finally, I drilled a diagonal hole through the block into which I inserted the thermocouple with the Al_2O_3 tube. The hole penetrated the h-BN spacer within the graphite tube to prevent damaging the sample pellets, and the temperature measuring junction was placed at the center of the graphite tube. The sample was heated by flowing an electric current to the graphite heater via the anvils and stainless-steel rings during the HPHT treatments. The heating

started after the cell assembly was pressed to the target pressure. The thermal treatment of a vacuum-sealed Cu-BTC pellet was also conducted at 500 °C for 15 min. Subsequently, the sample was recovered from the glass tube under ambient conditions. After removing the impurity materials due to the cell assembly, each obtained sample was ground using a mortar and pestle, then used for the characterizations and electrochemical measurements.

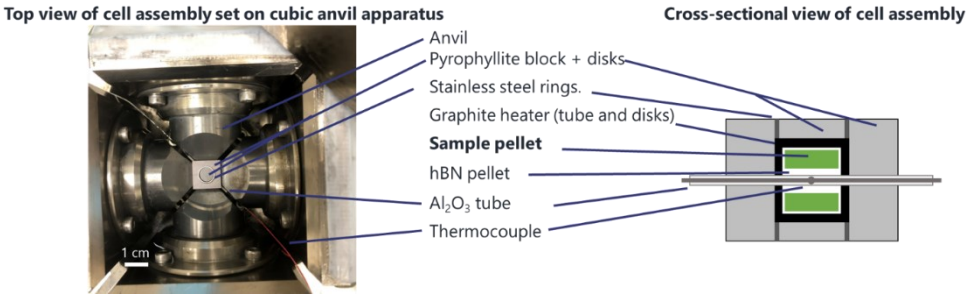

Figure 4-1 The schematic image of the cross-sectional view of the cell assembly for HPHT experiments.

4.2.2 Characterization

Powder X-ray diffraction (XRD) measurements were performed by a MiniFlex-600 (Rigaku, Cu Kα (λ = 1.5405 Å)). Transmission electron microscopy (TEM) observations were conducted by a JEM-2010 (JEOL). High-angle annular dark-field scanning-TEM (HAADF-STEM) observations and TEM electron energy loss spectroscopy (TEM-EELS) measurements were performed using a Titan3 G2 60-300 (FEI). TEM/STEM observations and EDS measurements shown in Figure 4-6- 4-13

were performed by JEM-2100 (JEOL). X-ray photoelectron spectroscopy measurements were performed by JPS-9200 (JEOL, using Mg Kα X-ray).

4.2.3 Electrochemical measurements

All the electrochemical measurements were carried out in a 0.1 M KOH aqueous solution at room temperature using a rotating-disk electrode system (BAS, RRDE-3A) and potentiostat (Hokuto Denko, HSV-110). The working electrode (WE), reference electrode (RE), and counter electrode (CE) in this study were a glassy carbon (GC) rotating-disk electrode (d = 0.4 cm), a Hg/HgO electrode, and a Pt coil electrode, respectively (Figure 4-2).

The catalyst ink was prepared as follows: the sample powder (4 mg) was added to a mixture of a 60 μL Nafion 5 wt% solution (Sigma-Aldrich) and 540 μL of 99.5% ethanol (Japan Alcohol Trading), then the suspension was sonicated for 30 min to yield a uniform ink. The prepared ink (8 μL) was dropped onto a GC disk WE and dried for 30 min. The potentials vs. a reversible hydrogen electrode (RHE) were calculated by the following formula [10]:

$$E_{\mathrm{RHE}} = E_{\mathrm{Hg/HgO}} + 0.098\ \mathrm{V} + 0.0591 \times (\mathrm{pH\ of\ the\ electrolyte}) \quad (1)$$

where E_{RHE} and $E_{\mathrm{Hg/HgO}}$ are the potentials versus RHE and Hg/HgO RE, respectively.

I analyzed the electron transfer number (n) for the ORR from the linear sweep voltammograms measured at various rotating-speeds by the Koutecký-Levich

equation [53]:

$$i^{-1} = i_k^{-1} + i_L^{-1} = i_k^{-1} + 1/(0.620nFcD^{2/3}v^{-1/6}\omega^{1/2}) \quad (2)$$

where I, i_k, i_L, F, c, D, v, and ω are the current density measured at the disk electrode, the kinetic-limited current density, the mass-transfer-limiting current density, Faraday's constant, the oxygen concentration of O_2 in the electrolyte, the diffusion coefficient of the O_2 in the electrolyte, the kinematic viscosity of the electrolyte, and the angular velocity of the disk electrode, respectively.

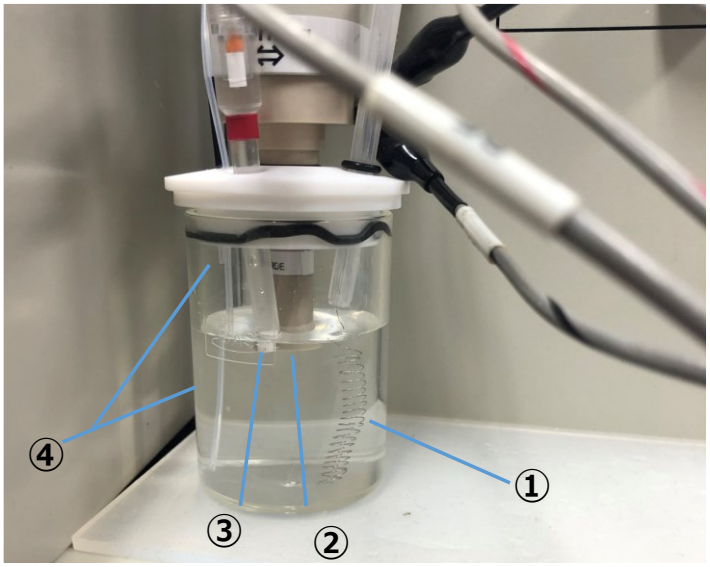

① Counter electrode
② Working electrode
③ Reference electrode
④ Gas tubes

Figure 4-2 The image of the electrochemical measurement system.

4.3 Results and discussion

4.3.1 Sample Preparation

Gas emissions and blowouts to the outside were not observed during the HPHT experiments at 5 GPa, whereas gentle gas emissions to the outside and intense blowouts of the sample cell assembly occurred at 0.5 and 2.5 GPa, respectively. The emissions were observed by temporary drops in the applied loads and sounds. The blowouts destroyed the cell assembly and anvils, which prevented conducting a further analysis at 2.5 GPa. I recovered the sample pellets from the press equipment under ambient conditions after the experiment at 5, 1, and 0.5 GPa. These recovered products from the experiments at 5, 1, and 0.5 GPa were labeled the Cu@C-5GPa, Cu@C-1GPa, and Cu@C-0.5GPa, respectively. I also obtained the products after the thermal treatments in the vacuum-sealed glass and labeled the products Cu@C-vac.

4.3.2 Structural characterization of the samples

I carried out a powder X-ray diffraction (XRD) measurement of the samples recovered after the treatments to identify the decomposition products. Figure 4-3 shows the XRD profiles of the Cu-BTC pyrolyzed under high pressure or in the vacuum-sealed glass tube. All the profiles exhibited obvious diffraction peaks at 43.3°, 50.4°, 74.0°, and 89.8°. These are attributed to the (111), (200), (220), and (311) planes of copper, respectively. This result indicated that most of the Cu^{2+} cations in the Cu-BTC did not

form oxides but were reduced to Cu^0 during the treatments. This reduction reaction is likely to have been caused by decarboxylation of the precursor. Small diffraction peaks due to Cu_2O were also observed at 36.3°, 42.2°, and 63.3° in the patterns of Cu@C-1GPa, Cu@C-0.5GPa, and Cu@C-vac, whereas no Cu_2O peaks were observed in the pattern of Cu@C-5GPa. The relative intensities of the Cu_2O diffraction peaks decreased as the applied pressures increased in the HPHT experiments. This suggested that the precursor was less exposed to the air when it was pyrolyzed at high pressure. However, a characteristic peak around ~26° derived from graphitic carbon was not observed in all the samples. This indicated that the organic ligands of Cu-BTC were not graphitized during the carbonization. In summary, the Cu^{2+} cation and organic ligands turned into metallic Cu or Cu_2O and carbon matrices with a low graphitization degree, respectively.

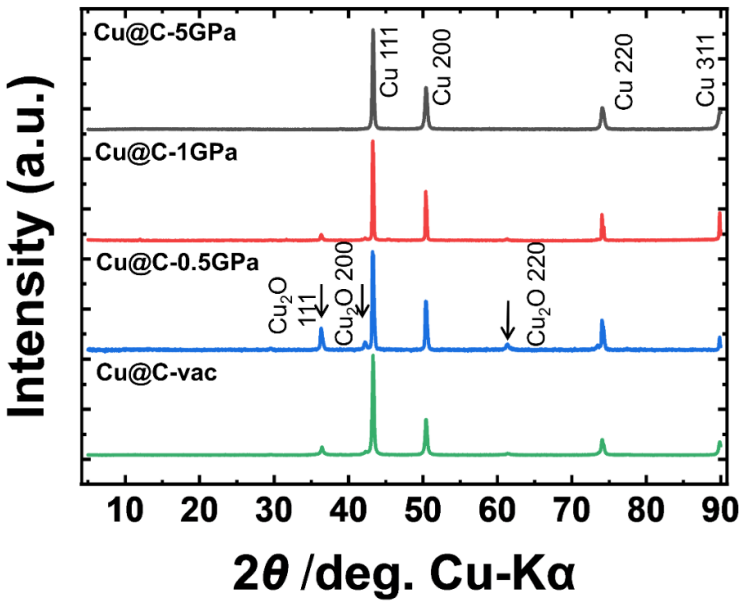

Figure 4-3 Powder XRD patterns of the samples pyrolyzed at various pressures.

Previous studies regarding the pyrolysis of Cu-BTC at ambient pressure are summarized in Table 4-1. The XRD results from those studies included only the peaks of Cu or Cu_2O from the as-prepared samples. The XRD peak of graphitic carbon appeared only after removing the copper by acid washing, which suggests that the graphite peak was very weak. This is consistent with the absence of the graphite peak in the present study. Table 4-1 also revealed that a high temperature and long heating time, for example, 800 °C for 2 h, were required to obtain only metallic Cu from the pyrolysis in an inert atmosphere. However, I successfully obtained the product without oxides from the 5 GPa thermal treatment at a much lower temperature for a shorter time, that is, 500 °C for 15min, despite being done in air. These results indicated that the high-pressure treatment can suppress the formation of copper oxides.

Table 4-1 The comparison of the Cu-BTC pyrolyzed Cu@C by the XRD at various pyrolysis conditions

Ref.	Pyrolysis conditions				Observed diffraction peaks in XRD	
	Temperature /°C	Time /h	Atmosphere	Pressure	Copper speices	Graphitic carbon
[54]	350	2	N_2	1 atm	Cu, Cu_2O	No observed.
[54]	350	2	H_2	1 atm	Cu, Cu_2O	No observed.
[55]	400	1	5% H_2-N_2	1 atm	Cu	No observed.
[56]	400	2	N_2	1 atm	Cu, Cu_2O*	Slightly observed?**
[57]	500	-	N_2	1 atm	Cu, Cu_2O	No observed.
[58]	400	1-4	N_2	1 atm	Cu, CuO, Cu_2O	No observed.
[58]	500	1-4	N_2	1 atm	Cu, CuO, Cu_2O	No observed.
[58]	600	1-4	N_2	1 atm	Cu, Cu_2O	No observed.
[58]	700	1-4	N_2	1 atm	Cu, Cu_2O	No observed.
[59]	700	4	Ar	1 atm	Cu, Cu_2O, CuO	Slightly observed after HCl washing.
[59]	800	4	Ar	1 atm	Cu, Cu_2O, CuO	Slightly observed after HCl washing.
[60]	800	2	Ar	1 atm	Cu	Observed after H_2SO_4 washing.
[61]	850	8	Ar	1 atm	Cu, CuO	No observed.
This work	500	0.25	Vacuum-sealed	Vacuum	Cu, Cu_2O	No observed.
This work	500	0.25	Air	0.5 GPa	Cu, Cu_2O	No observed.
This work	500	0.25	Air	1 GPa	Cu, Cu_2O	No observed.
This work	500	0.25	Air	5 GPa	Cu	No observed.

*: the authors did not state the existence of the Cu_2O diffraction peaks in the XRD pattern, but the pattern had a peak at ~36° that seems to be corresponding to Cu_2O (111) plane. **: the authors state the peak of carbon was observed at 2θ=20°, but the pattern did not seem to have such a peak at the position.

The morphology of the Cu species in the product was investigated by TEM and STEM (Figure 4-4). HAADF-STEM observations revealed that nanoclusters and nanoparticles supported on the matrices existed in the Cu@C-5GPa and the Cu@C-1GPa, respectively (Figure 4-4 (a) and (b)). The materials of these nanoparticles and the matrices were identified as copper and carbon, respectively, using the HAADF-STEM contrast and EDS analysis. . This assignment was confirmed by TEM/STEM-EDS point analysis and mapping measurements (Figure 4-6, 4-7, and 4-8). The result

proved that the products had copper supported on carbon (Cu@C) nanostructures. The sizes of the nanoparticles in the Cu@C-5GPa and the Cu@C-1GPa had diameters of ~1 nm and tens of nm, respectively, whereas the Cu@C-vac contained large particles with a diameter of >1 μm (Figure 4-4 (d)). The sizes of the copper particles in the products are controlled by the applied pressure during the pyrolysis, indicating that the ultrahigh pressure effectively modulated the atomic diffusions.

For the Cu@C-0.5GPa, however, copper did not form particles but was uniformly distributed over the sample powder (Figure 4-4 (d)). Figure 4-5 (a) and (b) show that the edge of the powder contained copper at a high concentration, which was confirmed by the EDS mapping in Figure 4-4 (c). Thus, it was found that the morphology of copper in this sample was different from the other ones and formed thin shells with a thickness of ~4 nm on the surface of the carbon matrices.

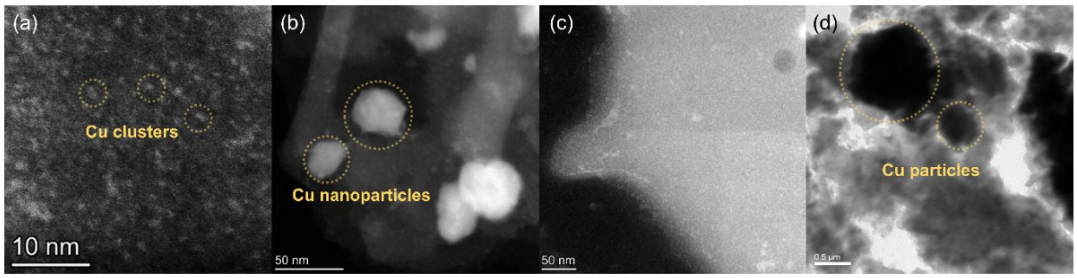

Figure 4-4 HAADF-STEM images of (a)Cu@C-5 GPa, (b)Cu@C-1GPa, (c)Cu@C-0.5 GPa, and the TEM image of (d) Cu@C-vac.

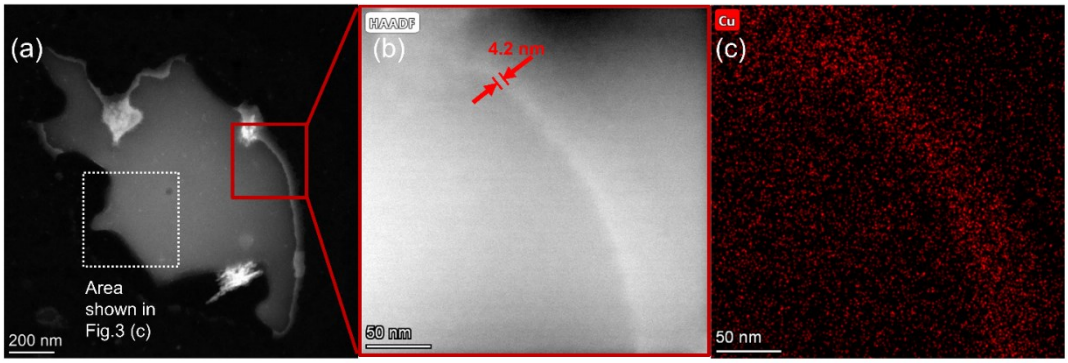

Figure 4-5 HAADF-STEM images at (a) low magnification and (b) and (c) HAADF-STEM images at high magnification of the Cu@C-0.5GPa and corresponding EDS mapping of Cu.

I conducted TEM/STEM-EDS measurements of Cu@C-5GPa, Cu@C-1GPa, and Cu@C-vac to confirm that those observed particles consist of copper. The point analysis of Cu@C-5GPa indicated a significant difference in the Cu peak intensity between the areas with and without particles (Figure 4-6). The analysis of Cu@C-1GPa showed the same results (Figure 4-7). For Cu@C-vac, the EDS mapping clearly shows that the observed particle consists of Cu (Figure 4-8). Thus, it was confirmed that the observed particles in Figure 4-4 were made of copper.

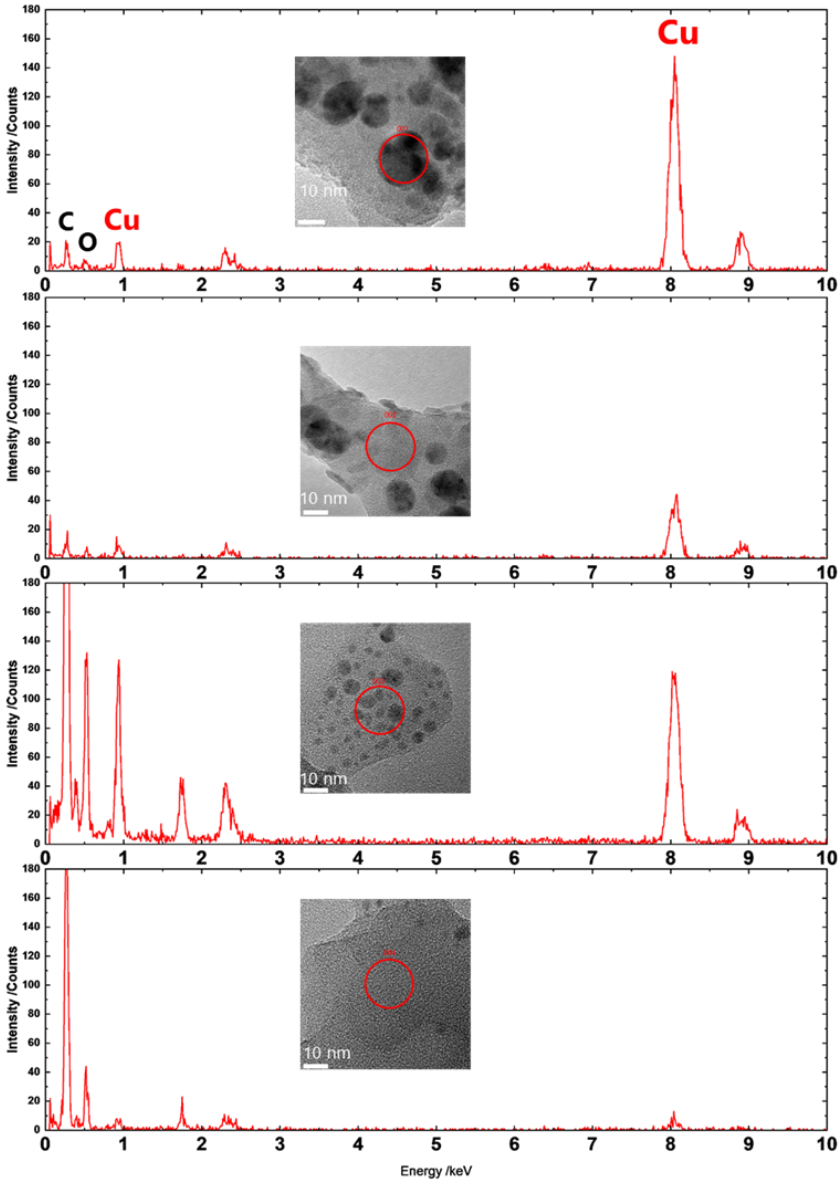

Figure 4-6 The STEM-EDS elemental analysis at multiple points of the Cu@C-5GPa

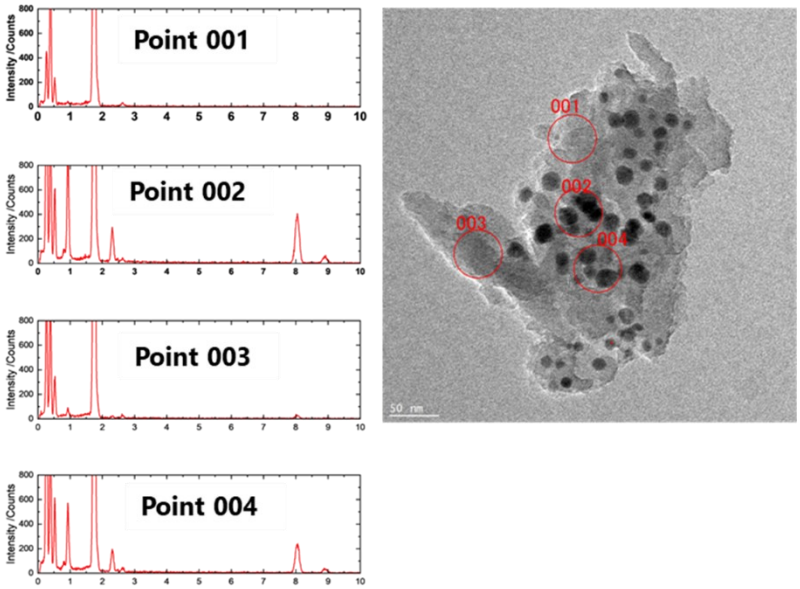

Figure 4-7 The STEM-EDS elemental analysis at multiple points of the Cu@C-1GPa

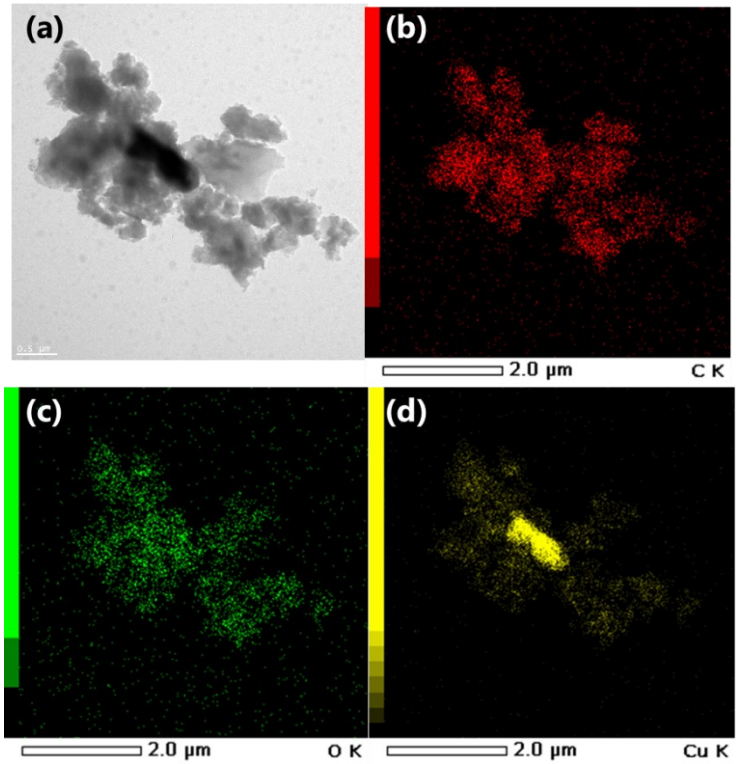

Figure 4-8 (a)TEM image of Cu@C-vac and the STEM-EDS mapping images of (a): (b) C, (c) O, and (d) Cu.

To further evaluate the carbon matrices of Cu@C in the HPHT-treated products, the core-loss EELS spectra of the carbon K-edge were obtained using TEM. Figure 4-9 shows the EELS spectra of our products with those of reference materials traced from Ref. [62]. The spectra of our products had two peaks near 285 and 291 eV the as same as the references, and their shapes were similar to amorphous carbon rather than to graphite. These two peaks are called π* and σ* peaks, which are derived from the π and σ bonds, respectively [62,63]. I estimated the graphitization degree of the sample from the area ratios of the π* peak to the K-edge. The area of the π* peak was calculated by peak separation using the Gaussian function in the range of 280-295 eV. The area of the K-edge was defined as the area in the range of 280-310 eV. The baseline in the above calculations was set to the intensity at 280 eV. As a result, the π* peak/K-edge ratios normalized by that of graphite were 56 % for the Cu@C-0.5GPa, 76% for the Cu@C-1GPa, 23% for the Cu@C-5GPa, 17% for the diamond-like carbon, and 49% for the amorphous carbon. The EELS results revealed that the carbon matrices of the products did not graphitize and formed amorphous carbon. In particular, Cu@C-5GPa had a remarkably poor graphitization degree among the products. Cu nanoparticles in the matrix of Cu@C-5GPa were much smaller than that in the other products (Figure 4-4) and these fine particles probably produced more defects in the matrix. This highly defective structure probably results in a remarkable poor graphitization degree.

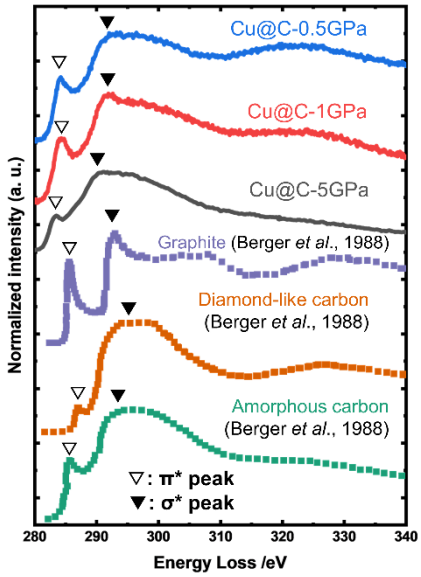

Figure 4-9 TEM-EELS spectra near carbon K -edge of the HPHT-treated samples and reference substances. ▽ and ▼ are, the π* and σ* peaks, respectively. The spectra of the graphite, diamond-like carbon, and amorphous carbon were reproduced from the data of Berger *et al.* [62]

The drastic morphology change in the Cu@C-0.5GPa seems to be related to the outgassing during the HPHT treatments (Figure 4-10). Cu-BTC is a kind of carboxylate salt, which leads to CO_2 evolution by decomposition of the carboxylate groups during heating Cu-BTC. For the experiment at 5 GPa, the evolved CO_2 was confined inside the cell assembly by the ultrahigh applied pressure and it could not go out of the cell. On the other hand, the gentle gas emission to the outside during the treatment was observed at 0.5 GPa. I consider that Cu atoms are carried by CO_2 gas or its gaseous precursors (small Cu-complexes) to the grain boundary of the MOF and deposited there. When the sample is retrieved to ambient conditions, the grains are separated at the grain boundary. As a result, the thin copper shell is exposed at the surface of the particles.

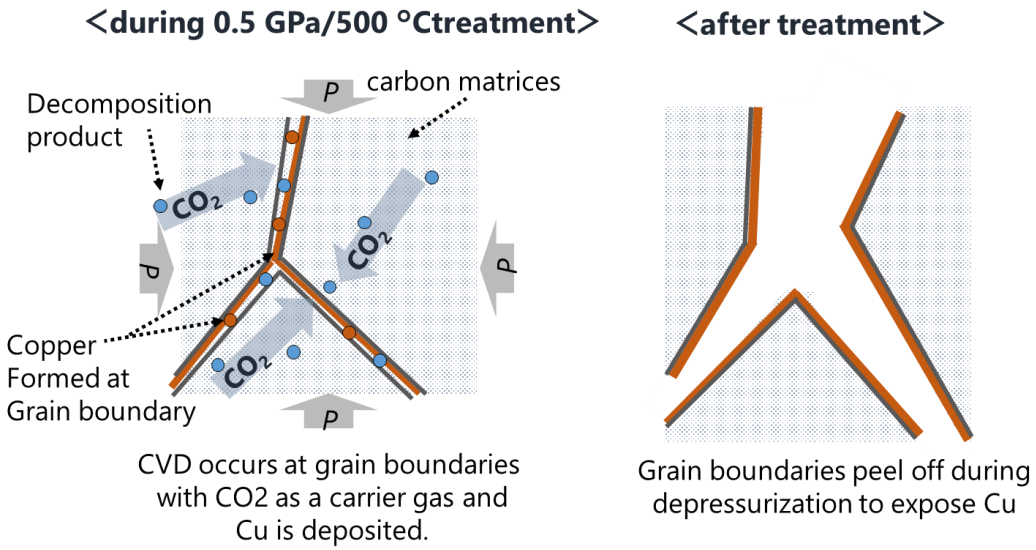

Figure 4-10 The schematic image of the mechanism to form thin-layered Cu in the synthesis of Cu@C-0.5GPa.

I measured the XPS of the samples to evaluate the Cu valency in detail. Figure 4-11 (a) shows XPS narrow scan spectra of Cu $2p_{3/2}$. The broad Cu^{2+} satellite peaks were observed clearly in Cu@C-5GPa and Cu@C-1GPa, whereas those in Cu@C-0.5GPa and Cu@C-vac were weak. The result after peak deconvolution is summarized in

Table 4-2. I also measured Cu LMM AES spectra to distinguish Cu^0 and Cu_2O (Figure 4-11 (b)) because they show almost the same chemical shift in Cu $2p_{3/2}$ XPS spectra. AES showed Cu_2O and Cu^0 peaks at ~916.8 eV and ~918.6 eV, respectively. It is noted that the Cu@C-5GPa did not show Cu^0 component while others did. These results provide the following insight about Cu valences: the average valences of the surface Cu decrease in the order of Cu@C-5GPa, Cu@C-1GPa, Cu@C-0.5GPa, and Cu@C-vac. It

suggests that the surface of Cu nanoparticles is easily oxidized in the air.

Table 4-2 The chemical composition of Cu calculated from Cu $2p_{3/2}$ XPS spectra.

Sample	composition		
	$Cu+Cu_2O$	CuO	$Cu(OH)_2$
Cu@C-5GPa	24.3%	18.2%	57.5%
Cu@C-1GPa	22.4%	17.3%	60.3%
Cu@C-0.5GPa	58.6%	12.0%	29.4%
Cu@C-vac	83.0%	8.79%	8.26%

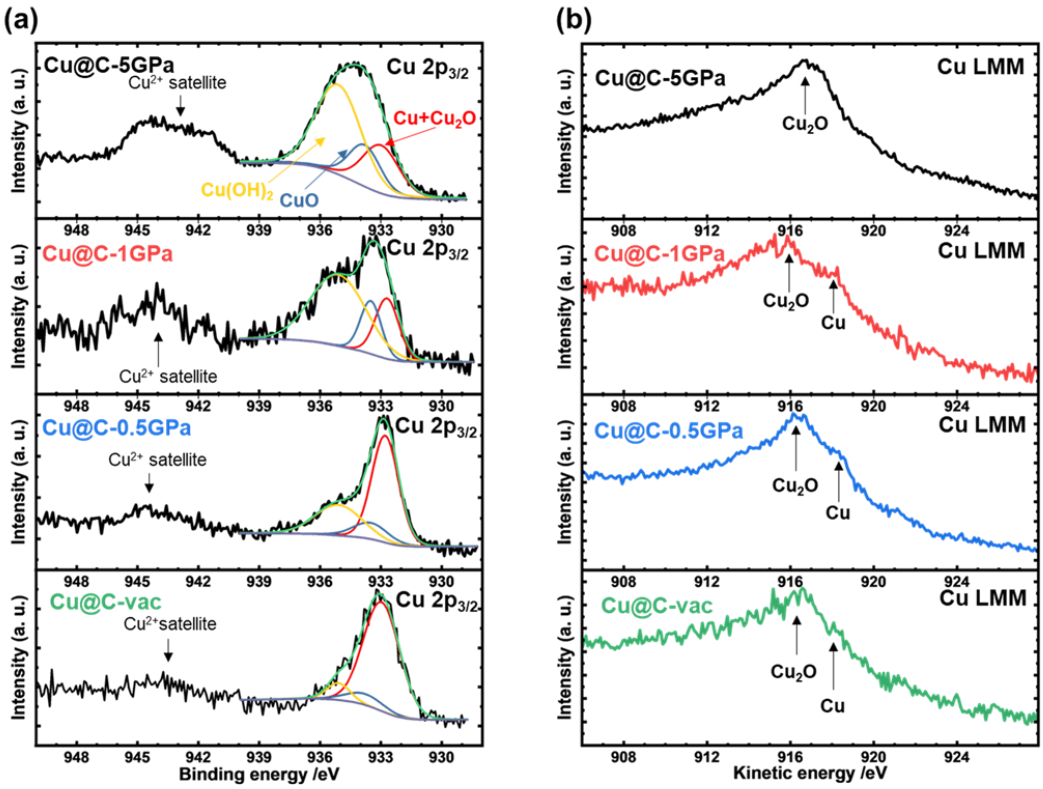

Figure 4-11 (a) Cu $2p_{3/2}$ XPS spectra and curve fitting. Red, blue, yellow, green, and purple curve indicates $Cu+Cu_2O$ component, CuO component, $Cu(OH)_2$ component, fitting curve, and background, respectively. (b)Cu LMM Auger spectra.

4.3.3 Electrocatalytic ORR performance

Cyclic voltammetry (CV) in a N_2 or O_2 saturated 0.1 M KOH aqueous solution was measured to test the electrocatalytic activities toward the ORR. As shown in Figure 4-12, each CV curve, except that of Cu@C-0.5GPa, exhibited a cathodic peak in only the O_2-saturated solutions. It means that the reaction attributed to the cathodic peak was the reduction reaction related to O_2. The shapes of the CV curves resemble that of ORR in the irreversible, electron-transfer-limited case [64–66].

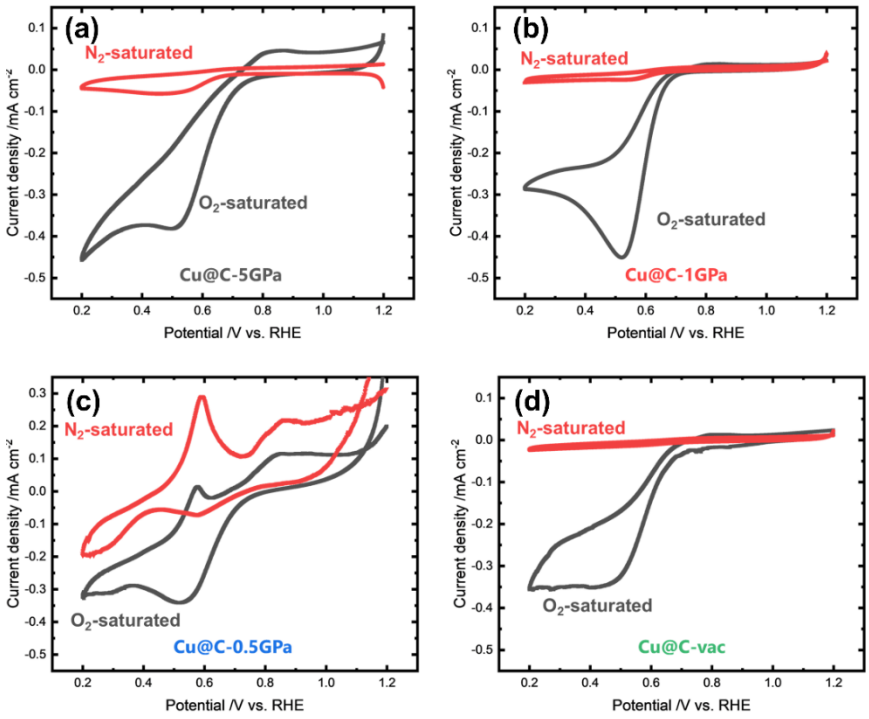

Figure 4-12 CV curves of (a) Cu@C-vac, (b) Cu@C-5GPa, (c) Cu@C-1GPa, and (d) Cu@C-0.5GPa at 10 mV s^{-1} scan rate. The red and black curves are measured in N_2-saturated and O_2-saturated 0.1 M KOH aqueous solutions, respectively.

The CV curve of Cu@C-0.5GPa showed different features from others. Namely, its shape was different from the other products and had not only cathodic but also anodic peaks. The anodic peaks are not derived from the ORR-related reactions, but from the oxidation reactions of copper ($2Cu + 2OH^- \rightarrow Cu_2O + H_2O + 2e^-$) because they were even observed in the N_2-saturated electrolyte. For comparison, the CV curves of the bulk Cu and Cu monolayer on Pt in an Ar-saturated alkaline medium are shown in Figure 4-13 along with those of Cu@C-0.5GPa (The CV data of bulk and monolayer Cu were reproduced from Giri *et al*. [67]). As shown in Figure 4-13, the bulk copper was initially oxidized to Cu_2O at 0.6 V vs. RHE. Subsequently, Cu_2O was further oxidized to $Cu(OH)_2$ and CuO via $Cu(OH)_4^{2-}$ in two steps at 0.9-1.1 V vs. RHE. The Cu monolayer was also reported to show some oxidation peaks. However, the peak positions were shifted to positive compared to that of the bulk copper and the loop shape was different from the bulk. This is commonly observed in thin film heterostructures, for example, Giri *et al*. explained that the peak shift was caused by the Pt underlying the Cu monolayer. The Pt gave nobility to the Cu because of the good affinity of Cu for Pt.

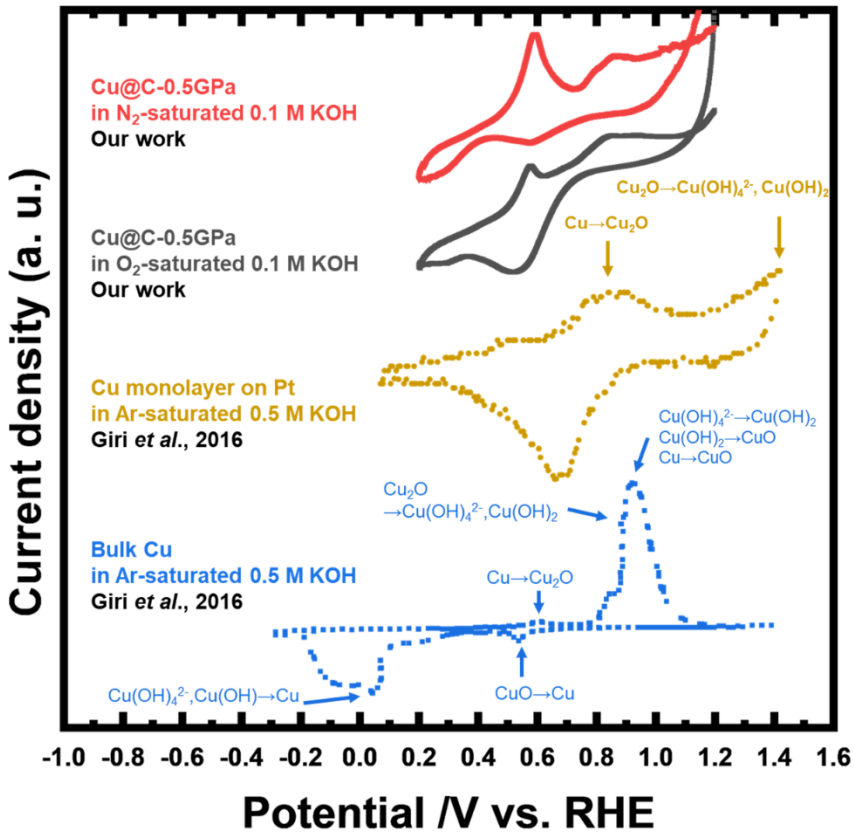

Figure 4-13 The comparison of the CV curves of the Cu@C-0.5GPa in N_2/O_2-saturated 0.1 M KOH, that of the copper monolayer deposited on the 20 wt% platinum nanoparticles supported on carbon electrode in Ar-saturated 0.5 M KOH, and that of bulk copper electrode in Ar-saturated 0.5 M KOH. All curves were measured at scan rate 10 mV/s. Data from Cu monolayer and bulk Cu were digitized from figures in the works of ref. [67] and their potentials were converted from V vs. Hg/HgO to V vs. RHE by the following formula: $E_{RHE} = E_{Hg/HgO} + 0.098$ V + 0.0591×(pH of the 0.5 M KOH).

Compared to the Cu bulk and monolayer (Figure 4-13), the CV curve of Cu@C-0.5GPa had oxidation peaks at the same positions as the bulk CV. Namely, the anodic peaks observed at 0.6 and 0.9-1.1 V were assigned to the oxidation from the metallic Cu to Cu_2O and the further oxidation to CuO and $Cu(OH)_2$. In contrast, the shape of the CV curve for Cu@C-0.5GPa was similar to that of the Cu monolayer. These discrepancies

can be explained by assuming that the shape of the CV curve is related to the morphology of the copper. As shown in Figure 4-5, the copper in Cu@C-0.5GPa was a thin layer (~ 4 nm-thick), not the bulk. I consider that this Cu layer has microstructures and its electronic structure is similar to that of a monolayer, thus affecting the CV characteristics.

CV curves of Cu@C-0.5GPa had cathodic peaks with different potentials in the N_2 and O_2-saturated electrolytes. The peak observed in the N_2-saturated electrolyte corresponded to the reduction of CuO to Cu. The intensity of the peak was weaker than that of the anodic peak at 0.6 V vs. RHE because the copper atoms of the electrode presumably dissolved in the electrolyte as $Cu(OH)_4^{2-}$. On the other hand, in the O_2-saturated electrolyte, the cathodic peak was enhanced and shifted to the negative side. This shows that this cathodic peak was derived from the ORR as well as the CuO reduction reaction. In summary, Cu@CV-0.5GPa showed CV curves with unique shapes because the copper atoms formed thin layers. The copper thin layers had a reactivity for oxidation while other products did not.

Figure 4-14 (a) shows the linear sweep voltammetry (LSV) results in the O_2-saturated 0.1 M KOH aqueous solution using a rotating disk electrode (RDE) for detailed evaluations of the ORR activity. The onset potentials, E_{onset}, of the samples synthesized at the Cu@C-5GPa, the Cu@C-1GPa, the Cu@C-0.5GPa, and the Cu@C-vac were 0.66,

0.61, 0.65, and 0.66 V vs. RHE, respectively, implying that the HPHT-treatments did not improve the E_{onset}. Each LSV curve had kinetic-, mixed- and diffusion-controlled regions though the plateau in the diffusion-controlled region was not very clear. This suggests the another cathodic reaction occurred.

Tafel plots from the LSV curves measured at 1600 rpm are shown in Figure 4-14(b) to evaluate the kinetics of the ORR in detail. The samples, except for the Cu@C-0.5GPa, had the two steps corresponding to different Tafel slopes, indicating that the ORR mechanism changes with the potential. This phenomenon can be caused by the decrease in the coverage of the absorbed species on the catalyst or the oxidation number on the active sites [68,69]. However, the linear plot in low current density region were presumably derived from not ORR but the other reactions because corresponding Tafel slopes were too large. The analysis of the electron transfer numbers regarding the ORR was conducted by the Koutecký-Levich plots. As shown in Figure 4-14(c), the plots demonstrate a good linearity. The electron transfer number *n* of the Cu@C-5GPa, the Cu@C-1GPa, the Cu@C-0.5GPa, and the Cu@C-vac were calculated from the slope of each plot, resulting in about 1.8, 2.8, 1.5, and 2.4, respectively. This indicated that the ORR for each product dominantly proceeds not by the four-electron pathway that generates H_2O, but by the two-electron pathway that generates hydrogen peroxide. I did

not observe any significant synergetic role of Cu_2O in the Cu@C-0.5GPa in the ORR data.

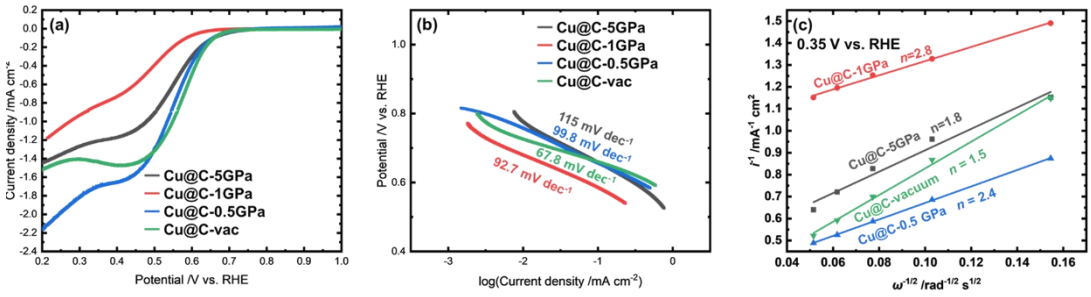

Figure 4-14 (a) LSV curves of ORR for the products in O_2-saturated 0.1 M KOH aqueous solution at the rotation rates of 1600 rpm and scan rates of 5 mV s^{-1}. (b) Tafel plot of ORR for the products. (c) Koutecký-Levich plots of the products at 0.35 V vs. RHE, where *i* and *ω* are disk current density and disk rotating speed, respectively.

4.3.4 Electrocatalytic OER performance

I conducted CV measurements in N_2-saturated 0.1 M KOH aqueous solutions to evaluate the OER electrocatalytic activities of the products (Figure 4-15 (a)). The CV curve of Cu@C-0.5GPa showed a distinct catalytic activity toward the OER. In addition, the curve exhibited a cathodic peak at 1.5-1.6 V vs. RHE. This cathodic peak had been assigned to the reduction of Cu(III) to Cu(II) in previous studies [70–72]. This indicated that Cu@C-0.5GPa include Cu(III) species during the oxidation scan. The kinetics of the OER in each product was evaluated by the LSV measurements at rotation scans of 1600 rpm (Figure 4-15(b)). The Tafel plots obtained by the LSV curves are shown in

Figure 4-15(c). The Tafel slopes of Cu@C-5GPa, Cu@C-1GPa, Cu@C-0.5GPa, and Cu@C-vac were 278, 230, 160, and 244 mV/dec, respectively. These results revealed that the CU@C-0.5GPa works as a bifunctional electrocatalyst for the OER/ORR.

The CV curve of Cu@C-0.5GPa in Figure 4-15(a) indicated that Cu(III) species was contained in the Cu@C-0.5GPa during the oxidation scan for the OER. This result is supported by the fact that Cu was oxidized to the Cu(II) state in the scan from 0.2 to 1.2 V vs. RHE (Figure 4-12 and Figure 4-13). It was reported that Cu(III) species enhances the OER catalytic activity [70,73], and this probably produces the highest OER performance for Cu@C-0.5GPa. On the other hand, the copper in other products exhibited poor activity for OER.

In those products, copper formed a morphology different from that of Cu@C-0.5GPa, with fine particles embedded in the carbon matrices. Cu@C-5GPa and Cu@C-1GPa contained Cu NPs with the oxidated surface (Figure 4-11), and the CV results indicate that the surface was low activity. Cu@C-vac included the Cu particles with larger size and less oxidated surface than the others. The CV results indicated that the particles exhibited an oxidation resistance. It suggests that the surface of the particles is encapsulated by a very thin shell of amorphous carbon. In summary, the difference in the morphology would affect the oxidation state of copper during the electrochemical processes, and then these states modified the OER performance.

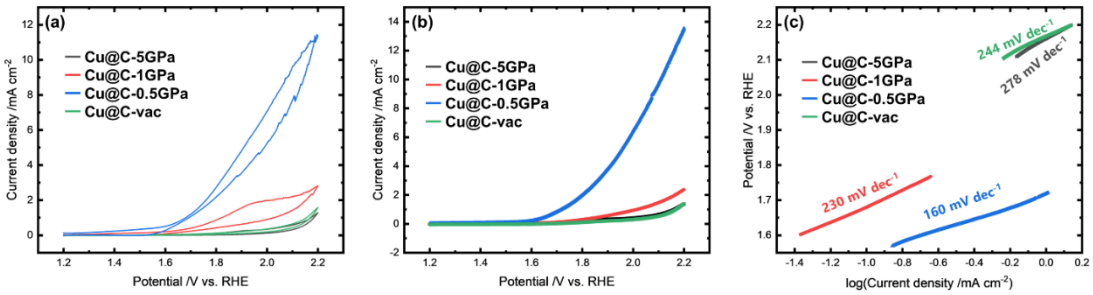

Figure 4-15 (a) CV curves of OER for the products in N_2-saturated 0.1 M KOH aqueous solution at the scan rate of 10 mV s^{-1} and (b) LSV curves of OER for the products in N_2-saturated 0.1 M KOH aqueous solution at the rotation rate of 1600 rpm and scan rate of 5 mV s^{-1}. (c) Tafel plot of OER for the products.

4.3.5 The comparison with other copper-based bifunctional electrocatalysts for the ORR/OER

The performance comparison of recently-reported Cu-based ORR/OER bifunctional electrocatalysts is shown in Figure 4-16 , Figure 4-17, and Table 4-3. In Figure 4-16, the overall performance was evaluated by Tafel slope. When the distance between a plotted point and the origin is smaller, the performance of the electrocatalyst is higher. This is because the lower value of the Tafel slopes means faster kinetics in the electrochemical processes. Thus Figure 4-16 reveals that the overall performance of Cu@C-0.5GPa was superior to most of the copper-based OER/ORR bifunctional electrocatalysts except for the Co-containing ones. As shown in Table 4-3 and Figure 4-16, the Cu-based OER/ORR electrocatalysts are often supported on nitrogen-doped carbon (NC) for enhanced performance. NC is useful for the following reasons: the pyridinic-N in NC

itself acts as the electrocatalyst for the ORR [74]; it can anchor metal atoms with N atoms that improved their dispersion [21]. Figure 4-16 also shows that the Cu-based OER/ORR electrocatalysts were often combined with other metal elements, such as Co, Ni, and Fe, to improve their performance. It is noted that Cu@C-0.5GPa exhibited an overall performance comparable to or higher than those even though it does not contain NC or other metal elements. This result revealed that the performance of the Cu-based OER/ORR bifunctional electrocatalysts can be further improved by controlling the morphology of the copper nanostructures.

In Figure 4-17, the overall performance was evaluated by exchange current density i_0 obtained from the extrapolation of the Tafel plot. This figure indicates that the Cu-0.5GPa exhibited the best overall performance among the products synthesized in this work as well as Figure 4-16. However, it also reveals that our products are inferior to other Cu-based electrocatalysts from the viewpoint of the exchange current density.

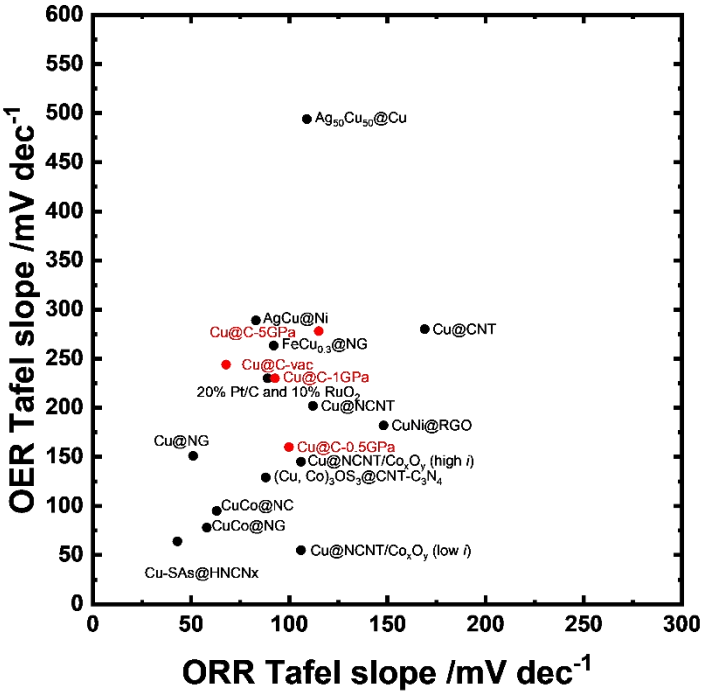

Figure 4-16 The performance comparison of the reported copper-based bifunctional electrocatalyst by Tafel slope. The plotted points were the data from the contents of Table 4-3. The red points are the data from this study.

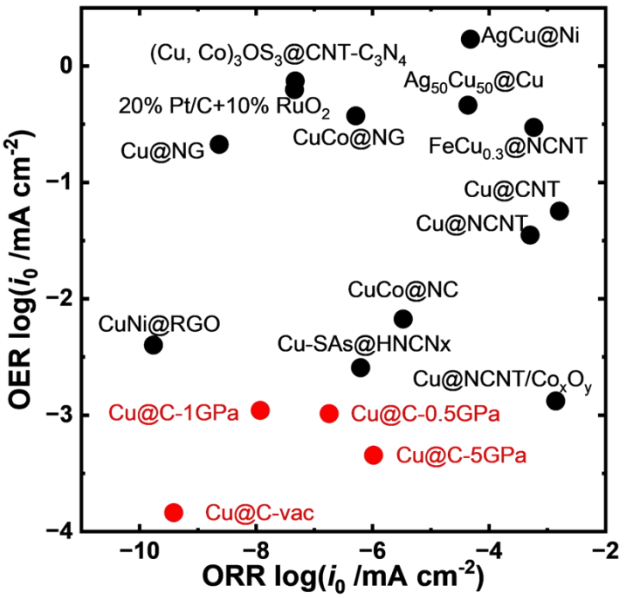

Figure 4-17 The performance comparison of the reported copper-based bifunctional electrocatalyst by exchange current density i_0. The plotted points were the data from the contents of Table 4-3. The red points are the data from this study.

Table 4-3 The performance comparison of the reported copper-based bifunctional electrocatalyst. The underlined values are data digitized from LSV curves or Tafel plots in the works of literature. CNT stands for carbon nanotubes; NCNT stands for nitrogen-doped CNT; SAs stands for single-atoms; HNCNx stands for hollow nano-spheroids of nitrogen-deficient carbon nitride frameworks; NC stands for nitrogen-doped carbonaceous nanoleaves; NG stands for nitrogen-doped graphene; RGO stands for reduced graphene oxides.

Materials	Cu species Morphology	Medium	Tafel slope /mV dec^{-1}		log(i_0/mA cm^{-2})		Ref.
			ORR	OER	ORR	OER	
$(Cu, Co)_3OS_3$ @CNT-C_3N_4	Nanoparticles @honeycomb-like porous nanosheets	0.1 M KOH	88	129	-7.33	-0.129	[75]
20% Pt/C and 10% RuO_2	-	0.1 M KOH	89	230	-7.34	-0.203	[75]
$Ag_{50}Cu_{50}$ @Cu	Nanoparticles @amorphous film	0.1 M KOH	109	494	-4.36	-0.336	[76]
Cu@CNT	Nanoparticles @nanotubes	0.1 M KOH	169	280	-2.79	-1.24	[77]
Cu@NCNT	Nanoparticles @nanotubes	0.1 M KOH	112	202	-3.30	-1.45	[77]
Cu@NCNT/Co_xO_y	Nanoparticles @nanotubes/nanoparticles	0.1 M KOH	106	55(low *i*) 145 (high *i*)	-2.86	-2.88 1.65	[77]
Cu-SAs@HNCNx	single atoms@ hollow nanospheroids	0.1 M KOH	43	64	-6.21	--2.59	[78]
CuCo@NC	Nanoparticles @nanoleaves	0.1 M KOH(ORR), 1.0 M KOH(OER)	63	95	-5.48	-2.17	[79]
AgCu@Ni	Nanoparticles@foam	0.1 M KOH	83	289	-4.32	0.231	[80]
CuCo@NG	Nanoparticles@nanosheets	0.1 M KOH	58	78	-6.29	-0.428	[81]
Cu@NG	Nanoparticles@nanosheets	0.1 M KOH	51	151	-8.63	-0.674	[81]
CuNi@RGO	Nanoparticles@nanosheets	0.5M KOH	148	182	-9.76	-2.40	[82]
$FeCu_{0.3}$ @NCNT	Nanoparticles@nanotubes	0.1 M KOH	92.1	263.4	-3.23	-0.528	[83]
Cu@C-5GPa	**Cluster@particles**	**0.1 M KOH**	**115**	**278**	**-5.98**	**-3.34**	**This work**
Cu@C -1GPa	**Nanoparticles@particles**	**0.1 M KOH**	**92.7**	**230**	**-3.81 -7.92**	**-2.96**	**This work**
Cu@C-0.5GPa	**Thin shell@particles**	**0.1 M KOH**	**99.8**	**160**	**-6.74**	**-2.99**	**This work**
Cu@C-vac	**microparticles@particles**	**0.1 M KOH**	**424 (low *i*) 67.8 (high *i*)**	**244**	**-3.63 -9.42**	**-3.84**	**This work**

4.4 Conclusions

I synthesized Cu@C composite materials from Cu-BTC by high-pressure and high-temperature treatments, where the applied pressures were 5, 1, and 0.5 GPa. Copper formed fine particles in the carbon matrices in the experiments at 5 and 1 GPa and the sizes became smaller with an increase in the applied pressure. On the other hand, the

copper formed thin layers with thicknesses of ~4 nm on the carbon matrices at 0.5 GPa. The nano-layered Cu morphology at 0.5 GPa probably comes from the transportation and the deposition of Cu atoms at grain boundaries during the CO_2 evolution from decomposed MOF. The difference in the oxidation resistance affected the electrocatalytic performance, and the OER performance of the 0.5 GPa-treated product was enhanced by the Cu(III) species generated during the oxidation scan. The 0.5GPa-treated product can work as a bifunctional electrocatalyst because it also exhibited an activity for the ORR as with other products. Its overall performance was comparable to other copper-based bifunctional electrocatalysts which contain N-doped carbon or other metals such as Ni and Fe. The pressure of 0.5 GPa can be generated by large-volume high-pressure apparatuses such as piston cylinders. Therefore, the method proposed in this study is feasible for mass production.

References

[1] J. Su, R. Ge, Y. Dong, F. Hao, and L. Chen, *Recent Progress in Single-Atom Electrocatalysts: Concept, Synthesis, and Applications in Clean Energy Conversion*, J. Mater. Chem. A **6**, 14025 (2018).

[2] D. A. Ruddy, J. A. Schaidle, J. R. Ferrell III, J. Wang, L. Moens, and J. E. Hensley, *Recent Advances in Heterogeneous Catalysts for Bio-Oil Upgrading via "Ex Situ Catalytic Fast Pyrolysis": Catalyst Development through the Study of Model Compounds*, Green Chem. **16**, 454 (2014).

[3] Q. Liu, M. Ranocchiari, and J. A. van Bokhoven, *Catalyst Overcoating Engineering towards High-Performance Electrocatalysis*, Chem. Soc. Rev. **51**, 188 (2022).

[4] B. I. Whittington, C. J. Jiang, and D. L. Trimm, *Vehicle Exhaust Catalysis: I. The Relative Importance of Catalytic Oxidation, Steam Reforming and Water-Gas Shift Reactions*, Catal. Today **26**, 41 (1995).

[5] Y. Li, Y. Sun, Y. Qin, W. Zhang, L. Wang, M. Luo, H. Yang, and S. Guo, *Recent Advances on Water-Splitting Electrocatalysis Mediated by Noble-Metal-Based Nanostructured Materials*, Adv. Energy Mater. **10**, 1903120 (2020).

[6] M. Shelef and G. W. Graham, *Why Rhodium in Automotive Three-Way Catalysts?*, Catal. Rev. - Sci. Eng. **36**, 433 (1994).

[7] Z. Zhou, X. Li, Q. Li, Y. Zhao, and H. Pang, *Copper-Based Materials as Highly Active Electrocatalysts for the Oxygen Evolution Reaction*, Mater. Today Chem. **11**, 169 (2019).

[8] C. Hu, L. Zhang, and J. Gong, *Recent Progress Made in the Mechanism Comprehension and Design of Electrocatalysts for Alkaline Water Splitting*, Energy Environ. Sci. **12**, 2620 (2019).

[9] F. Xiao et al., *Recent Advances in Electrocatalysts for Proton Exchange Membrane Fuel Cells and Alkaline Membrane Fuel Cells*, Adv. Mater. **33**, 2006292 (2021).

[10] X. Ge, A. Sumboja, D. Wuu, T. An, B. Li, F. W. T. Goh, T. S. A. Hor, Y. Zong, and Z. Liu, *Oxygen Reduction in Alkaline Media: From Mechanisms to Recent Advances of Catalysts*, ACS Catal. **5**, 4643 (2015).

[11] D. U. Lee, P. Xu, Z. P. Cano, A. G. Kashkooli, M. G. Park, and Z. Chen, *Recent Progress and Perspectives on Bi-Functional Oxygen Electrocatalysts for Advanced Rechargeable Metal–Air Batteries*, J. Mater. Chem. A **4**, 7107 (2016).

[12] X.-T. Xu, L. Pan, X. Zhang, L. Wang, and J.-J. Zou, *Rational Design and Construction of Cocatalysts for Semiconductor-Based Photo-Electrochemical Oxygen Evolution: A Comprehensive Review*, Adv. Sci. **6**, 1801505 (2019).

[13] C.-W. Ye and L. Xu, *Recent Advances in the Design of a High Performance Metal–Nitrogen–Carbon Catalyst for the Oxygen Reduction Reaction*, J. Mater. Chem. A **9**, 22218 (2021).

[14] T. Zhang, Y. Zhu, and J. Y. Lee, *Unconventional Noble Metal-Free Catalysts for Oxygen Evolution in Aqueous Systems*, J. Mater. Chem. A **6**, 8147 (2018).

[15] A. Miura, C. Rosero-Navarro, Y. Masubuchi, M. Higuchi, S. Kikkawa, and K. Tadanaga, *Nitrogen-Rich Manganese Oxynitrides with Enhanced Catalytic Activity in the Oxygen Reduction Reaction*, Angew. Chem. Int. Ed. **55**, 7963 (2016).

[16] Y. Li, K. A. Kuttiyiel, L. Wu, Y. Zhu, E. Fujita, R. R. Adzic, and K. Sasaki, *Enhancing Electrocatalytic Performance of Bifunctional Cobalt–Manganese-Oxynitride Nanocatalysts on Graphene*, ChemSusChem **10**, 68 (2017).

[17] M. Chisaka, A. Ishihara, K. Ota, and H. Muramoto, *Synthesis of Carbon-Supported Titanium Oxynitride Nanoparticles as Cathode Catalyst for Polymer Electrolyte Fuel Cells*, Electrochim. Acta **113**, 735 (2013).

[18] M. A. Ashraf, C. Li, B. T. Pham, and D. Zhang, *Electrodeposition of Ni–Fe–Mn Ternary Nanosheets as Affordable and Efficient Electrocatalyst for Both Hydrogen and Oxygen Evolution Reactions*, Int. J. Hydrog. Energy **45**, 24670 (2020).

[19] J. Chen et al., *Enhanced Electrocatalysis of NiMnIn Heusler Alloy Films for Hydrogen Evolution Reaction by Magnetic Field*, Journal of Alloys and Compounds **877**, 160271 (2021).

[20] S. Bai, M. Yang, J. Jiang, X. He, J. Zou, Z. Xiong, G. Liao, and S. Liu, *Recent Advances of MXenes as Electrocatalysts for Hydrogen Evolution Reaction*, NPJ 2D Mater. Appl. **5**, 1 (2021).

[21] Y.-S. Wei, M. Zhang, R. Zou, and Q. Xu, *Metal–Organic Framework-Based Catalysts with Single Metal Sites*, Chem. Rev. **120**, 12089 (2020).

[22] W. Liu et al., *Graphene Quantum Dots-Based Advanced Electrode Materials: Design, Synthesis and Their Applications in Electrochemical Energy Storage and Electrocatalysis*, Adv. Energy Mater. **10**, 2001275 (2020).

[23] Q. Li, S. Zhang, L. Dai, and L. Li, *Nitrogen-Doped Colloidal Graphene Quantum Dots and Their Size-Dependent Electrocatalytic Activity for the Oxygen Reduction Reaction*, J. Am. Chem. Soc. **134**, 18932 (2012).

[24] H. Kita, H. Nakajima, and K. Hayashi, *Electrochemical Oxidation of CO on Au in Alkaline Solution*, J. Electroanal. Chem. Interf. Electrochem. **190**, 141 (1985).

[25] X. Han, G. He, Y. He, J. Zhang, X. Zheng, L. Li, C. Zhong, W. Hu, Y. Deng, and T.-Y. Ma, *Engineering Catalytic Active Sites on Cobalt Oxide Surface for Enhanced Oxygen Electrocatalysis*, Adv. Energy Mater. **8**, 1702222 (2018).

[26] B. Wei, Y. Xiong, Z. Zhang, J. Hao, L. Li, and W. Shi, *Efficient Electrocatalytic Reduction of CO_2 to HCOOH by Bimetallic In-Cu Nanoparticles with Controlled Growth Facet*, Appl. Catal. B **283**, 119646 (2021).

[27] B. Shen, L. Huang, J. Shen, K. He, C. Y. Zheng, V. P. Dravid, C. Wolverton, and C. A. Mirkin, *Crystal Structure Engineering in Multimetallic High-Index Facet Nanocatalysts*, Proc. Natl. Acad. Sci. U.S.A. **118**, e2105722118 (2021).

[28] J. P. S. Walsh and D. E. Freedman, *High-Pressure Synthesis: A New Frontier in the Search*

for Next-Generation Intermetallic Compounds, Acc. Chem. Res. **51**, 1315 (2018).

[29] L. Zhang, Y. Wang, J. Lv, and Y. Ma, *Materials Discovery at High Pressures*, Nat. Rev. Mater. **2**, 17005 (2017).

[30] X. Wang and X. Liu, *High Pressure: A Feasible Tool for the Synthesis of Unprecedented Inorganic Compounds*, Inorg. Chem. Front. **7**, 2890 (2020).

[31] I. Yamada, K. Takata, N. Hayashi, S. Shinohara, M. Azuma, S. Mori, S. Muranaka, Y. Shimakawa, and M. Takano, *A Perovskite Containing Quadrivalent Iron as a Charge-Disproportionated Ferrimagnet*, Angew. Chem. Int. Ed. **47**, 7032 (2008).

[32] I. Yamada, H. Fujii, A. Takamatsu, H. Ikeno, K. Wada, H. Tsukasaki, S. Kawaguchi, S. Mori, and S. Yagi, *Bifunctional Oxygen Reaction Catalysis of Quadruple Manganese Perovskites*, Adv. Mater. **29**, 1603004 (2017).

[33] S. Xu et al., *Pressure-Driven Catalyst Synthesis of Co-Doped Fe_3C@Carbon Nano-Onions for Efficient Oxygen Evolution Reaction*, Appl. Catal. B **268**, 118385 (2020).

[34] S. Xu et al., *Pressure-Promoted Irregular $CoMoP_2$ Nanoparticles Activated by Surface Reconstruction for Oxygen Evolution Reaction Electrocatalysts*, J. Mater. Chem. A **8**, 2001 (2020).

[35] R. Tian et al., *Pressure-Promoted Highly-Ordered Fe-Doped-Ni2B for Effective Oxygen Evolution Reaction and Overall Water Splitting*, J. Mater. Chem. A **9**, 6469 (2021).

[36] I. Yamane, K. Sato, R. Otomo, T. Yanase, A. Miura, T. Nagahama, Y. Kamiya, and T. Shimada, *Ultrahigh-Pressure Preparation and Catalytic Activity of MOF-Derived Cu Nanoparticles*, Nanomaterials **11**, 4 (2021).

[37] H. Liu, S. Zhang, Y. Liu, Z. Yang, X. Feng, X. Lu, and F. Huo, *Well-Dispersed and Size-Controlled Supported Metal Oxide Nanoparticles Derived from MOF Composites and Further Application in Catalysis*, Small **11**, 3130 (2015).

[38] A. Kim, N. Muthuchamy, C. Yoon, S. Joo, and K. Park, *MOF-Derived Cu@Cu2O Nanocatalyst for Oxygen Reduction Reaction and Cycloaddition Reaction*, Nanomaterials **8**, 138 (2018).

[39] S. Dang, Q.-L. Zhu, and Q. Xu, *Nanomaterials Derived from Metal–Organic Frameworks*, Nat. Rev. Mater. **3**, 1 (2017).

[40] K. Shen, X. Chen, J. Chen, and Y. Li, *Development of MOF-Derived Carbon-Based Nanomaterials for Efficient Catalysis*, ACS Catal. **6**, 5887 (2016).

[41] Y. Qian, Q. Liu, E. Sarnello, C. Tang, M. Chng, J. Shui, T. Li, S. J. Pennycook, M. Han, and D. Zhao, *MOF-Derived Carbon Networks with Atomically Dispersed Fe–N_x Sites for Oxygen Reduction Reaction Catalysis in Acidic Media*, ACS Materials Lett. **1**, 37 (2019).

[42] S. H. Ahn, M. J. Klein, and A. Manthiram, *1D Co- and N-Doped Hierarchically Porous Carbon Nanotubes Derived from Bimetallic Metal Organic Framework for Efficient Oxygen and Tri-Iodide Reduction Reactions*, Adv. Energy Mater. **7**, 1601979 (2017).

[43] W. Chen et al., *Single Tungsten Atoms Supported on MOF-Derived N-Doped Carbon for*

Robust Electrochemical Hydrogen Evolution, Adv. Mater. **30**, 1800396 (2018).

[44] Y. Chen et al., *Isolated Single Iron Atoms Anchored on N-Doped Porous Carbon as an Efficient Electrocatalyst for the Oxygen Reduction Reaction*, Angew. Chem. Int. Ed. **56**, 6937 (2017).

[45] P. Yin et al., *Single Cobalt Atoms with Precise N-Coordination as Superior Oxygen Reduction Reaction Catalysts*, Angew. Chem. Int. Ed. **55**, 10800 (2016).

[46] B. Jiang, H. Sun, T. Yuan, W. He, C. Zheng, H.-J. Zhang, J. Yang, and S. Zheng, *Framework-Derived Tungsten Single-Atom Catalyst for Oxygen Reduction Reaction*, Energy Fuels **35**, 8173 (2021).

[47] J. Wang et al., *ZIF-8 with Ferrocene Encapsulated: A Promising Precursor to Single-Atom Fe Embedded Nitrogen-Doped Carbon as Highly Efficient Catalyst for Oxygen Electroreduction*, Small **14**, e1704282 (2018).

[48] M. Liu, Q. Xu, Q. Miao, S. Yang, P. Wu, G. Liu, J. He, C. Yu, and G. Zeng, *Atomic Co–N_4 and Co Nanoparticles Confined in COF@ZIF-67 Derived Core–Shell Carbon Frameworks: Bifunctional Non-Precious Metal Catalysts toward the ORR and HER*, J. Mater. Chem. A **10**, 228 (2021).

[49] C. T. Candland, D. L. Decker, and H. B. Vanfleet, *Interstitial Diffusion of Copper in Lead at Pressures up to 56 Kbar*, Phys. Rev. B **5**, 2085 (1972).

[50] G. Rein and H. Mehrer, *Effect of Hydrostatic Pressure and Temperature on the Self-Diffusion Rate in Single Crystals of Silver and Gold*, Philos. Mag. A **45**, 467 (1982).

[51] N. L. Peterson, *Self-Diffusion in Pure Metals*, J. Nucl. Mater. **69–70**, 3 (1978).

[52] J. Wang, B. Chen, Q. Williams, and M. H. Manghnani, *Short- and Intermediate-Range Structure and Dynamics of Fe-Ni-C Liquid Under Compression*, Front. Earth Sci. **7**, (2019).

[53] R. Zhou, Y. Zheng, M. Jaroniec, and S.-Z. Qiao, *Determination of the Electron Transfer Number for the Oxygen Reduction Reaction: From Theory to Experiment*, ACS Catal. **6**, 4720 (2016).

[54] Y. Zhao, X. Wu, J. Zhou, Y. Wang, S. Wang, and X. Ma, *MOF-Derived Cu@C Catalyst for the Liquid-Phase Hydrogenation of Esters*, Chem. Lett. **47**, 883 (2018).

[55] Q. Gong, L.-P. Sun, Z. Wu, L.-H. Huo, and H. Zhao, *Enhanced Non-Enzymatic Glucose Sensing of Cu–BTC-Derived Porous Copper@carbon Agglomerate*, J. Mater. Sci. **53**, 10 (2018).

[56] H. Tan, C. Ma, L. Gao, Q. Li, Y. Song, F. Xu, T. Wang, and L. Wang, *Metal–Organic Framework-Derived Copper Nanoparticle@Carbon Nanocomposites as Peroxidase Mimics for Colorimetric Sensing of Ascorbic Acid*, Chem. Eur. J. **20**, 16377 (2014).

[57] Y. Yao et al., *Roles of Cu^+ and Cu^0 Sites in Liquid-Phase Hydrogenation of Esters on Core-Shell $CuZn_x$@C Catalysts*, Appl. Catal. B **267**, 118698 (2020).

[58] B. Wang, H. Pan, X. Lu, L. He, H. Zhang, X. Li, H. Guo, D. Zhou, and Q. Xia, *Copper-Organic Framework-Derived Porous Nanorods for Chemoselective Hydrogenation of*

Quinoline Compounds at an Aqueous/Oil Interface, ACS Appl. Nano Mater. **4**, 11779 (2021).

[59] I. A. Khan, A. Badshah, M. A. Nadeem, N. Haider, and M. A. Nadeem, *A Copper Based Metal-Organic Framework as Single Source for the Synthesis of Electrode Materials for High-Performance Supercapacitors and Glucose Sensing Applications*, Int. J. Hydrogen Energy **39**, 19609 (2014).

[60] L. Qiao, A. Zhu, Y. Liu, Y. Bian, R. Dong, D. Zhong, H. Wu, and J. Pan, *Metal–Organic Framework-Driven Copper/Carbon Polyhedron: Synthesis, Characterization and the Role of Copper in Electrochemistry Properties*, J. Mater. Sci. **53**, 7755 (2018).

[61] X. Zhang, J. Luo, P. Tang, J. R. Morante, J. Arbiol, C. Xu, Q. Li, and J. Fransaer, *Ultrasensitive Binder-Free Glucose Sensors Based on the Pyrolysis of in Situ Grown Cu MOF*, Sens. Actuators B Chem. **254**, 272 (2018).

[62] S. D. Berger, D. R. McKenzie, and P. J. Martin, *EELS Analysis of Vacuum Arc-Deposited Diamond-like Films*, Philos. Mag. Lett. **57**, 285 (1988).

[63] S. Urbonaite, S. Wachtmeister, C. Mirguet, E. Coronel, W. Y. Zou, S. Csillag, and G. Svensson, *EELS Studies of Carbide Derived Carbons*, Carbon **45**, 2047 (2007).

[64] K. ur Rehman, S. Airam, L. Song, J. Gao, Q. Guo, Y. Xiao, and Z. Zhang, *MnS-Nanoparticles-Decorated Three-Dimensional Graphene Hybrid as Highly Efficient Bifunctional Electrocatalyst for Hydrogen Evolution Reaction and Oxygen Reduction Reaction*, Catalysts **10**, 10 (2020).

[65] K. Huang et al., *Novel Graphite-Carbon Encased Tungsten Carbide Nanocomposites by Solid-State Reaction and Their ORR Electrocatalytic Performance in Alkaline Medium*, Electrochim. Acta **174**, 172 (2015).

[66] Y. Xu, C. Chen, M. Zhou, G. Fu, Y. Zhao, and Y. Chen, *Improved Oxygen Reduction Activity of Carbon Nanotubes and Graphene through Adenine Functionalization*, RSC Adv. **7**, 26722 (2017).

[67] S. D. Giri and A. Sarkar, *Electrochemical Study of Bulk and Monolayer Copper in Alkaline Solution*, J. Electrochem. Soc. **163**, H252 (2016).

[68] T. Poux, A. Bonnefont, G. Kéranguéven, G. A. Tsirlina, and E. R. Savinova, *Electrocatalytic Oxygen Reduction Reaction on Perovskite Oxides: Series versus Direct Pathway*, ChemPhysChem **15**, 2108 (2014).

[69] Q. Li, X. Zhou, Z. Wei, G. Du, G. Zhang, and N. Chen, *Electrocatalytic Activity of $LaSr_3Fe_3O_{10}$ and $LaSr_3Fe_3O_{10}$-GO towards Oxygen Reduction Reaction in Alkaline Medium*, J. Rare Earths **37**, 282 (2019).

[70] A. D. Handoko, S. Deng, Y. Deng, A. W. F. Cheng, K. W. Chan, H. R. Tan, Y. Pan, E. S. Tok, C. H. Sow, and B. S. Yeo, *Enhanced Activity of H_2O_2-Treated Copper(II) Oxide Nanostructures for the Electrochemical Evolution of Oxygen*, Catal. Sci. Technol. **6**, 269 (2015).

[71] S. M. Abd el Haleem and B. G. Ateya, *Cyclic Voltammetry of Copper in Sodium Hydroxide*

Solutions, J. Electroanal. Chem. Interf. Electrochem. **117**, 309 (1981).

[72] D. T. Schwartz and R. H. Muller, *Oxidation Films on Copper in Alkaline Media: Intensity Modulated Photoelectrochemical and Raman Spectroscopy Studies*, Surf. Sci. **248**, 349 (1991).

[73] B. Kumar, S. Saha, M. Basu, and A. K. Ganguli, *Enhanced Hydrogen/Oxygen Evolution and Stability of Nanocrystalline (4–6 Nm) Copper Particles*, J. Mater. Chem. A **1**, 4728 (2013).

[74] D. Guo, R. Shibuya, C. Akiba, S. Saji, T. Kondo, and J. Nakamura, *Active Sites of Nitrogen-Doped Carbon Materials for Oxygen Reduction Reaction Clarified Using Model Catalysts*, Science **351**, 361 (2016).

[75] X. Wang, L. Peng, N. Xu, M. Wu, Y. Wang, J. Guo, S. Sun, and J. Qiao, *Cu/S-Occupation Bifunctional Oxygen Catalysts for Advanced Rechargeable Zinc–Air Batteries*, ACS Appl. Mater. Interfaces **12**, 52836 (2020).

[76] X. Wu, F. Chen, Y. Jin, N. Zhang, and R. L. Johnston, *Silver–Copper Nanoalloy Catalyst Layer for Bifunctional Air Electrodes in Alkaline Media*, ACS Appl. Mater. Interfaces **7**, 17782 (2015).

[77] X. Zhao, F. Li, R. Wang, J.-M. Seo, H.-J. Choi, S.-M. Jung, J. Mahmood, I.-Y. Jeon, and J.-B. Baek, *Controlled Fabrication of Hierarchically Structured Nitrogen-Doped Carbon Nanotubes as a Highly Active Bifunctional Oxygen Electrocatalyst*, Adv. Funct. Mater. **27**, 1605717 (2017).

[78] N. K. Wagh, S. S. Shinde, C. H. Lee, J.-Y. Jung, D.-H. Kim, S.-H. Kim, C. Lin, S. U. Lee, and J.-H. Lee, *Densely Colonized Isolated Cu-N Single Sites for Efficient Bifunctional Electrocatalysts and Rechargeable Advanced Zn-Air Batteries*, Appl. Catal. B **268**, 118746 (2020).

[79] M. Huo et al., *2D Metal–Organic Framework Derived CuCo Alloy Nanoparticles Encapsulated by Nitrogen-Doped Carbonaceous Nanoleaves for Efficient Bifunctional Oxygen Electrocatalyst and Zinc–Air Batteries*, Chem. Eur. J. **25**, 12780 (2019).

[80] Y. Jin and F. Chen, *Facile Preparation of Ag-Cu Bifunctional Electrocatalysts for Zinc-Air Batteries*, Electrochim. Acta **158**, 437 (2015).

[81] P. Liu, Y. Hu, X. Liu, T. Wang, P. Xi, S. Xi, D. Gao, and J. Wang, *Cu and Co Nanoparticle-Co-Decorated N-Doped Graphene Nanosheets: A High Efficiency Bifunctional Electrocatalyst for Rechargeable Zn–Air Batteries*, J. Mater. Chem. A **7**, 12851 (2019).

[82] A. M. Al-Enizi, M. Ubaidullah, J. Ahmed, H. Alrobei, and S. M. Alshehri, *Copper Nickel@reduced Graphene Oxide Nanocomposite as Bifunctional Electro-Catalyst for Excellent Oxygen Evolution and Oxygen Reduction Reactions*, Mater. Lett. **260**, 126969 (2020).

[83] B. Wang et al., *In Situ Confinement Growth of Peasecod-like N-Doped Carbon Nanotubes Encapsulate Bimetallic FeCu Alloy as a Bifunctional Oxygen Reaction Cathode Electrocatalyst for Sustainable Energy Batteries*, J. Alloys Compd. **826**, 154152 (2020).

Chapter 5 General Conclusions

This thesis aimed to synthesize carbon-based materials from designable precursors containing carbon, such as organic compounds and metal-organic frameworks (MOF), under high pressure. The main results of this study can be described below.

In Chapter 2, I examined ultrahigh-pressure experiments on crystalline nitrogen-containing polycyclic aromatic compounds, TQPP and DDQP, respectively. After 5 GPa treatments at room temperature, each recovered sample contained the oligomer. These compounds underwent accompanied by transformation from sp^2-hybridization carbon atoms to sp^3 ones. This result suggests that the aromatic compounds with complex structures, i.e., polycycles and heteroatoms, can occur the pressure-induced addition at mild conditions.

In Chapter 3, I investigated the pyrolysis of MOF under high pressure as a new approach to miniaturizing metal nanoparticles in MOF-derived materials. This approach aimed to take advantage of diffusion suppression of atoms during pyrolysis. The study employed copper benzenetricarboxylate (Cu-BTC) as a precursor MOF and synthesized Cu particles/carbon composites by HPHT treatments at 5GPa. As a result, the treatment at 5 GPa/500 °C produced single-nanometer Cu nanoparticles@carbon composite

materials, significantly smaller than the Cu particles prepared at ambient pressure. I tested catalytic activity for the Huisgen reaction to explore the functions, and this experiment showed much-improved performance compared with the samples synthesized by a conventional method.

In Chapter 4, Cu-BTC pyrolysis was conducted at various applied pressures. The products synthesized at 5 GPa and 1 GPa showed that the particle size of the copper particles in the product changed with the applied pressure. However, for the 0.5 GPa-treated product, the copper formed a shell-like nanostructure on the carbon matrices rather than particles. It is considered that the transportation of copper atoms by outgassing during the pyrolysis affects the morphology. The function of products was examined by electrochemical oxygen reduction/evolution reaction in alkaline media. The results showed that the 0.5 GPa-treated sample was an excellent ORR/OER/ bifunctional electrocatalyst among simple Cu/C materials. This difference in performance can be attributed to the difference in morphology.

This thesis has gained mainly insights related to the pressure-induced oligomerization of aromatics at mild conditions and the effect of metal morphology on the applied pressure and precursor structure in the synthesis of MOF-derived materials. The former insight may be of assistance to the synthesis of novel carbon-based materials from designed aromatic compounds by pressure-induced reactions at mild conditions.

Applying the latter insight to other metals-containing MOF or organometallics should help develop new metal/carbon composite materials.

Appendix

Publications related to this thesis

Chapter 2:

I. Yamane, T. Yanase, T. Taro and T. Toshihiro, *Search for new nitrogen-doped carbon materials by compressing molecular crystals*, Jpn. J. Appl. Phys. **58**, SBBG13 (2019).

Chapter 3:

I. Yamane, K. Sato, R. Otomo, T. Yanase, A. Miura, T. Nagahama, Y. Kamiya, and T. Shimada, *Ultrahigh-Pressure Preparation and Catalytic Activity of MOF-Derived Cu Nanoparticles*, Nanomaterials **11**, 1040 (2021).

Chapter 4:

I. Yamane, K. Sato, T. Ando, T. Tadokoro, S. Yokokura, T. Nagahama, Y. Kato, T. Takeguchi, and T. Shimada, *Ultrahigh pressure-induced modification of morphology and performance of MOFs-derived Cu@C electrocatalysts*, Nanoscale Adv. **5**, 493 (2022).

Acknowledgments

I would like to extend my great thanks to my supervisor Professor Toshihiro Shimada for his constant guidance, encouragement, and support in my research. I would also like to thank Associate Professor Jun Harada and Associate Professor Taro Nagahama for their helpful advice and warm encouragement.

I am deeply grateful to Professor Kiyoharu Tadanaga, Professor Yuichi Kamiya, Associate Professor Akira Miura, Hayato Sakai, Associate Professor Ryoichi Otomo, Lecturer Takashi Yanase (currently at Toho University), and Assistant Professor Seiya Yokokura, Professor Tastuya Takeguchi, and Yoshiki Kato, who provided their experimental facilities and valuable comments to my research.

I would like to thank the members of the laboratory of solid state chemistry for their support and advice. In particular, My sincere thanks go to Kota Sato, Teruki Ando, and Taijiro Tadokoro for their contributions to the experiments as collaborators for years. I also wish to thank Hiroto Inui, who provided an illustration of the cubic anvil apparatus.

I would also like to give a special thank you to my family for their continuous support and understanding.

Ichiro Yamane